Investigating the Dynamic Behaviour of Neurofilaments in Zebrafish

by

Tijotop Ahmed Binjibon

A thesis submitted to the Faculty of Graduate Studies of
The University of Manitoba
in partial fulfillment of the requirements of the degree of

Master of Science

Department of Mathematics
University of Manitoba
Winnipeg

Abstract

Neurofilaments transport is essential for axonal integrity, yet its dynamics in zebrafish remain largely unexplored. In this study, we applied mathematical modelling and computational simulations to analyse neurofilaments transport in zebrafish, comparing it with established findings in mammals. Using the pulse-spread model of Boyer *et. al* [1], we estimated key transport parameters but found it insufficient to fully capture pausing states and anterograde and retrograde velocities. To address this, we developed a partial differential equation (PDE) model that incorporated bidirectional transport, pausing, anterograde and retrograde dynamics. Additionally, we derived pure exchange, pure transport, and transport-exchange sub-models, offering deeper insights into the transport of neurofilaments. Using data from Bomont's lab pulse-spread experiments (NeuroMyoGène Institute, Lyon, France), our findings confirmed that the transport of neurofilaments is bidirectional, with an anterograde bias that reverses with age. Increasing the central window length significantly extends the quantified residence time of neurofilaments within the central region. Additionally, when considering reversible pausing, we found that exchange dominates transport and defined the steady state neurofilaments organization. This study advances our understanding of neurofilaments transport in zebrafish and establishes a framework for future investigations into axonal transport mechanisms across species, with potential implications for neurodegenerative disease research.

Acknowledgements

I wish to express my heartfelt appreciation to my supervisor, Dr. Stéphanie Portet, whose exceptional mentorship, unwavering support, and inspiring guidance have been instrumental throughout my master's program. Her patience, wisdom, and compassion were fundamental to bringing this thesis to fruition. My sincere thanks go to my thesis committee members, Dr. Julien Arino and Dr. Kang-Ling Liao, whose insightful feedback, constructive comments, and valuable recommendations greatly enhanced the caliber of this research. I sincerely thank Dr. Pascale Bomont and Van Asperen Jessy of the NeuroMyoGène Institute (Lyon, France) for performing the pulse-spread experiments in Bomont's lab and generously providing the experimental data used in this study. I am grateful for the financial assistance provided by the Teaching/Research assistantship from the Department of Mathematics, the International Graduate Entrance Scholarship, and the Research Completion Scholarship from the Faculty of Graduate Studies, which made this academic pursuit possible. Special recognition goes to the dedicated administrative team—Kristina Kovacevic, Melanie Vanderhorst, Alison Skopalek, and Liza Yaroshenko—whose warmth and ongoing support have been deeply appreciated throughout my studies. Lastly, I would like to thank the entire faculty, as well as my fellow students and colleagues in the Department of Mathematics, for fostering an environment of encouragement, collaboration, and friendship that enriched my academic experience.

Dedication

I dedicate this thesis to my beloved family — my father, Najah Binjibon, my mother, Bibelah N-nyibe, and all my brothers — for their unwavering support, encouragement, and sacrifices throughout every stage of my education. I am also deeply grateful to my spouse, whose love, patience, and constant prayers have been a pillar of strength during this journey.

Contributions of Authors

The research presented in this thesis was primarily conducted by the author, including the development of mathematical models, analysis of experimental data, numerical simulations, and manuscript preparation. Dr. Stéphanie Portet provided overall supervision, conceptual guidance, and critical feedback throughout the project. The experimental data used in this study were generated from pulse-spread experiments carried out on zebrafish by Bomont's lab at the NeuroMyoGène Institute (Lyon, France), to whom I am grateful for their collaboration and data provision. The model used in Chapter 3 was originally developed by Boyer *et al.* [1] and was adopted in this thesis to analyse the data obtained on zebrafish and compare them with analysis results from mices.

Contents

List of Figures

List of Tables

List of Symbols

$[x_i]_{i=1}^n$	The list x_1, x_2 ...x_n
$\mathbb{R}_+$	The set $[0, \infty)$ of non-negative real numbers
$\mathbb{R}^n$	The n-dimensional Euclidean space
$\mathbb{R}_+^n$	The n-dimensional nonnegative orthant $\{(x_1, \ldots, x_n) \in \mathbb{R}^n : x_1 \geqslant 0, \ldots, x_n \geqslant 0\}$
$det[\cdot]$	The determinant of a matrix
$\|\cdot\|$	Euclidean norm
I_n	The n-dimensional identity matrix
A^T	The transpose of A
$R(\cdot)$	The resilience of an equilibrium
$\Re(\cdot)$	The reactivity of an equilibrium
λ_L^A	The eigenvalue with the largest real part of A
$H(A)$	The Hermitian part of the matrix A

1

Introduction

This research studied axonal neurofilaments transport in zebrafish using mathematical modelling and computational simulations. This chapter provides a biological background for the study of neurofilaments and highlights the motivation for this research. It also outlines the framework and overall structure of the work.

1.1 The Composition of Cytoskeleton

The cytoskeleton is classified into microfilaments (actin), intermediate filaments, and microtubules [5, 6] based on their respective diameters - $7nm$, $10nm$, and $25nm$- and protein composition. These proteins assemble in filaments that form interconnected networks found in the cytoplasm of eukaryotic cells, which constantly reorganize in response to their environment to be able to play their vital role in the structure and functions of cells [7]. Cytoskeletal proteins are responsible for cell shape and motility as well as transport [8], providing mechanical support and organization of intracellular components [9, 10]. The protein composition of microtubules and microfilaments is highly conserved, whereas intermediate filaments are remarkably diverse, with their composition varying depending on the cell type and differentiation stage [11]. For instance, keratins are present in epithelial cells, vimentin in

connective tissues and blood cells, and neurofilaments in nerve cells. The perception of intermediate filaments as relatively static components within cells underwent a profound shift when fluorescently labelled intermediate filaments were observed in live cells, illuminating their remarkably dynamic characteristics [12, 13, 14]. These investigations have revealed that both keratin and vimentin filaments are transported along microtubule tracks by motor proteins, just like neurofilaments. Several studies (see, for instance, [15, 16]) suggested that such motions are general characteristics of intermediate filaments.

1.1.1 Intracellular Transport of Intermediate Filaments

Intracellular transport of intermediate filaments is a critical dynamic process for cellular architecture, mechanical resilience, and adaptive responses. Unlike microtubules and actin filaments, intermediate filaments are nonpolar and do not intrinsically contribute to motor-driven motility [17]. Instead, their transport relies on interactions with microtubules, actin networks, and associated motor proteins, enabling spatiotemporal regulation of intermediate filaments network organization [15, 18].

Microtubules serve as the primary highways for long-range intermediate filaments transport [19]. Kinesin motors mediate anterograde movement (toward the cell periphery), whereas retrograde transport (toward the cell center) involves cytoplasmic dynein. These motors bind intermediate filaments either directly or via adaptors such as dynactin [20]. Microtubule-dependent transport enables rapid intermediate filaments reorganization in response to mechanical cues, ensuring cellular adaptation to shear stress or substrate stiffness [21, 22].

The actin cytoskeleton governs the short-range transport and spatial organization of intermediate filaments, particularly near the cell periphery and during dynamic processes such as migration [19, 23]. Actin arcs—contractile bundles driven

by myosin—generate retrograde flow, exerting rearward tension on intermediate filaments to align them with actin networks and integrate them into stress fibres [24]. This retrograde movement collaborates with myosin motors to fine-tune intermediate filaments positioning during polarization, wound healing, and force transmission [25].

Microtubules and actin networks cooperate to balance long-range transport and localized intermediate filaments dynamics. While microtubules disperse intermediate filaments globally via kinesin/dynein motors, actin fine-tunes their localization at specific subcellular domains through retrograde flow and myosin activity [19]. This spatial division of labour creates a mechanical "tug-of-war," where anterograde/retrograde microtubule transport balances actin-driven retrograde forces, stabilizing intermediate filaments in mechanically active regions [26]. Together, this cross-talk enables cells to maintain structural integrity while adapting to environmental demands.

Neurons exhibit a highly polarized structure, with lengthy axons extending from the cell body to distant synaptic terminals. This distinctive morphology poses a considerable challenge for intracellular transport, necessitating efficient long-range movement of organelles, proteins, and cytoskeletal components [27]. Unlike other cell types, where transport occurs in a more compact space, neurons depend on specialized transport mechanisms to maintain cellular homeostasis (maintaining a stable internal environment in cells) and support synaptic function over extended distances [27]. Axonal transport is a fundamental process that enables the movement of molecular cargo along microtubules, powered by motor proteins such as kinesin and dynein [28]. This transport system is essential for neuronal survival, ensuring the delivery of organelles, vesicles, and cytoskeletal components to regions far from the cell body (soma). Unlike cell body regions, where actin filaments influence intracellular transport, axonal transport predominantly relies on microtubule-based

mechanisms [29], providing a more controlled environment to study microtubule-driven transport without interference from actin networks.

Our objective in this study is to investigate the dynamic transport of neurofilaments in the axons of zebrafish and to compare our findings with similar studies conducted in other organisms, such as mice [1, 30, 31]. We further aim to understand what proportion of fluorescent neurofilaments is pausing in a short time of minutes and the dynamics of switching between mobile and stationary populations.

1.2 The Neurofilaments

Neurofilaments are flexible protein polymers, with a diameter of approximately $10nm$ [32] as mentioned above, and a length of up to at least $40\mu m$ [33, 34]. Neurofilaments are numerous space-filling cytoskeleton protein polymers that are assembled within neuronal cell body [35] and are then conveyed into axons and transported along their length through the complex mechanisms of axonal transport [1, 36]. This phenomenon of neurofilaments axonal transport, which was first revealed by using radioisotopic pulse labelling techniques [37], is stochastic and in a "stop-and-go" manner, characterized by short bursts of rapid motion followed by extended periods of pauses, giving rise to a slow overall movement rate [2, 38]. The transport, which is along microtubule tracks just like other intermediate filaments, is driven by kinesin and dynein, which respectively enhance anterograde and retrograde motion along the axon [39]. The anterograde moving state of neurofilaments refers to the movement of these filaments from the cell body toward the periphery (axon terminal) of the cell (Figure 1.1). This is facilitated by the interaction with kinesin along microtubules. However, the retrograde moving state of neurofilaments refers to the movement of these filaments from the periphery of the cell toward the cell body (Figure 1.1). This is also facilitated by the interaction with dynein that moves the filaments along

microtubules in the opposite direction of anterograde flow.

The cross-sectional area of axons determines its conduction velocity and can expand by up to 50 times during the postnatal development of mammals [40, 41]. During this developmental period, the neurofilaments polymers assemble in myelinated axons resulting in an enlargement of axon calibre, which is important for facilitating rapid transmission of electrical impulse [2, 42]. Without neurofilaments, the axons cannot increase in caliber [43], resulting in a reduction in conduction velocity[2, 44, 45]. With advances in technology, fluorescence microscopy can now be used to monitor the motion of neurofilaments in cultured nerve cells, in time units of seconds or minutes [46].

Several studies have recently been conducted to try to understand the mode and mechanism of this axonal transport (see, for example, [2, 11, 47]). These studies show that neurofilaments undergo assembly or disassembly processes [48] during intracellular transport. This interplay of phenomena, which determines the organization of neurofilaments in neurons, is of interest to many researchers.

1.2.1 Neurofilaments and Related Diseases

Neurofilaments accumulation in neurodegenerative diseases—such as Charcot-Marie-Tooth disease, dementia, diabetic neuropathy, and spinal muscular atrophy—differs significantly from the patterns observed in healthy axons [49]. This phenomenon has been attributed to several factors including defects in motor proteins, neurofilaments mutations, defective axonal transport and several toxic agents [50]. It has been reported that normal axons display a characteristic alignment of microtubules and neurofilaments that runs along their length [51, 52]. Additionally, in cross-sectional views of axons, these microtubules and neurofilaments are interspersed, with microtubules often clustering around membranous organelles [51, 52]. However, it has been observed that the arrangement of polymers changes, resulting in the clustering

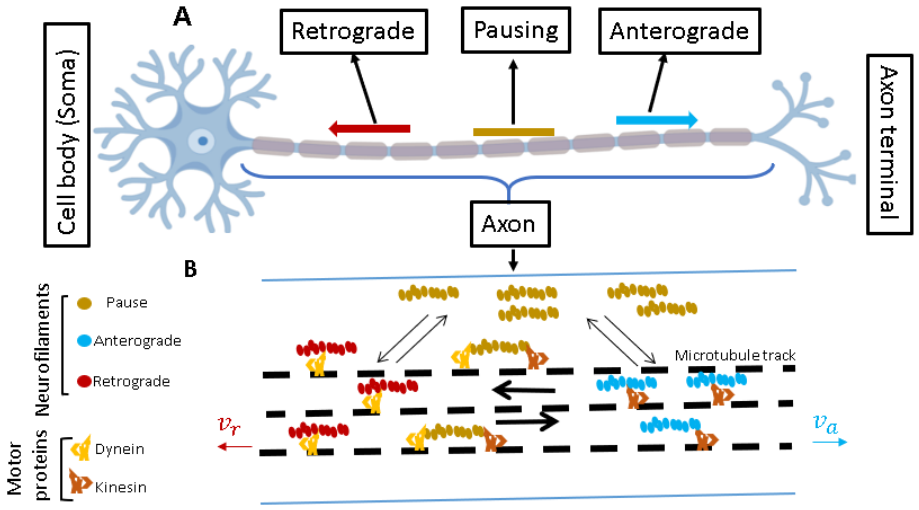

Figure 1.1: **A neuron and neurofilaments transport dynamics.**(A) A neuron is composed of an axon connecting cell body (soma) to the axon terminal. Directions of axonal transport are indicated by coloured arrows. (B) An axonal segment, showing the primary transport states of neurofilaments along microtubule tracks (black dashed lines): anterograde transport (blue, directed toward the axon terminal with velocity v_a, mediated by kinesin motors) and retrograde transport (red, directed toward the soma with velocity v_r, mediated by dynein motors). Pausing states are shown as on-track (orange, when neurofilaments are still attached to microtubules via both antagonistic motor proteins) and off-track (orange, when neurofilaments are detached from the microtubule tracks). Bidirectional black arrows indicate potential transitions between these mobile and immobile states, reflecting the dynamic exchange of neurofilaments.

of microtubules and membranous organelles towards the midpoint of the axon, while neurofilaments are pushed toward the outer periphery in many neurodegenerative diseases like Charcot-Marie-Tooth disease [53]. Hence, it is crucial to understand the factors driving the organization and transport of the intermediate filaments in cells and their effects on health and disease conditions. These can aid in finding new directions for therapy for numerous generational neurodegenerative disorders.

1.3 Motivation

Mathematical modelling serves as a powerful tool for simplifying complex real-life phenomena, facilitating detailed analysis and the derivation of meaningful insights

(see, for example, [54]). By breaking down intricate biological processes into manageable components, modelling fosters a deeper understanding of underlying mechanisms and aids in making informed predictions (see, for example, [55]). This approach has addressed numerous challenges in biology and related fields, with the study of neurofilaments transport being no exception. Blum and Reed [56] were the pioneers in developing a mathematical model that describes the axonal transport of neurofilaments, laying the groundwork for subsequent research into this complex process. Building on this foundation, Brown *et al.* [38, 57] introduced stochastic "stop-and-go" models, attributing slow axonal transport to alternating phases of rapid bidirectional movement and pauses. Later, [2, 3] expanded these concepts with a six-state kinetic model, categorizing neurofilaments motility into anterograde/retrograde movement, short-term pausing, and long-term pausing states. Dallon *et al.* [58, 59] incorporated motor competition by modelling intermediate filaments as flexible chains undergoing dynein-kinesin "tug-of-war," while [60] developed a multiscale stochastic framework to simulate microtubule-neurofilaments segregation in neurodegenerative contexts. Probabilistic models have been developed to identify the necessary conditions for axonal transport to produce uniform distributions of material within axons [61]. Collectively, these models form a foundation to interrogate neurofilaments transport dynamics. Numerous studies to further understand the nature of neurofilaments transport led to several key propositions: it is bidirectional [62], exhibits an anterograde bias [1], can switch between anterograde and retrograde directions, slows with age, and constantly alternates between periods of immobility and motion [46]. Although these propositions have provided valuable insight, many aspects of neurofilaments transport remain under investigation. Recent studies [47] have challenged the claim that a significant proportion of neurofilaments remain immobile for months [63, 64]. Notably, much of the current understanding is based on research conducted in organisms such as rats and mice. This thesis seeks to extend these investigations

by exploring whether similar dynamic behaviours occur in zebrafish. Zebrafish, a tropical freshwater fish, has gained significant interest in scientific research and drug development [65]. This is largely because it possesses organs that are anatomically and functionally similar to those of mammals. Additionally, zebrafish reproduce and grow rapidly, produce large quantities of offspring, and are relatively easy to maintain [66], making them an ideal model organism for various studies.

To this end, Bomont's laboratory (Neuromyogene Institute, Lyon, France) conducted pulse-spread experiments on zebrafish axons at various developmental stages. These experiments generated data that we analyse to gain insight into how neurofilaments movement evolves with age. Additionally, data were collected using different central window lengths to evaluate their influence on transport characteristics. Full details of the experimental setup and data are provided in Chapter 3. Through this analysis, we aim to offer a broader perspective on neurofilaments transport across species and contribute to a deeper understanding of its underlying mechanisms.

1.4 Thesis Outline

The subsequent part of this thesis consists of six chapters. In chapter 2, we present the mathematical tools used in our work. In chapter 3, we analysed and presented the results of Bomont's lab pulse-spread data using the previous model developed by Boyer *et. al* [1]. Chapter 4 presents a fully developed partial differential equations model, from which four sub-models are derived: one that captures the dynamics of switching between different compartments, another that focuses on pure transport dynamics when switching is negligible and the last one that combines both transport and exchange, where we refine the pure transport model by exploring two key scenarios: (i) when neurofilaments transition off-track with diffusion and do not return to the moving states, and (ii) when off-track neurofilaments return to the moving states,

but diffusion is neglected. In chapter 5, we present the mathematical analysis of our models. In Chapter 6, we present numerical results and simulations of the proposed models. Chapter 7 presents the discussion and conclusion, and the appendix brings the work to an end.

2

Tools

This section highlights key mathematical tools employed in analyzing ordinary differential equations (ODEs), partial differential equations (PDEs), and solving the associated modelling challenges. In particular, we use the concept of stability to assess the behaviour of equilibrium solutions in our ODE systems—an essential step in understanding the long-term dynamics of neurofilaments distributions between mobile and immobile states. For the PDE models, we employed the method of characteristics that allows us to describe the spatiotemporal evolution of neurofilaments transport. Additionally, we apply optimization methods, specifically genetic algorithms (GA) enable us to optimize model parameters by fitting the model to experimental data. These tools form the core of our analytical and computational approach.

2.1 Qualitative Tools for ODE Analysis

We consider a system of n interacting populations modelled by nonlinear ordinary differential equations. For any time $t \geqslant 0$, let $\pi(t) \in \mathcal{D} \subset \mathbb{R}^n_+$ denote a non-negative vector of population densities, where $\pi_i(t)$ represents the density of the i-th popula-

tion. The system's dynamics is governed by:

$$\frac{d\pi(t)}{dt} = \mathbf{g}(\pi(t), t), \quad \pi(t) \in \mathcal{D}, \quad t \in \mathbb{R}_+, \tag{2.1.1}$$

where $\mathbf{g} : \mathcal{D} \times \mathbb{R}_+ \to \mathbb{R}^n$ is a vector field defining the rate of change of $\pi(t)$. The system (2.1.1) is autonomous if $\mathbf{g}(\pi(t), t) \equiv \mathbf{g}(\pi(t))$, meaning the dynamics depends only on the state $\pi(t)$, not explicitly on t; otherwise, it is non-autonomous.

Definition 2.1.1. A function $\mathbf{g} : \mathcal{D} \times \mathbb{R}_+ \to \mathbb{R}^n$ is **continuous at a point** $\pi \in \mathcal{D}$ if, for every $\epsilon > 0$, there exists a $\delta(\epsilon) > 0$ such that for all $\pi_1, \pi_2 \in \mathcal{D}$, if:

$$\|\pi_2 - \pi_1\| < \delta \quad \text{then} \quad \|\mathbf{g}(\pi_2, t) - \mathbf{g}(\pi_1, t)\| < \epsilon \quad \text{for all} \quad t \in \mathbb{R}_+.$$

If this holds for all points in $\mathcal{D}$, then $\mathbf{g}$ is **continuous** on $\mathcal{D}$.

Definition 2.1.2. Let $t_0 \in \mathbb{R}_+$ and $\pi_0 \in \mathcal{D}$. The system (2.1.1) with the initial condition $\pi(t_0) = \pi_0$, written as:

$$\frac{d\pi(t)}{dt} = \mathbf{g}(\pi(t), t), \quad \pi(t_0) = \pi_0, \tag{2.1.2}$$

is called an **initial value problem (IVP)**.

Theorem 2.1.3. *[67] Suppose the IVP* (2.1.2) *satisfies:*

1. $\mathbf{g}(\pi(t), t)$ *is continuous on* $\mathcal{D} \times \mathbb{R}_+$.
2. *The partial derivatives* $\left[\frac{\partial g_i}{\partial \pi_j}\right]_{i,j=1}^{n}$ *exist and are continuous on* $\mathcal{D} \times \mathbb{R}_+$*, where* g_i *and* π_j *are the* i*-th and* j*-th components of* $\mathbf{g}$ *and* π*, respectively.*

Then there exists a unique solution $\pi(t)$ *to the IVP* (2.1.2) *on an interval* $\mathcal{I} \subseteq \mathbb{R}_+$ *containing* t_0.

Definition 2.1.4. A point $\pi^* \in \mathcal{D} \subset \mathbb{R}_+^n$ is an **equilibrium** of the system (2.1.2) if $\mathbf{g}(\pi^*, t) = \mathbf{0}$ for all $t \in \mathbb{R}_+$. That is, π^* is a time-independent solution.

- For an **autonomous system** (i.e., $\mathbf{g}(\pi, t) = \mathbf{g}(\pi)$), this simplifies to $\mathbf{g}(\pi^*) = \mathbf{0}$.
- For a **non-autonomous system**, the condition $\mathbf{g}(\pi^*, t) = \mathbf{0}$ must hold for all $t \geqslant 0$.

Definition 2.1.5. (For autonomous systems). The **Jacobian matrix** of the vector field $\mathbf{g}$ in (2.1.2) with respect to π is defined as:

$$J(\pi) = \left[\frac{\partial g_i(\pi)}{\partial \pi_j}\right]_{i,j=1}^{n},$$

where $\frac{\partial g_i}{\partial \pi_j}$ is the partial derivative of the i-th component of $\mathbf{g}$ with respect to the j-th component of π. This matrix, used as the coefficient matrix of a linear system, defines the linearization of the system (2.1.2) around a point π.

Definition 2.1.6. (For autonomous systems). An equilibrium π^* of the system (2.1.2) is **hyperbolic** if none of the eigenvalues of the Jacobian matrix $J(\pi^*)$, evaluated at π^*, have a zero real part.

Theorem 2.1.7. *[68] Let $\pi^* \in \mathcal{D}$ be a hyperbolic equilibrium of the system* (2.1.2)*, with the Jacobian matrix $J(\pi^*)$ as in Definition 2.1.5. For autonomous systems, consider the linearized dynamics of a perturbation $\mathbf{z}(t) = \pi(t) - \pi^*$, governed by:*

$$\frac{d\mathbf{z}}{dt} = J(\pi^*)\mathbf{z}. \tag{2.1.3}$$

Then:

1. *If all eigenvalues of $J(\pi^*)$ have negative real parts, the equilibrium π^* is locally asymptotically stable, meaning perturbations $\mathbf{z}(t)$ decay to zero over time.*
2. *If at least one eigenvalue has a positive real part, the equilibrium π^* is unstable, and perturbations grow [69].*

2.1.1 The Case of Linear Systems

In this subsection, we analyse the special case of linear systems within the framework of autonomous ordinary differential equations. Consider the system (2.1.2) where the vector field $\mathbf{g}(\pi(t))$ is linear, i.e., it can be expressed as:

$$\mathbf{g}(\pi(t)) = A\pi(t) + \mathbf{b}, \tag{2.1.4}$$

where A is an $n \times n$ constant matrix, $\mathbf{b} \in \mathbb{R}^n_+$ is a constant vector, and $\pi(t) \in \mathcal{D} \subset \mathbb{R}^n_+$. The system (2.1.2) becomes:

$$\frac{d\pi(t)}{dt} = A\pi(t) + \mathbf{b}, \quad \pi(t_0) = \pi_0. \tag{2.1.5}$$

Since $\mathbf{g}$ does not explicitly depend on t, the system is autonomous.

Equilibrium Points

An equilibrium point π^* of the system (2.1.5) satisfies $\mathbf{g}(\pi^*) = \mathbf{0}$, i.e.,

$$A\pi^* + \mathbf{b} = \mathbf{0}. \tag{2.1.6}$$

- **Non-Homogeneous Systems ($\mathbf{b} \neq \mathbf{0}$)** [70]: Solving (2.1.6), we get:

  $$\pi^* = -A^{-1}\mathbf{b},$$

  provided A is invertible (i.e., $\det[A] \neq 0$). In this case, the equilibrium is unique.

- **Homogeneous Systems ($\mathbf{b} = \mathbf{0}$)** [70]: If $\mathbf{b} = \mathbf{0}$, the system reduces to:

  $$\frac{d\pi(t)}{dt} = A\pi(t), \tag{2.1.7}$$

and the equilibrium condition becomes $A\pi^* = \mathbf{0}$. The origin $\pi^* = \mathbf{0}$ is always an equilibrium. If A is invertible, this is the only equilibrium.

Stability Analysis

For linear autonomous systems, the Jacobian matrix of $\mathbf{g}(\pi) = A\pi + \mathbf{b}$ with respect to π is:

$$J(\pi) = A,$$

which is independent of π. Thus, the stability of the equilibrium π^* is determined globally (not just locally) by the eigenvalues of A, as stated in Theorem 2.1.7.

- **Solution Form:**

  The unique solution to the initial value problem (2.1.5) is given by:

  $$\pi(t) = e^{A(t-t_0)}\pi_0 + \int_{t_0}^{t} e^{A(t-s)}\mathbf{b}\, ds.$$

  In particular, when $t_0 = 0$, this simplifies to:

  $$\pi(t) = e^{At}\pi(0) + \int_{0}^{t} e^{A(t-s)}\mathbf{b}\, ds.$$

  For homogeneous systems, $\mathbf{b} = \mathbf{0}$, the solution simplifies to $\pi(t) = e^{At}\pi(0)$, and the behaviour of e^{At} is governed by the eigenvalues of A.

- **Homogeneous Linear System**: Consider the homogeneous system (2.1.7). Instead of directly computing e^{At}, we seek n linearly independent solutions $\pi_i(t)$ to form a fundamental matrix. We assume that solutions take the form: $\pi_i(t) = e^{\lambda_i t}\mathbf{u}_i$, where λ_i is an unknown scalar and $\mathbf{u}_i$ is an unknown $n \times 1$ vector. Substituting into (2.1.7) yields the eigenvalue problem:

  $$A\mathbf{u}_i = \lambda_i \mathbf{u}_i.$$

- To find λ_i (for $i = 1, \ldots, n$), solve the characteristic polynomial:

$$\det[A - \lambda I_n] = 0.$$

- To find $\mathbf{u}_i$ (for $i = 1, \ldots, n$), solve the system:

$$(A - \lambda_i I_n)\mathbf{u}_i = \mathbf{0}.$$

Theorem 2.1.8. *If A has n distinct eigenvalues $\lambda_1, \ldots, \lambda_n$, with corresponding eigenvectors $\mathbf{u}_1, \ldots, \mathbf{u}_n$, the general solution to* (2.1.7) *on $\mathbb{R}_+$ is:*

$$\pi(t) = c_1\mathbf{u}_1 e^{\lambda_1 t} + \cdots + c_n\mathbf{u}_n e^{\lambda_n t},$$

where $c_1, \ldots, c_n$ are arbitrary constants determined by the initial condition $\pi(t_0) = \pi_0$.

2.1.2 Routh-Hurwitz Stability Criterion

In this section, we introduce the Routh-Hurwitz stability criterion, a valuable method for assessing the stability of linear systems. This criterion analyses the roots of the characteristic polynomial derived from the Jacobian matrix $J(\pi^*)$ of the linearized system (2.1.3). Consider the characteristic polynomial of an $n \times n$ matrix with real entries:

$$P(\lambda) = \lambda^n + e_1\lambda^{n-1} + \cdots + e_{n-1}\lambda + e_n.$$

where the coefficients $[e_i]_{i=1}^n$ are real constants. We define the n Hurwitz matrices using the coefficients e_i of the characteristic polynomial and their determinants are as follows

$$H_1 = det[e_1], \quad H_2 = det\begin{bmatrix} e_1 & 1 \\ e_3 & e_2 \end{bmatrix}, \quad H_3 = det\begin{bmatrix} e_1 & 1 & 0 \\ e_3 & e_2 & e_1 \\ e_5 & e_4 & e_3 \end{bmatrix}, \ldots$$

and in general,

$$H_n = det\begin{bmatrix} e_1 & 1 & 0 & 0 & \ldots & 0 \\ e_3 & e_2 & e_1 & 0 & \ldots & 0 \\ e_5 & e_4 & e_3 & e_2 & \ldots & 0 \\ \vdots & \vdots & \vdots & \vdots & \ddots & \vdots \\ 0 & 0 & 0 & 0 & \ldots & e_n \end{bmatrix}$$

where $e_i = 0$ if $i > j$.

Theorem 2.1.9. *[71] All roots of the polynomial $P(\lambda)$ have negative real parts (or are negative if real) if and only if the determinants of all Hurwitz matrices are positive (i.e. $[H_j]_{j=1}^n > 0$.)*

Routh-Hurwitz Criteria for Small n

For specific values of n, the stability conditions reduce to:

- $n = 2$: $e_1 > 0$ and $e_2 > 0$.
- $n = 3$: $e_1 > 0$, $e_3 > 0$, and $e_1 e_2 > e_3$.
- $n = 4$: $e_1 > 0$, $e_3 > 0$, $e_4 > 0$, and $e_1 e_2 e_3 > e_3^2 + e_1^2 e_4$.

These conditions provide a practical way to assess stability without computing the eigenvalues directly, especially for low-dimensional systems.

2.1.3 Resilience and Reactivity

Consider a system with a stable equilibrium point π^*, as derived from the linear system (2.1.5). We focus on assessing how swiftly the system recovers after a minor

disturbance from this equilibrium. Pimm and Lawton (1977) introduced the concept of the resilience of an equilibrium (e.g., π^*), which we denote as $R(\pi^*)$, to address this question. Resilience quantifies the asymptotic rate at which a typical perturbation diminishes - the quicker the decay, the more resilient the system. Mathematically, resilience is calculated as:

$$R(\pi^*) = -\mathrm{Re}(\lambda_L^A) > 0, \tag{2.1.8}$$

where λ_L^A represents the eigenvalue with the largest (maximum) real part of the coefficient matrix A of the linear system (2.1.5). The reciprocal, $\frac{1}{R(\pi^*)}$, indicates the average return time to the stable equilibrium.

Stability and resilience describe the long-term behaviour of the system after disturbances but do not address the transient effects of perturbations or shocks. They indicate whether the system will return to equilibrium (stable) and how quickly (resilient). However, a small perturbation can still cause notable short-term growth even if the system is stable. To capture this short-term response, Neubert *et al.* [72] proposed a measure called reactivity, which we denote as $\Re(A)$. Reactivity represents the maximum instantaneous rate at which a small perturbation can grow before returning to the stable equilibrium, considering all possible initial conditions. This is computed as:

$$\Re(A) = \lambda_L^{H(A)}, \tag{2.1.9}$$

where $\lambda_L^{H(A)}$ is the largest (maximum) eigenvalue of $H(A)$ defined as $H(A) = \frac{A+A^\top}{2}$. Here, $A^\top$ is the transpose of A, and since $H(A)$ is symmetric, all its eigenvalues are real. If $\lambda_L^{H(A)} > 0$, the equilibrium is reactive, and the perturbation immediately grows before decaying to the stable equilibrium; otherwise, it is non-reactive and monotonically decays or grows to the stable equilibrium.

2.2 Solutions of PDEs

This section focuses on solving PDEs that arise in modelling neurofilaments transport, a critical process in understanding neuronal dynamics. We consider PDEs that describe the spatiotemporal evolution of population densities, such as those for neurofilaments, which are influenced by both convective transport and linear reaction terms. The method of characteristics is the tool used to derive explicit solutions for these PDEs under given initial conditions.

2.2.1 Method of Characteristics

We explore the one-dimensional transport of an incompressible fluid (with constant density) using the method of characteristics, which is well-suited for solving first-order PDEs. This method is applied to PDEs that describe the evolution of particle density $u(x,t)$ over time t and space x, driven by convective processes. We begin with the homogeneous advection PDE and then extend the approach to include non-homogeneous terms, such as linear reaction terms, to model more complex dynamics like neurofilaments transport and exchange between motile states.

Homogeneous Advection PDE

Consider the pure advection PDE, which models the transport of a density without reaction terms:

$$\frac{\partial u(x,t)}{\partial t} + v\frac{\partial u(x,t)}{\partial x} = 0, \quad u(x,0) = u_0(x), \tag{2.2.1}$$

where v is a nonzero constant velocity and $u_0(x)$ is the initial condition. Implies, along $x(t)$ in (x,t)-plane, u changes as follows

$$\frac{du}{dt} = \frac{\partial u}{\partial t} + \frac{dx}{dt}\frac{\partial u}{\partial x}. \tag{2.2.2}$$

Comparing (2.2.1) and (2.2.2), we get $\frac{du}{dt} = 0$, and characteristic curves $\frac{dx}{dt} = v$,

along which $u(x,t)$ is constant. Further, the characteristic curves are

$$x(t) = vt + x_0 \quad \text{and} \quad u(x,t) = c.$$

Using the initial condition in (2.2.1),

$$u(x_0, 0) = c = u_0(x_0) = u_0(x - vt).$$

Therefore, the solution to the PDE in (2.2.1) is $u(x,t) = u_0(x - vt)$.

Non-Homogeneous Advection PDE with Reaction Term

We now extend the method to a non-homogeneous PDE that includes a linear reaction term, modelling the density $u(x,t)$ of a fluid with decay:

$$\frac{\partial u}{\partial t} + v\frac{\partial u}{\partial x} = -\lambda u, \quad u(x,0) = u_0(x), \tag{2.2.3}$$

where $v \neq 0$ is the transport velocity, $\lambda > 0$ is the decay rate, and $u_0(x)$ is the initial condition. Using the method of characteristics, we apply the Lagrange–Charpit equations (see details [73]) to the PDE (2.2.3) gives:

$$\frac{dt}{1} = \frac{dx}{v} = \frac{du}{-\lambda u}.$$

- From $\frac{dt}{1} = \frac{dx}{v}$, the characteristic curves are:

$$\frac{dx}{dt} = v \quad \Longrightarrow \quad x(t) = vt + x_0,$$

identical to the homogeneous case.

- From $\frac{dt}{1} = \frac{du}{-\lambda u}$, we obtain the ODE along the characteristic curves:

$$\frac{du}{dt} = -\lambda u.$$

Solving this first-order linear ODE:

$$\frac{du}{u} = -\lambda dt \quad \Longrightarrow \quad \ln|u| = -\lambda t + C \quad \Longrightarrow \quad u(t) = C'e^{-\lambda t},$$

where C' is a constant. At $t = 0$, $x = x_0$, so $u(x_0, 0) = u_0(x_0)$, and thus:

$$u(0) = C' = u_0(x_0).$$

Therefore, along the characteristic curve:

$$u(x, t) = u_0(x_0)e^{-\lambda t}.$$

Substituting $x_0 = x - vt$, the solution to (2.2.3) is:

$$u(x, t) = u_0(x - vt)e^{-\lambda t}.$$

This solution describes the density $u(x, t)$ as it is transported with velocity v while decaying exponentially at rate λ.

2.3 Global vs. Local Optimization Methods

In the modelling of neurofilament transport, a key challenge is to accurately estimate model parameters so that the resulting solutions match experimental data, ensuring the model reliably captures the observed dynamics of neurofilaments populations. Optimization methods are crucial for this task, as they allow us to systematically

search the parameter space to minimize the error between model predictions and experimental observations. Optimization is the process of selecting the best possible solution from a set of feasible alternatives to efficiently achieve a desired objective [74]. Optimization methods are broadly categorized into local and global approaches, depending on their search strategy. We explore both global and local optimization methods to achieve this goal, with a particular emphasis on global methods to avoid local optima in our complex, nonlinear system.

- **Local Optimization**:
  - Focuses on finding the nearest optimal solution within a small region of the search space.
  - Relies on gradient-based methods (e.g., Newton-Raphson, gradient descent) and is computationally efficient.
  - Prone to converging to local optima (suboptimal solutions) if the objective function is nonlinear, multimodal, or noisy [74].
- **Global Optimization**:
  - Explores the entire search space to identify the global optimum, the best solution among all possible candidates.
  - Suitable for complex, high-dimensional problems with multiple local optima or non-differentiable functions.
  - Examples include genetic algorithms (GAs), particle swarm optimization (PSO), and simulated annealing [75, 76].

For this study, we employed a GA to solve the data-fitting problem. Unlike local methods, GAs avoid premature convergence to local optima by leveraging stochastic search mechanisms inspired by biological evolution [77, 78].

2.3.1 Genetic Algorithm Framework

The GA iteratively refines a population of candidate parameter sets through cycles of selection, crossover, and mutation. Below, we outline its key components:

1. Population Initialization

The algorithm starts by generating an initial population of candidate solutions (parameter sets). Each individual in the population represents a unique combination of parameters, analogous to a chromosome in biological systems.

2. Fitness Evaluation

A predefined fitness function quantifies how well the model output, generated using a given parameter set, matches the observed data. Individuals that produce lower error values (indicating better agreement with the data) are assigned higher fitness scores and are prioritized for reproduction [79].

3. Selection

Selection mimics natural "survival of the fittest" by choosing parents to produce offspring. Common strategies include:

- **Roulette Wheel Selection**: Probabilistic selection proportional to fitness.
- **Tournament Selection**: Randomly sampled subsets compete, with the fittest advancing.
- **Rank-Based Selection**: Prioritizes individuals based on fitness rank [77].

4. Crossover

Crossover combines genetic material from two parents to create offspring. This promotes exploration of the search space by merging promising parameter combinations.

For example, in uniform crossover, parameters are swapped at random positions [80].

5. Mutation

Mutation introduces random perturbations to individual parameters, preserving genetic diversity and enabling escape from local optima. The mutation rate is typically low to balance exploration and "exploitation" [79].

6. Termination

The algorithm ends once a predefined stopping condition is satisfied, such as:

- Reaching a maximum number of generations.
- Achieving a target fitness threshold.
- Observing no improvement in fitness over successive generations.

The best parameter set from the final population is returned as the solution [81]. The flowchart of this GA is as presented in Figure 2.1.

Parameter optimization of our model is conducted using the GA implemented in R via the GA package [82]. This package offers a robust framework for evolutionary computation, allowing for customizable selection, crossover, and mutation operators tailored to our model's parameter space. The implementation leveraged the GA package's optimization capabilities to calibrate the model against experimental data, ensuring an efficient search for the best-fitting parameters.

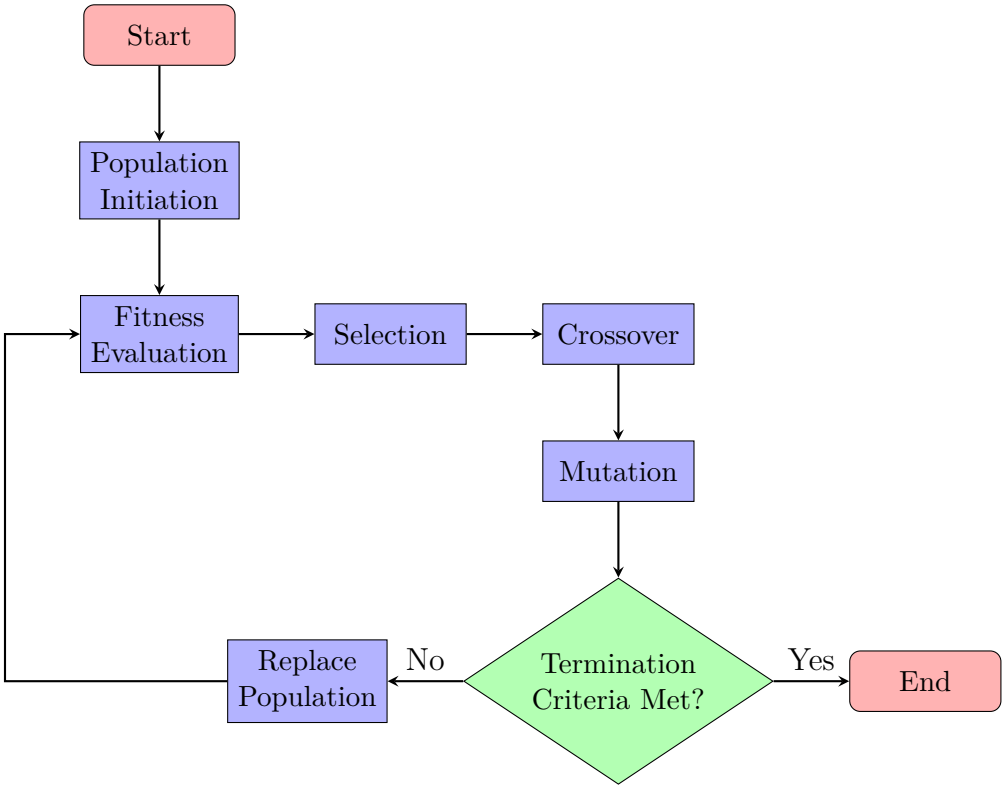

Figure 2.1: Flowchart of the Genetic Algorithm used for parameter optimization.

3

Pulse-spread Analysis

To determine whether the observed transport dynamics of neurofilaments (including bi-directionality, pausing, and anterograde bias) in mice is comparable to that in zebrafish, Bomont's lab at the NeuroMyoGène Institute (Lyon, France) replicated the pulse-spread experiment previously conducted in Boyer *et al.* [1]. However, the current experiment used a bundle of axons in nerves rather than a single axon as in [1]. The pulse-spread method is a variation of the pulse-escape technique developed in [46]. Unlike pulse-escape, which involves photoactivating a short segment of an axon and studying the movement of activated neurofilaments away from that region over time, pulse-spread monitors the amount of neurofilaments leaving at both ends of the activated region. This is achieved by using flanking windows, known as distal and proximal windows, at each end of the activated region (central window) as shown in Figure 3.1 [1]. The dynamics of the neurofilaments in these flanking windows were then analysed over time.

3.1 Pulse-spread model

To analyse pulse-spread experimental data, we use the approach developed in Boyer *et al.* [1] (Figure 3.1). For self-containment, we provide details of their approach.

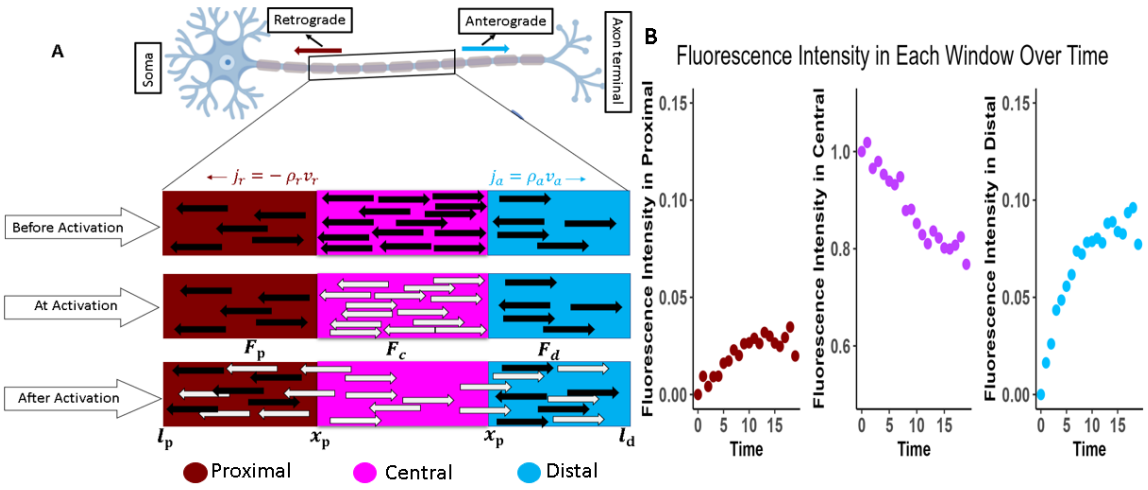

Figure 3.1: **Pulse-spread experiment set-up**. (A) Retrograde transport is directed toward the soma, while anterograde transport is toward the axon terminal. Their respective fluxes are given by $j_r = -v_r\rho_r$ and $j_a = v_a\rho_a$, where $v_r > 0$ and $v_a > 0$ represent the speeds, and ρ_r and ρ_a denote the neurofilament quantities per unit length in the retrograde and anterograde directions, respectively. The region between x_p and x_d (magenta) represents the central window. To the left of the central window is the proximal window (dark red), extending from l_p to x_p while to the right is the distal window (sky blue), starting from x_d to l_d. Note that $l_p < x_p < x_d < l_d$. The fluorescence of neurofilaments within the central window is activated; x_p and x_d are the spatial points where the activated neurofilaments exit the central window into the proximal and distal windows, respectively. The total fluorescence from the photoactivated neurofilaments in all three windows is recorded over time. The variables F_p, F_c, and F_d denote the quantities of fluorescent neurofilaments in the proximal, central, and distal windows, respectively. (B) The plots illustrate an example of normalized fluorescence in the respective windows over time $\tilde{F}_p(t)$, $\tilde{F}_c(t)$ and $\tilde{F}_d(t)$.

We let x be the location (measured in μm) along the length of the axon at each time t (measured in min), $\rho_a(x,t)$ and $\rho_r(x,t)$ be the quantity of fluorescent neurofilaments moving in anterograde (towards the axon terminal) and retrograde (towards the soma) direction per unit length and their speed are $v_a > 0$ and $v_r > 0$, respectively. The corresponding fluxes, which are the quantity of fluorescent neurofilaments passing a point per unit time, are $j_a = \rho_a(x,t)v_a$ and $j_r = -\rho_r(x,t)v_r$, respectively. Then, the total flux, $j(x,t)$ (measured in $(fluorescence)\text{min}^{-1}$, where $fluorescence$

represents the amount of photoactivated neurofilaments), is given by

$$j(x,t) = \rho_a(x,t)v_a - \rho_r(x,t)v_r = \rho(x,t)\bar{v}, \tag{3.1.1}$$

where $\rho(x,t)$ (measured in $(fluorescence)\mu\text{m}^{-1}$) is the quantity of all fluorescent neurofilaments per unit length at time t and $\bar{v}$ (measured in $\mu\text{m}(\text{min})^{-1}$) is the average velocity of neurofilaments at a particular location, which is defined as follows

$$\bar{v}(x,t) = \frac{\rho_a(x,t)}{\rho(x,t)}v_a - \frac{\rho_r(x,t)}{\rho(x,t)}v_r = p_a(x,t)v_a - p_r(x,t)v_r. \tag{3.1.2}$$

The variables p_a and p_r are the fractions of neurofilaments moving in anterograde and retrograde direction, respectively.

After photoactivation of neurofilaments in the central window in a pulse-spread experiment, the amount of fluorescent neurofilaments at time t in the central, proximal and distal windows respectively are $F_c(t)$, $F_p(t)$ and $F_d(t)$ (Figure 3.1B), respectively.

At the early activation period, the fluorescent neurofilaments exiting the central window are captured by the flanking windows. So, as the amount of fluorescence $F_c(t)$ declines in the central window, the fluorescence, $F_d(t)$ and $F_p(t)$, in the flanking windows have a corresponding increase. The rate of change of photoactivated neurofilaments in each window is given by

$$\begin{aligned}
\frac{dF_c}{dt} &= -\left(j_a(x_d,t) - j_r(x_p,t)\right) = -(\rho_a(x_d,t)v_a + \rho_r(x_p,t)v_r),\\
\frac{dF_p}{dt} &= -\, j_r(x_p,t) = \rho_r(x_p,t)v_r,\\
\frac{dF_d}{dt} &= j_a(x_d,t) = \rho_a(x_d,t)v_a,
\end{aligned} \tag{3.1.3}$$

where $\rho_a(x_d,t)$ and $\rho_r(x_p,t)$ are respectively, the quantity of fluorescent neurofilaments in anterograde and retrograde moving states at the distal and proximal ends

(i.e. x_d and x_p) of the central window as in Figure 3.1. These equations describe the decrease of fluorescent neurofilaments in the central window per unit time and the increase of fluorescent neurofilaments in the flanking windows per unit time. From system (3.1.3),

$$\frac{dF_c}{dt} + \frac{dF_p}{dt} + \frac{dF_d}{dt} = 0;$$

hence, the total amount of fluorescent neurofilaments is conserved over time

$$\forall t \geqslant 0, \quad F_c(t) + F_p(t) + F_d(t) = F_c(0) = a\rho(x, 0), \tag{3.1.4}$$

where $F_c(0)$ is the total fluorescence in the central window at the time of activation, a is the length of the central window and ρ is the quantity of photoactivated neurofilaments per unit length. Furthermore , based on biological observations, we assume that photoactivated neurofilaments are homogeneously distributed in space in the central window; so $\rho(x, 0) \equiv \rho$.

Therefore, normalizing the content of each window at a given time by the initial content in the central window

$$\tilde{F}_c(t) \equiv \frac{F_c(t)}{F_c(0)}, \quad \tilde{F}_d(t) \equiv \frac{F_d(t)}{F_c(0)}, \quad \tilde{F}_p(t) \equiv \frac{F_p(t)}{F_c(0)}$$

gives the following

$$\begin{aligned}
\frac{d\tilde{F}_c}{dt} &= \frac{-(\rho_a(x_d, t)v_a + \rho_r(x_p, t)v_r)}{a\rho} = -\frac{(p_a(x_d, t)v_a + p_r(x_p, t)v_r)}{a}, \\
\frac{d\tilde{F}_p}{dt} &= \frac{\rho_r(x_p, t)v_r}{a\rho} = \frac{p_r(x_p, t)v_r}{a}, \\
\frac{d\tilde{F}_d}{dt} &= \frac{\rho_a(x_d, t)v_a}{a\rho} = \frac{p_a(x_d, t)v_a}{a}.
\end{aligned} \tag{3.1.5}$$

The equations in (3.1.5) are in the form $\frac{dF}{dt}$ with the solution $F(t)$. Approximating

these solutions at the photoactivation time $t = 0$ by a Taylor's expansion gives,

$$F(t) \approx F(0) + \frac{dF(0)}{dt}t + \frac{d^2F}{dt^2}(0)t^2 + ... \tag{3.1.6}$$

Truncating this expansion at the second term from the higher orders gives,

$$F(t) \approx F(0) + \frac{dF(0)}{dt}t, \tag{3.1.7}$$

which is linear in t and the slope $\frac{dF(0)}{dt} = S$. Therefore, S can be estimated from data in a time frame in which the data follows a linear regime. Note from Figure 3.1B that a linear regime is exhibited in data at the early activation period where there is a decrease in the amount of photoactivated neurofilaments in the central window. At the same time, there is a corresponding linear increase in the amount of neurofilaments in the flanking windows. Applying (3.1.5) on (3.1.7), while noting that at $t = 0$ there are no fluorescent neurofilaments in flanking windows, all the fluorescent neurofilaments are still in the central window. Hence, $\tilde{F}_c(0) = 1$ and $\tilde{F}_p(0) = \tilde{F}_d(0) = 0$, we obtain

$$\begin{aligned}
\tilde{F}_c(t) &\approx \tilde{F}_c(0) - \frac{(p_a(x_d,0)v_a + p_r(x_p,0)v_r)}{a}t = 1 - S_c t, \\
\tilde{F}_p(t) &\approx \tilde{F}_p(0) + \frac{p_r(x_p,0)v_r}{a}t = S_p t, \\
\tilde{F}_d(t) &\approx \tilde{F}_d(0) + \frac{p_a(x_d,0)v_a}{a}t = S_d t,
\end{aligned} \tag{3.1.8}$$

where S_c is the slope estimated from the decrease of experimental fluorescence in the central window, and S_p and S_d are the slopes estimated from the increase in experimental fluorescence in the proximal and distal windows, respectively (Figure 3.1B). Hence, this modelling framework assumes that during the short period following activation - when the estimation of S is performed - there is no change in neurofilaments kinetics (i.e., no switching between directions of motion or transitions

into pausing) such that $p_a^s(x_d, 0) \equiv p_a^s(x_d)$ and $p_r^s(x_p, 0) \equiv p_r^s(x_p)$ where p_r^s and p_a^s are time-independent values (steady state values) of p_r and p_a respectively and we have

$$\begin{aligned} \frac{p_a^s(x_d)v_a + p_r^s(x_p)v_r}{a} &\equiv S_c, \\ \frac{p_r^s(x_p)v_r}{a} &\equiv S_p, \\ \frac{p_a^s(x_d)v_a}{a} &\equiv S_d. \end{aligned} \tag{3.1.9}$$

Then, combining (3.1.2) and (3.1.9) gives an estimate of the average velocity

$$\bar{v} = a(S_d - S_p) \tag{3.1.10}$$

and from (3.1.8) the ratio of the quantity of photoactivated neurofilaments moving in an anterograde and retrograde direction

$$\frac{S_d}{S_p} = \frac{p_a^s(x_d)v_a}{p_r^s(x_p)v_r}. \tag{3.1.11}$$

If this ratio is greater than one then more filaments move in the anterograde direction otherwise more moves in the retrograde direction.

Hence, the model framework developed by Boyer *et al.* [1] allows to estimate the directional bias and mean velocity of neurofilaments based on the increase in fluorescence in the adjacent windows of the photoactivated region. These estimates are valid at the early time of activation and assumed that there is no change in the dynamics of neurofilaments - no switching in direction nor between mobile and pausing states.

3.2 Data Analysis

3.2.1 Experimental Data

To investigate axonal neurofilaments transport, our collaborators (Bomont's lab) employed the pulse-spread method, a fluorescence photoactivation technique that enables tracking of neurofilaments movement [1, 2, 30]. Neurofilaments were labeled with a fluorescent marker within a defined central window, and their redistribution into proximal and distal flanking windows was tracked via time-lapse fluorescence microscopy. Fluorescence intensity changes in these windows were quantified at high temporal resolution, with recordings taken every 0.5 minutes for the experiments comparing central window length, while some datasets (e.g., those involving aging effects) were recorded every 1 minute.

Due to inherent variability in neurofilaments content among individual axons [46], fluorescence intensities varied across experiments. To enable consistent comparisons, we normalized the fluorescence intensities in each window relative to the initial intensity of the central activation window at the start of the experiment. This normalization ensures a standardized assessment of neurofilaments transport dynamics across different axons [1, 46].

We had access to pulse-spread measurements across all windows for 13 to 15 axons, depending on the conditions. We considered the data either individually or as averaged values at each time point. Fitting can be performed on the averaged data or separately for each bundle of axons in each fish for each experiment. For this analysis, we opted for an averaged approach, summarizing the results in an error bar plot (Figure 3.2). The fluorescence at each time point is represented as mean values with confidence intervals (CI) to account for measurement variability. The confidence intervals were computed as $\text{CI} = \text{mean} \pm 1.96 \times \frac{\text{SD}}{\sqrt{n}}$, where SD is the standard deviation of fluorescence at a given time point, and n is the number of data

points contributing to the mean (e.g., $n = 13$). The factor 1.96 corresponds to a 95% confidence level, assuming normally distributed data.

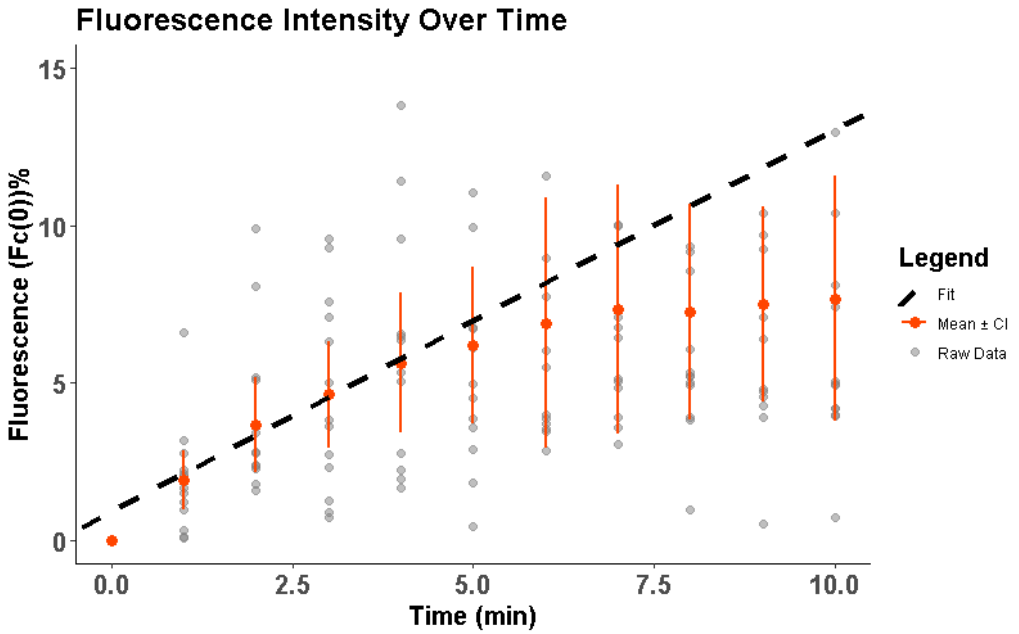

Figure 3.2: **Fitting of averaged fluorescence data.** The plot shows the mean fluorescence intensity across 13 axons at each time point, with orange error bars representing the 95% confidence interval (mean $\pm$ 1.96 $\times$ $\frac{\text{SD}}{\sqrt{13}}$). Gray points are individual data points, and the black dashed line represents the linear model (3.1.8) fitted to the mean data (orange points) to estimate the rate of fluorescence change due to neurofilaments transport.

The experiment was conducted with varying window configurations to assess the influence of window length on the quantification of neurofilaments movement, as illustrated in Figure 3.1. The central window length ($x_p - x_d = a$) was set to either 5 μm or 15 μm, while the flanking window lengths ($l_p - x_p$ for proximal and $x_d - l_d$ for distal) were varied at 2 μm, 5 μm, 10 μm, and 15 μm. This setup allowed us to evaluate how window size affects the capture of fluorescent neurofilaments. To determine the optimal flanking window length for analysis, we fitted (3.1.8) to the fluorescence intensity data in each window. As the flanking window length increased, the rates of fluorescence entry (S_p and S_d) into each window also increased, with the rates for 10 μm and 15 μm windows almost coinciding and fluorescence curves exhibiting a linear

regime up to approximately 2 minutes, as shown in Figure 3.4 A, B, D, E. Smaller windows (2 μm and 5 μm) captured less fluorescence, indicating that some activated neurofilaments already exited flanking windows during the observation period. Using these smaller windows leads to an underestimation of the neurofilaments transport parameters [1]. Since the rates in the 10 μm and 15 μm windows were equivalent, we selected the 10 μm (Figure 3.4 G, H) flanking window for our analysis to ensure that we did not miss some of the activated neurofilaments from the central window.

3.2.2 Photobleaching Correction

In Bomont's lab experimental data, addressing the challenge of photobleaching is crucial, as highlighted in [30]. Photobleaching is an inherent limitation in fluorescence-based imaging, where the fluorescent signal diminishes with time due to the loss of fluorescence in proteins [83] or due to the reduction of the light intensity of the microscope used for the experiment.

In our study, this phenomenon poses a specific obstacle: we expect the total fluorescence of activated neurofilaments within the central window to equal the sum across all windows at any given time, provided they remain within the central and flanking windows. However, as time progresses, photobleaching causes a reduction in observed fluorescence, disrupting this conservation, as shown in Figure 3.3A. Consequently, this affects the reliability of our data, hindering our ability to fit the model to the data and obtain accurate parameter estimates.

To address this issue, a photobleach correction was essential. We fitted the pulse-spread data from Bomont's lab to the photobleach decay equation, $y_t = y_0 e^{-\omega t}$, where y_0 is the initial fluorescence intensity (at $t = 0$) in the central window after activation, ω is the unknown bleaching rate, and t is time (Figure 3.3B). This function is fitted to the total fluorescence in the three windows during the time period in which no fluorescence has left the flanking windows (blue points in Figure 3.3B,

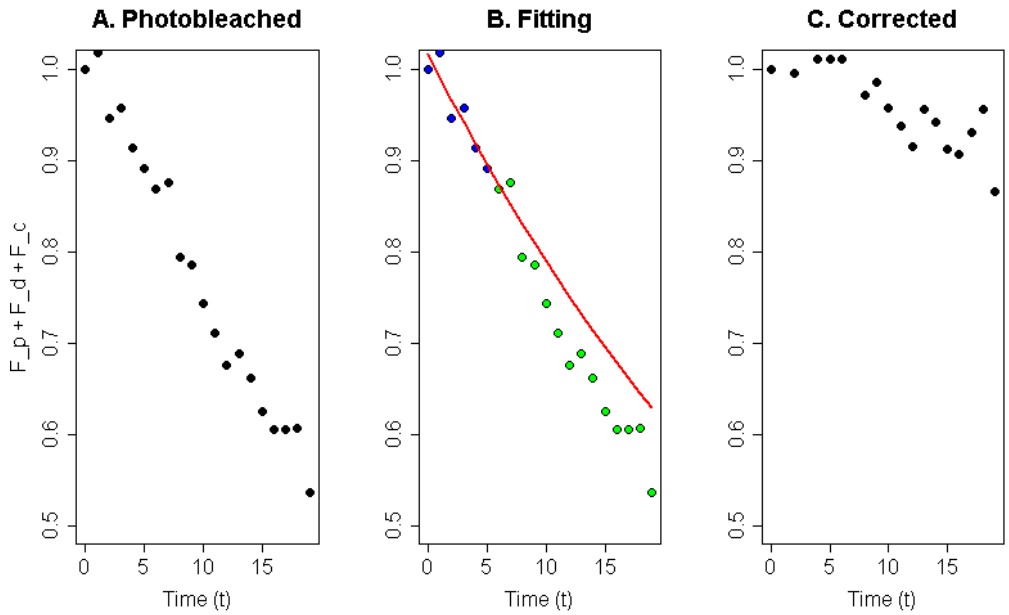

Figure 3.3: **Photobleaching correction in fluorescence data.** (A) Actual total fluorescence data from proximal, central, and distal windows before correction, showing the decline due to photobleaching over time. (B) Photobleach fitting: blue points represent total fluorescence within the first 5 minutes, when fluorescence remains in the flanking windows; green points indicate time points when fluorescence starts exiting the flanking windows; the red curve is the fitted photobleach decay model $y_t = y_0 e^{-\omega t}$ up to 20 minutes. (C) Corrected fluorescence data after applying the photobleach correction factor $e^{\omega t}$, restoring the expected fluorescence dynamics.

up to 5 minutes). The red curve represents the fitted photobleach decay model. By fitting our actual data to this equation, we extracted the bleaching rate ω and subsequently applied a correction factor, $e^{\omega t}$, to the experimental data [1, 30]. This adjustment effectively mitigates the influence of photobleaching, restoring a more accurate representation of the fluorescent neurofilaments over time (Figure 3.3C, upto 5 minutes). Beyond 4–5 minutes, it is observed in Figure 3.3C that the sum of fluorescent neurofilaments in all windows is less than one. This is because by that point neurofilaments will have started exiting the flanking windows, so the sum will be less than the initial amount that was photoactivated in the central window. Using this corrected dataset, we proceeded with model fitting to estimate parameter values, ensuring that our results more accurately reflect the dynamics of

neurofilaments transport.

3.2.3 Estimation of Fluorescence Slopes

To estimate the rates of change—i.e., the slopes (S_p, S_d and S_c)—of fluorescent neurofilaments content in the proximal, central and distal windows, we fitted the linear models in (3.1.8) to photobleaching-corrected data for individual axons (13 to 15 in total) for all windows, within the time range where the signal exhibited a linear trend. Rather than presenting individual axon fits, which would be cumbersome, we summarized the results using the mean and confidence intervals across axons, as shown in Figure3.2. This approach allows for a compact yet informative representation of early transport dynamics across multiple axons. The resulting slope estimates from the individual axons for the central, proximal, and distal windows were then extracted and analysed (e.g., Figure 3.5).

3.2.4 Results

Our work is a preliminary study aimed at identifying optimal parameters for the experimental setup. We analysed the pulse-spread data to investigate the behaviour of neurofilaments in zebrafish, effects of central window length on the quantifacation of transport dynamics and the effect of age on axonal transport.

The analysis revealed that neurofilaments transport is bidirectional as fluorescent neurofilaments were recorded in both proximal and distal flanking windows, as shown in Figure 3.1 B. The rates of fluorescence increase in the proximal (S_p) and distal (S_d) flanking windows, along with the rate of decrease in the central window (S_c), were determined by fitting the (3.1.8) to the data of 15 axons and presented (as described in Section 3.2.3) in Figure 3.4. These rates or slopes quantify the movement of neurofilaments into and out of each window. Analysis of the 15 axon bundles revealed that the rate of fluorescence increase in the distal window (S_d) con-

sistently exceeded that in the proximal window (S_p), as depicted in the box plots of slopes in Figure 3.5 (first row: S_p, S_d, S_c). This indicates that more neurofilaments move in the anterograde direction (distal) than in the retrograde direction (proximal). The positive net velocity, calculated using (3.1.10) and shown in Figure 3.5, further supports this finding. Additionally, the average ratio, computed via (3.1.11), exceeds 1 (red horizontal line in Figure 3.5 S_d/S_p), confirming the predominance of anterograde movement.

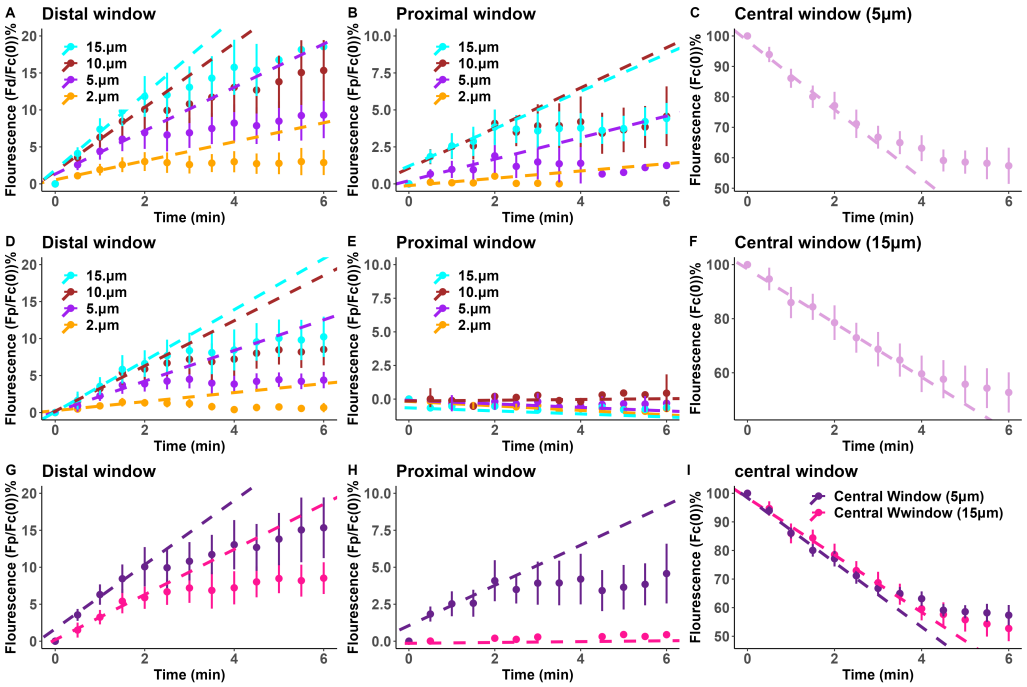

Figure 3.4: **Fluorescence intensity fitting for 5 μm and 15 μm central windows.** The plots illustrate the fluorescence intensity dynamics in different window sizes. Panels A, B, and C correspond to the 5 μm central window data fitting, while panels D, E, and F represent the 15 μm central window data fitting. Panels A, B, D and E are the data fitting of varying flanking window lengths 2μm, 5 μm, 10 μm and 15 μm. Panels G, H and I compare the fitting of 5 μm and 15 μm central window length and 10 μm flanking window. The error bars indicate the mean fluorescence intensity $\pm$ 95% confidence interval from 15 axon bundles at each time point. The dashed lines represent model fits through the mean fluorescence values.

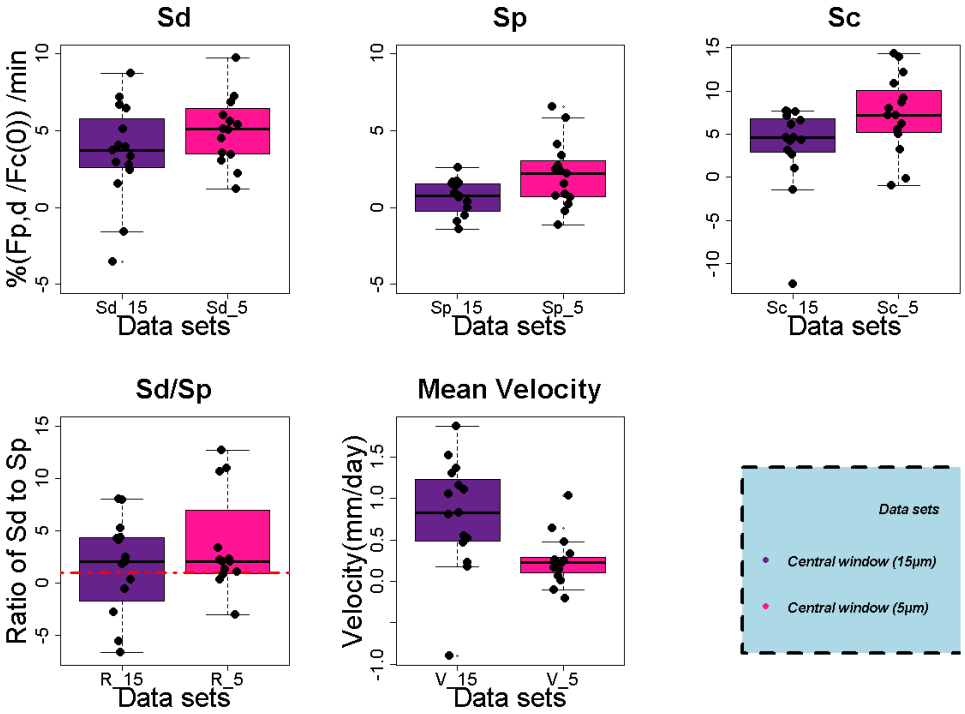

Figure 3.5: **Pulse spread slopes analysis.** This figure compares the slopes of neurofilaments transport in the proximal (S_d), distal (S_p), and central (S_c) windows for central window sizes of 15 μm and 5 μm. The ratio of distal to proximal slopes (S_d/S_p) and the mean neurofilaments transport velocity are also shown for both conditions. Each black dot represents data from an individual axon. The box plots indicate the upper and lower quartiles, the median, and the whiskers represent the minimum and maximum values. The horizontal red line in the S_d/S_p plot marks a ratio of 1, highlighting relative differences in transport between the two slopes.

1. Effects of Different Central Window Length

In comparing the effect of the different central window lengths, it can be observed that the average rate of increase of fluorescent neurofilaments in the flanking windows is always higher in 5μm than in 15μm central window length and the rate of decrease in fluorescent neurofilaments in the central window is relatively higher in 5μm than in 15μm (Figure 3.5 and 3.4). This confirmed what is alluded to in [1] that longer central windows provide a greater opportunity for on-track filaments to reside longer before exiting, resulting in the quantification of a slower departure rate.

2. Slowing of Neurofilament Transport with Age

An intriguing phenomenon from numerous studies has been the gradual slowing down of neurofilaments transport over time [1, 37, 84]. According to computational modelling in [3], the slowing of neurofilaments transport in the mouse sciatic nerve may result from longer pauses or a shift in the proportion of anterograde to retrograde movement. Additionally, studies indicate that as an organism age, the density of the microtubule on which neurofilaments are transported decreases, and neurofilaments take a longer time to find their tract, lengthening the pausing period and decreasing overall velocity [4]. To determine whether this observation is true for zebrafish, our collaborator performed pulse-spread experiments on 13 bundles of axons of the fish at different ages, i.e. 72, 96 and 120 hours post-fertilization (hpf). The amount of fluorescent neurofilaments in the central window of size $15\mu m$ and flanking windows of size $10\mu m$ was quantified and fitted to the respective (3.1.8). The fitting described in Section 3.2.3 was applied, and the data exhibited linear behaviour up to approximately $4-5$ minutes (Figure 3.6). The dashed lines in the figure represent the linear fits corresponding to the respective windows, based on (3.1.8). The slopes (S_d, S_p, S_c) were extracted and analysed. At 72 and 96 hpf, the distal rate S_d appears higher than the proximal rate S_p. However, within each slope group, there is no significant difference between 72 and 96 hpf. Furthermore, there is a decrease in the average distal rate from 1.40min^{-1} to 0.64min^{-1} between 72 and 120 hpf and the average proximal rate increases from 0.50min^{-1} to 1.45min^{-1}. This has led to the corresponding decrease in their mean velocities from 0.23mm(day)^{-1} to about -0.20mm(day)^{-1} (Figure 3.7). It can also be observed from the central window that the average rate at which fluorescent neurofilaments leave slows down over the same period (Table 3.1). These results confirm that the anterograde bias in neurofilament transport in zebrafish decreases with age and, in this case, even reverses toward retrograde dominance. This trend is evident from the average slope ratio (S_d/S_p),

which remains above one at 72 and 96 hpf, but drops below one by 120 hpf, as shown by the red line in Figure 3.7.

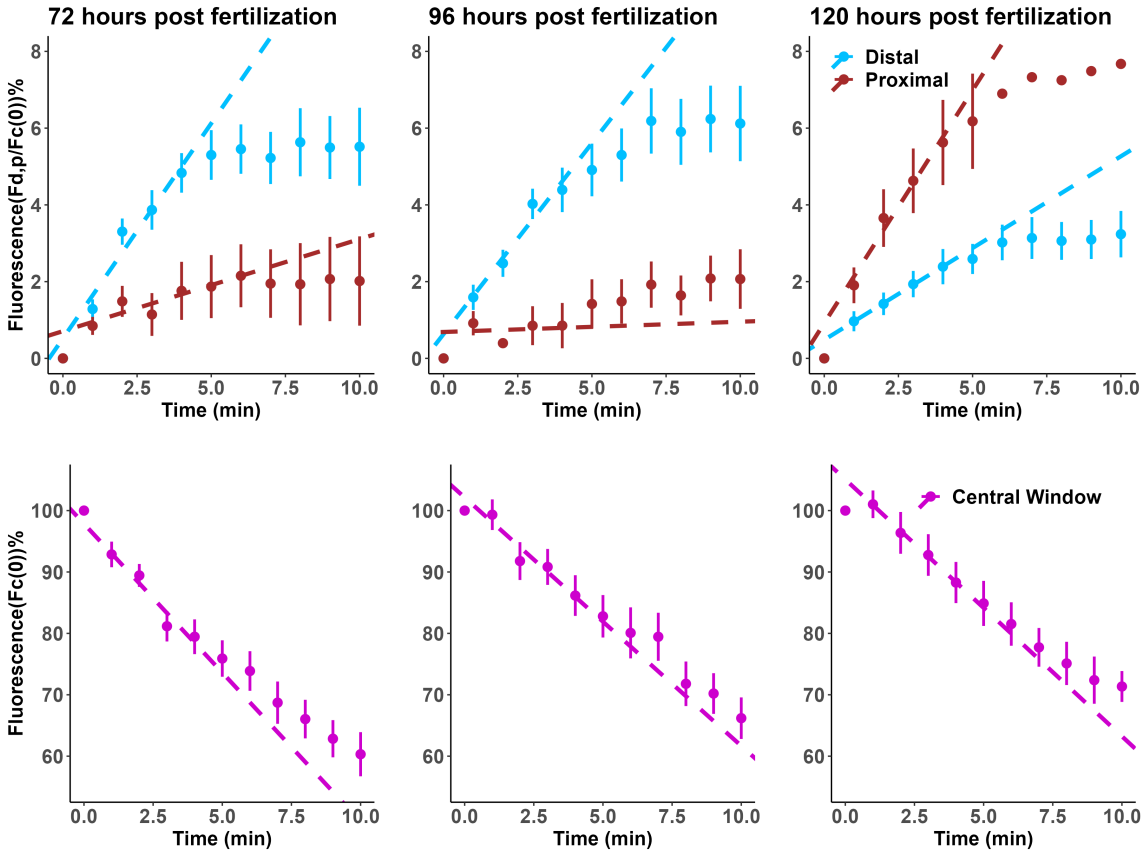

Figure 3.6: **Fluorescence intensity fitting at** 72**,** 96**, and** 120 **hpf.** Each column represents data for a specific age group, showing the fluorescence intensity changes in the flanking windows (top row) and the corresponding central window (bottom row) over time. The blue and brown markers in the top row represent the distal and proximal flanking windows, respectively, while the magenta markers in the bottom row represent the central window. The dashed lines indicate fitted equations. Error bars represent 95% confidence interval around the mean. Data were collected from 13 bundles of axons, with dots indicating the mean fluorescence intensity at each time point.

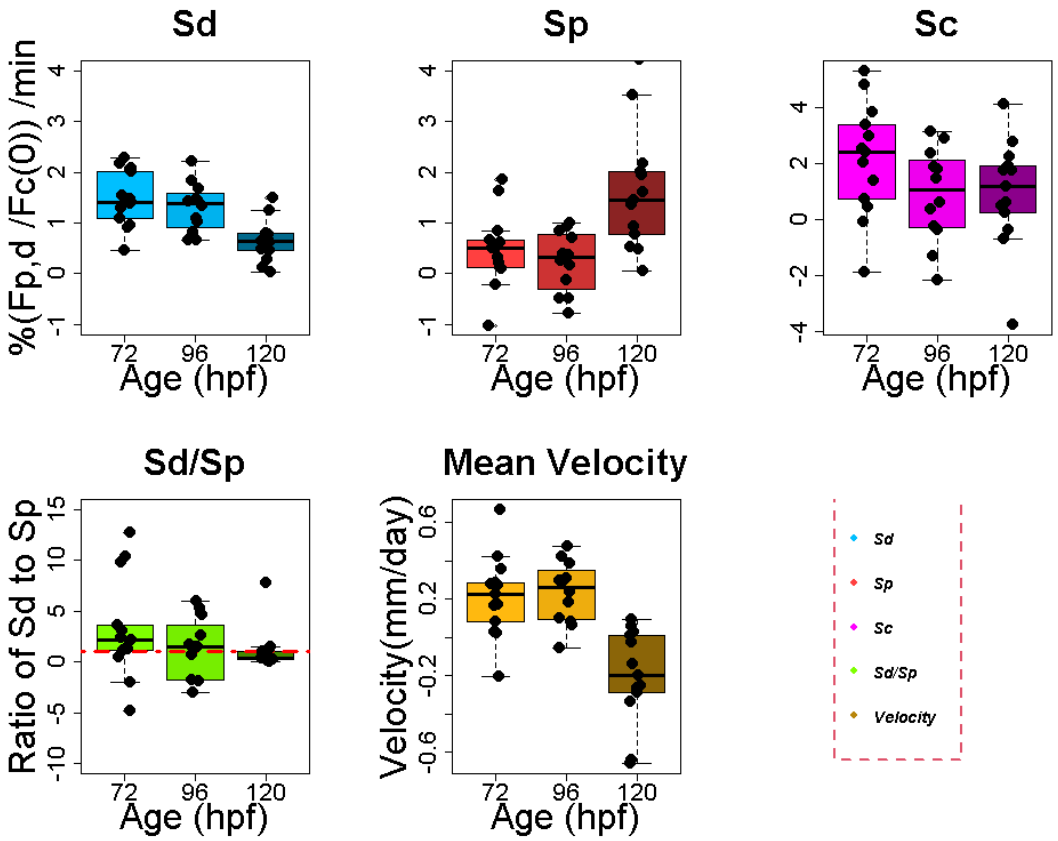

Figure 3.7: **Box plot of neurofilaments transport across developmental stages.** The upper row presents box plots of the slopes S_d, S_p, and S_c at different ages (72, 96, and 120 hours post-fertilization, hpf). Each black dot represents the slope of an individual axon. The lower row illustrates the ratio of S_d to S_p and the mean velocity across ages. The results indicate that, on average, S_d decreases with age, whereas S_p increases. This trend is reflected in the decreasing S_d/S_p ratio and the decline in mean velocity over time.

Table 3.1: The quantitative information collected from the data analysis.

Age (hpf)	$S_d(\text{min}^{-1})$	$S_p(\text{min}^{-1})$	$S_c(\text{min}^{-1})$	S_d/S_p	Mean velocity (mm(day)^{-1})
72	1.40	0.50	2.41	2.20	0.23
96	1.39	0.32	1.10	1.50	0.26
120	0.64	1.45	1.18	0.4	-0.20

4

Modelling Neurofilament Transport Dynamics

Neurofilaments are cargos of axonal transport that move along microtubules, which serve as tracks [2]. Neurofilaments can be in either an on-track or off-track state. In the on-track state, they move in the anterograde (towards the axon terminal) or retrograde (towards the soma) direction, as illustrated in Figure 1.1. In either the anterograde or retrograde state, neurofilaments exhibit short bouts of movement interspersed with brief pauses and can also switch direction. Conversely, in the off-track state, neurofilaments detach from their track and pause for an extended period (at least 60 minutes) before reattaching and resuming movement in either direction [2, 3, 46].

4.1 Models for Axonal Transport of Neurofilaments

In our models, we assume that neurofilaments can transition to the off-track state from either the moving or short-pausing states, and vice versa. Additionally, we assume that diffusion occurs only in the off-track state. Consequently, we categorize neurofilaments in the axon into four classes: on-track populations, including the

anterograde (A), retrograde (R), and short-pause (P_S) populations; and the off-track population, consisting solely of the long-pause population (P_L), (see Figure 1.1).

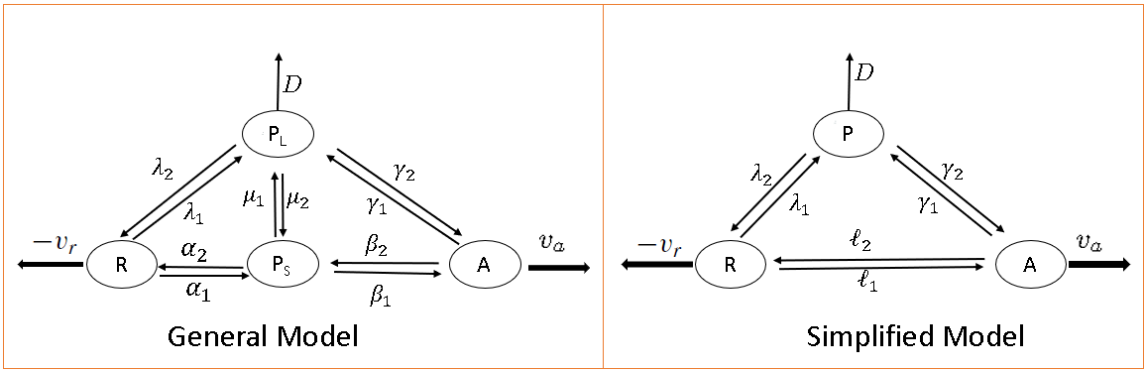

Figure 4.1: **Models of neurofilaments transport in the axon.** In the general model, the P_S compartment represents short on-track pauses lasting less than 30 seconds and is considered a normal part of the moving population. In the simplified model, the sole pausing compartment P corresponds to the P_L compartment related to long off-track pauses in the general model. The transition rates are defined as follows: α_1 and α_2 govern switching between R and P_S; λ_1 and λ_2 govern switching between R and P_L or P; μ_1 and μ_2 govern switching between P_S and P_L; β_1 and β_2 govern switching between P_S and A; γ_1 and γ_2 govern switching between A and P_L or P; ℓ_1 and ℓ_2 govern direct switching between A and R; D is the diffusion rate; and v_r and v_a are the retrograde and anterograde velocities, respectively.

In the general model of Figure 4.1, the variables P_L and P_S represent the long and short pausing states, respectively, while A and R denote the anterograde and retrograde moving states with velocities v_a and v_r. The diffusion constant D applies to off-track neurofilaments. We assume that microtubules (tracks along which motor proteins transport neurofilaments) are arranged in parallel, allowing the dynamics of neurofilaments movement to be modelled in one dimension; hence, the general model is considered on a one-dimensional spatial domain and x represents the position along the axon, with $x = 0$ at the soma and $x = L$ at the axon terminal, where L is the axon length. All state variables have units of population (quantity of neurofilaments, which is proportional to fluorescence), x is measured in μm, v_a and v_r in $\mu\text{m}(\text{min})^{-1}$, and D in $\mu\text{m}^2(\text{min})^{-1}$.

Table 4.1: **Variables and parameters used in the models.** The table lists all variables, parameters, their definitions, and units in the models.

Variables	**Definition**	**Units**
A	Population of neurofilaments in anterograde motion	Population
R	Population of neurofilaments in retrograde motion	Population
P_S	Population of neurofilaments in short pausing state	Population
P_L	Population of neurofilaments in long pausing state	Population
P	Population of neurofilaments in pausing states	Population
Parameters	**Definition**	**Units**
D	Diffusion rate	$\mu\text{m}^2(\text{min})^{-1}$
v_a	Velocity of neurofilaments in anterograde motion	$\mu\text{m}(\text{min})^{-1}$
v_r	Velocity of neurofilaments in retrograde motion	$\mu\text{m}(\text{min})^{-1}$
α_1	Rate of switching from R to P_S	min^{-1}
α_2	Rate of switching from P_S to R	min^{-1}
β_1	Rate of switching from P_S to A	min^{-1}
β_2	Rate of switching from A to P_S	min^{-1}
γ_1	Rate of switching from A to P_L	min^{-1}
γ_2	Rate of switching from P_L to A	min^{-1}
λ_1	Rate of switching from R to P_L	min^{-1}
λ_2	Rate of switching from P_L to R	min^{-1}
μ_1	Rate of switching from P_S to P_L	min^{-1}
μ_2	Rate of switching from P_L to P_S	min^{-1}
ℓ_1	Rate of direct switching from R to A	min^{-1}
ℓ_2	Rate of direct switching from A to R	min^{-1}

The spatial transport dynamics are modelled using partial differential equations that distinguish between diffusive and advective processes. We assume long pausing neurofilaments undergo diffusion described by $\frac{\partial P}{\partial t} = D\frac{\partial^2 P}{\partial x^2}$, where D is the diffusion constant. Mobile populations exhibit advective transport: anterograde neurofilaments follow $\frac{\partial A}{\partial t} = -v_a \frac{\partial A}{\partial x}$ and retrograde neurofilaments follow $\frac{\partial R}{\partial t} = v_r \frac{\partial R}{\partial x}$, where v_a and $-v_r$ are the respective transport velocities along the spatial coordinate x. The full equations of the general model from Figure 4.1 are:

$$\frac{\partial P_S}{\partial t} = -(\alpha_2 + \beta_1 + \mu_1)P_S + \mu_2 P_L + \alpha_1 R + \beta_2 A,$$

$$
\begin{aligned}
\frac{\partial P_L}{\partial t} &= D\frac{\partial^2 P_L}{\partial x^2} + \mu_1 P_S - (\gamma_2 + \lambda_2 + \mu_2)P_L + \lambda_1 R + \gamma_1 A, \\
\frac{\partial A}{\partial t} &= -v_a\frac{\partial A}{\partial x} + \beta_1 P_S + \gamma_2 P_L - (\beta_2 + \gamma_1)A, \\
\frac{\partial R}{\partial t} &= v_r\frac{\partial R}{\partial x} + \alpha_2 P_S + \lambda_2 P_L - (\alpha_1 + \lambda_1)R.
\end{aligned} \tag{4.1.1}
$$

All variables and parameters are listed in Table 4.1 and considered non-negative.

To achieve a manageable framework for analysis, we simplified the general model by reducing the number of parameters and variables while preserving key dynamical properties. Based on previous findings [46, 57, 85], which indicate that neurofilaments pause on-track (P_S) for an average of 30 seconds and off-track (P_L) for at least one hour, we assume that short pauses (P_S) are an inherent aspect of the actively transported populations (A and R). Therefore, the anterograde and retrograde short-pause states (P_S) are incorporated into the A and R populations, respectively, while the long-pause state (P_L) is retained as a distinct pausing compartment (P) representing off-track neurofilaments. This aggregation is reflected in the simplified model shown in Figure 4.1. The equations of the simplified model are:

$$
\begin{aligned}
\frac{\partial P}{\partial t} &= D\frac{\partial^2 P}{\partial x^2} - (\lambda_2 + \gamma_2)P + \lambda_1 R + \gamma_1 A, \\
\frac{\partial A}{\partial t} &= -v_a\frac{\partial A}{\partial x} + \gamma_2 P + \ell_1 R - (\ell_2 + \gamma_1)A, \\
\frac{\partial R}{\partial t} &= v_r\frac{\partial R}{\partial x} + \lambda_2 P - (\lambda_1 + \ell_1)R + \ell_2 A.
\end{aligned} \tag{4.1.2}
$$

The spatial domain representing the axon is $0 \leqslant x \leqslant L$. At the boundaries $x = 0$ (soma) and $x = L$ (axon terminal), we assume zero flux of neurofilaments. The boundary and initial conditions for the simplified model are defined as follows:

- **Boundary Conditions:** We assume that there is no flux of neurofilaments at the boundaries. For the pausing population P, which undergoes diffusion, and the moving populations A and R, which are advective, the homogeneous

Neumann boundary condition (zero flux) is applied:

$$\left.\frac{\partial P}{\partial x}\right|_{x=0,L} = \left.\frac{\partial A}{\partial x}\right|_{x=0,L} = \left.\frac{\partial R}{\partial x}\right|_{x=0,L} = 0.$$

- **Initial Conditions:** At $t = 0$, the neurofilaments are distributed in the axon according to a continuous function $f(x)$. Hence, $P(x, 0) = P_0 f(x)$, $A(x, 0) = A_0 f(x)$, and $R(x, 0) = R_0 f(x)$, where P_0, A_0 and R_0 are the initial amount of P, A and R of total neurofilaments in its respective compartment.

After developing the simplified model, we derive four sub-models: one focusing on pure transport of neurofilaments in the pulse-spread protocol, assuming negligible exchange during this period [2], another focusing on pure exchange between compartments and the last being a transport-exchange (reversible and irreversible pausing) model. The pure transport model extends the classical Boyer's pulse-spread model [1], presented in Chapter 3, which describes movement in the linear phase without accounting for changes in neurofilaments dynamics or a pausing population. Unlike Boyer's model, our formulation explicitly incorporates pauses and explores the fit of the model beyond the linear phase. The pure exchange model isolates the switching dynamics between compartments, independent of spatial transport. Rather than pulse-spread protocol, which explores the dynamics of photoactivated neurofilaments out of a segment of the axon over a short period of time, the pure exchange model considers fluorescent neurofilaments homogeneously distributed over the entire axon and investigates the dynamics of their motile and non-motile states over a long time. This is due to the fact that the impact of reversal between anterograde and retrograde states is felt over a long time [2] and off-tract pausing of neurofilaments takes a long time to go on-tract. The separation of the pure exchange model enables us to examine whether the exchange process exhibits stable repartition between the motile and non-motile states, its resilience (time to recover from perturbations) and

reactivity (whether perturbations are amplified before stabilizing). The transport-exchange model examines the effect of transitions between on-track and off-track states on the pure transport model, to determine whether incorporating exchange dynamics impacts the model's ability to capture neurofilaments dynamics. By so doing, we aim to better understand the roles of transport and exchange in shaping the distribution and dynamics of neurofilaments in axons.

4.2 Pure Transport

To extract information about neurofilaments dynamics over short timescales (seconds to minutes), we analyse their early behaviour following photoactivation. During this period—from the moment of photoactivation in the central window until the fluorescent neurofilaments begin to exit the flanking windows—we assume no exchange occurs between the anterograde (A), retrograde (R), and pausing (P) compartments.

This assumption is supported by experimental findings: the reversal rate between A and R is extremely low over short timescales [86, 87, 88], and neurofilaments that pause off-track remain immobile for prolonged durations, often on the order of hours [46, 57, 85]. Consequently, in the context of pulse-spread experiments, switching between compartments is negligible. This implies that neurofilaments either undergo directed transport (anterograde or retrograde) or remain in the pausing state.

Previous studies (e.g., [1]) have established that active transport is the dominant mechanism responsible for the observed movement of fluorescent neurofilaments into distal and proximal regions, while diffusion is negligible under these experimental conditions.

To describe neurofilaments dynamics along the axon, we introduce a general function $f(x)$ representing the initial spatial distribution of neurofilaments across different transport states in the entire axon. Thus, the system (4.1.2) for the general

distribution case takes the form:

$$\begin{aligned} \frac{\partial P}{\partial t} &= 0, & P(x,0) &= P_0 f(x), \\ \frac{\partial A}{\partial t} &= -v_a \frac{\partial A}{\partial x}, & A(x,0) &= A_0 f(x), \\ \frac{\partial R}{\partial t} &= v_r \frac{\partial R}{\partial x}, & R(x,0) &= R_0 f(x). \end{aligned} \tag{4.2.1}$$

Here, $P(x,0)$, $A(x,0)$, and $R(x,0)$ are the initial conditions representing the repartition of fluorescent neurofilaments in the pausing, anterograde, and retrograde states, respectively. The constants P_0, A_0, and R_0 represent the "proportions" of fluorescent neurofilaments in the pausing, anterograde, and retrograde states, respectively. For generality, the dimensionless or normalized function $f(x)$ satisfies:

$$\int_{-\infty}^{\infty} f(x)\, dx = 1.$$

Note that for the pure transport model, the spatial domain is assumed to be unbounded.

In the specific case of pulse-spread experiments, $f(x)$ describes the initial distribution of photoactivated neurofilaments in the central activation window and takes the form of a smoothed step function to represent the photoactivation region:

$$f(x) = \left(\frac{1}{1 + \exp\left(-h(x - x_p)\right)} - \frac{1}{1 + \exp\left(-h(x - x_d)\right)} \right), \tag{4.2.2}$$

where x_p, and x_d are fixed parameters defining the boundaries of the photoactivation region (central window), as illustrated in Figure 4.2. Specifically, $x_p = 15\,\mu$m and $x_d = 30\,\mu$m correspond to the proximal and distal edges of the central window, and h controls the steepness of the transition.

At time $t = 0$, the total fluorescence in the central window is given by:

$$
\begin{aligned}
F_C(0) &= \int_{-\infty}^{\infty} \left[P_0 f(x) + A_0 f(x) + R_0 f(x)\right] dx \qquad (4.2.3)\\
&= \int_{x_p}^{x_d} \left[P_0 \left(\frac{1}{1+\exp\left(-h(x-x_p)\right)} - \frac{1}{1+\exp\left(-h(x-x_d)\right)} \right) \right.\\
&\quad + A_0 \left(\frac{1}{1+\exp\left(-h(x-x_p)\right)} - \frac{1}{1+\exp\left(-h(x-x_d)\right)} \right)\\
&\quad \left. + R_0 \left(\frac{1}{1+\exp\left(-h(x-x_p)\right)} - \frac{1}{1+\exp\left(-h(x-x_d)\right)} \right) \right] dx\\
&= \int_{x_p}^{x_d} (P_0 + A_0 + R_0) \left(\frac{1}{1+\exp\left(-h(x-x_p)\right)} - \frac{1}{1+\exp\left(-h(x-x_d)\right)} \right) dx\\
&= (P_0 + A_0 + R_0) \int_{x_p}^{x_d} f(x)\, dx. \qquad (4.2.4)
\end{aligned}
$$

Thus, we define:

$$P_0 + A_0 + R_0 = N,$$

where $N = \frac{F_c(0)}{x_d - x_p}$ represents the initial total quantity of fluorescent neurofilaments per unit length in the central window at the time of activation.

This approach enables us to gain insights into the nature of transport in photoactivated neurofilaments. Specifically, it allows us to estimate key parameters such as the anterograde velocity (v_a), retrograde velocity (v_r), and the "proportions" of photoactivated neurofilaments that are pausing (P_0), moving anterogradely (A_0), and moving retrogradely (R_0). These estimates are crucial for determining whether the proportion of pausing neurofilaments is significant.

4.3 Pure Exchange

Neurofilaments reversals between anterograde and retrograde states are rare over short timescales, with estimated rates below $1 \times 10^{-4}\,\mathrm{s}^{-1}$ [2, 86, 88]. Additionally, off-track neurofilaments often pause for extended periods, typically hours [46, 57, 85],

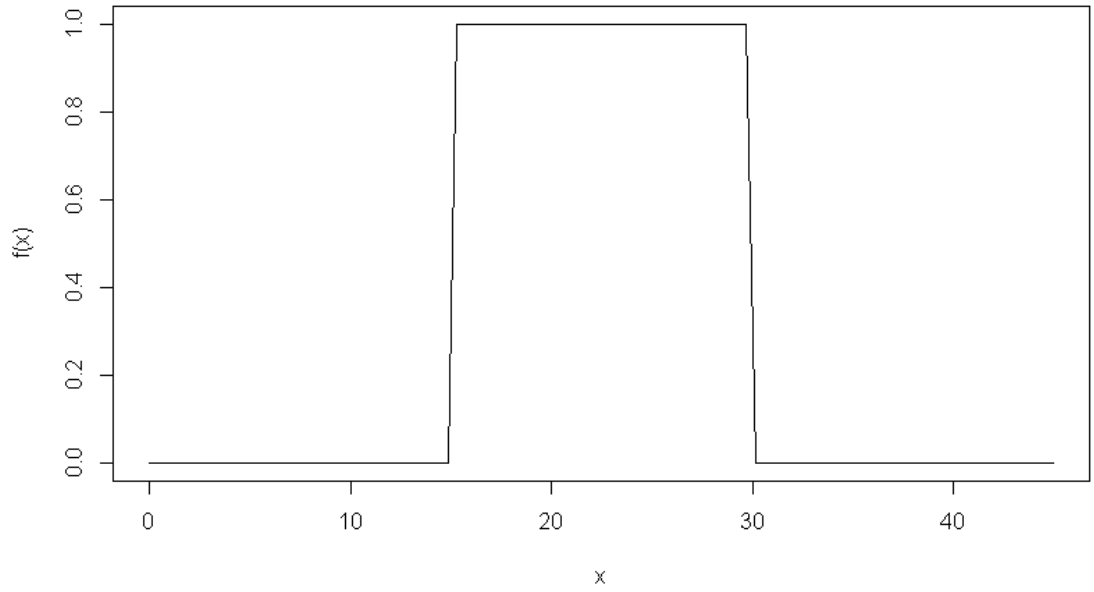

Figure 4.2: **Initial distribution of photoactivated neurofilaments in the pulse-spread experiment.** The plot shows the setup at the start of the experiment, where the proximal window $(0 - 15\,\mu\text{m})$ and distal window $(30 - 45\,\mu\text{m})$ contain no photoactivated neurofilaments, while the central window $(15 - 30\,\mu\text{m})$ contains all the fluorescent neurofilaments, as defined by the function $f(x)$ (4.2.2).

suggesting that switching events significantly influence neurofilaments organization over long periods rather than short timescales (seconds to minutes). Consequently, instead of relying on a pulse-spread protocol, which captures dynamics over brief intervals, we focus on a pure exchange model across the entire axon over extended timeframes.

The simplified model (4.1.2) incorporates both spatial transport (via diffusion D and velocities v_a, v_r) and state transitions (via rates λ_1, λ_2, γ_1, γ_2, ℓ_1, ℓ_2). However, this simultaneous consideration of transport and exchange complicates the analysis of exchange dynamics in isolation. To address this, we consider the relative timescales: by assuming that in extended time, transport rates (D, v_a, v_r) are significantly slower than switching rates (λ_i, γ_i, ℓ_i), the spatial transport terms become negligible. Under

these assumptions, the following system describing pure exchange dynamics is:

$$\begin{aligned}
\frac{dP}{dt} &= -(\lambda_2 + \gamma_2)P + \gamma_1 A + \lambda_1 R, \\
\frac{dA}{dt} &= \gamma_2 P - (\ell_2 + \gamma_1)A + \ell_1 R, \\
\frac{dR}{dt} &= \lambda_2 P + \ell_2 A - (\lambda_1 + \ell_1)R,
\end{aligned} \tag{4.3.1}$$

considered with initial conditions $P(0) \geqslant 0$, $A(0) \geqslant 0$, $R(0) \geqslant 0$.

Analysis of this system looks at how the steady state of neurofilaments is distributed among the three states and how variations in switching rates influence dynamics. Key questions include: What is the steady-state distribution of neurofilaments across P, A, and R? How do changes in switching rates affect this distribution? This approach provides insights into the long-term organization of neurofilaments, complementing short-timescale transport studies.

4.4 The Transport-Exchange Models

Building on the insights from Section 4.3 and the sensitivity analysis presented in Figure 6.10 (b), we observe that the effects of exchange rates between anterograde (A) and retrograde (R) compartments, ℓ_1 and ℓ_2, are negligible under the conditions studied (see light colour in Figure 4.3). This is further supported by the experimental constraints of the pulse-spread experiment, which is limited to less than 20 minutes. Within this timeframe, the off-track pausing population, requiring a minimum of 60 minutes to return on-track [46, 57, 85], remains stationary and does not contribute to re-entry dynamics. Consequently, the return parameters γ_2 and λ_2 can be ignored, leading to two transport-exchange models that extend the pure transport model and refine the simplified model (4.1.2).

The first model, the transport-exchange model with irreversible pausing is for-

mulated as follows, as illustrated in Figure 4.3:

$$\begin{aligned}
\frac{\partial P}{\partial t} &= D\frac{\partial^2 P}{\partial x^2} + \gamma_1 A + \lambda_1 R, \quad P(x,0) = P_0 f(x), \\
\frac{\partial A}{\partial t} &= -v_a \frac{\partial A}{\partial x} - \gamma_1 A, \quad A(x,0) = A_0 f(x), \\
\frac{\partial R}{\partial t} &= v_r \frac{\partial R}{\partial x} - \lambda_1 R, \quad R(x,0) = R_0 f(x).
\end{aligned} \tag{4.4.1}$$

Here, γ_2 and λ_2 are negligible (depicted in light colour in Figure 4.3), indicating no return from the pausing state P to A or R.

Alternatively, we explore a second model, the transport-exchange model with reversible pausing, where diffusion (D) is negligible, and γ_2 and λ_2 are small but non-zero, acting as perturbative effects. This model, shown in Figure 4.3, incorporates these transition terms and is given by:

$$\begin{aligned}
\frac{\partial P}{\partial t} &= -(\lambda_2 + \gamma_2)P + \gamma_1 A + \lambda_1 R, \quad P(x,0) = P_0 f(x), \\
\frac{\partial A}{\partial t} &= -v_a \frac{\partial A}{\partial x} + \gamma_2 P - \gamma_1 A, \quad A(x,0) = A_0 f(x), \\
\frac{\partial R}{\partial t} &= v_r \frac{\partial R}{\partial x} + \lambda_2 P - \lambda_1 R, \quad R(x,0) = R_0 f(x).
\end{aligned} \tag{4.4.2}$$

In this case, γ_2 and λ_2 in Figure 4.3 represent minor returns from P to A and R, respectively. The parameter definitions, initial, and boundary conditions of the simplified model (4.1.2) apply to both models.

These models enable us to investigate whether incorporating transition terms enhances their ability to capture neurofilament dynamics compared to the pure transport approach, providing a foundation for evaluating their efficacy in representing experimental observations.

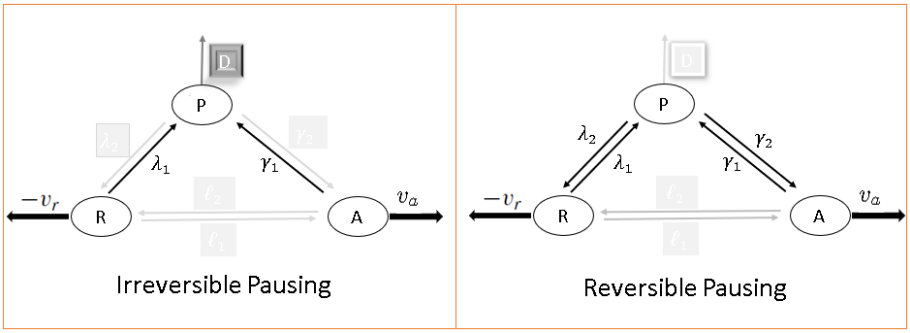

Figure 4.3: **Transport-exchange Models.** The diagram is derived from the simplified model (4.1.2) illustrating the flow between anterograde (A), retrograde (R), and pausing (P) states, advection and diffusion. In the irreversible pausing, the light colour transition (ℓ_1, ℓ_2, γ_2 and λ_2) are assumed to be negligible, indicating no return of pausing population to mobile states, resulting in (4.4.1). While in the reversible pausing, (ℓ_1, ℓ_2 and D) being negligible, which gives (4.4.2).

5

Mathematical Analysis

In this chapter, we present the analysis of the four models derived from the simplified model (4.1.2).

5.1 The Pure Transport Model

5.1.1 Solution

The pure transport model, as defined by (4.2.1), assumes no exchange between the anterograde (A), retrograde (R), and pausing (P) compartments over short timescales following photoactivation. The initial spatial distribution $f(x)$ (4.2.2) in this context, is modelled using a step function to represent the photoactivation profile. Utilizing the method of characteristics (detailed in Section 2.2.1) for the advective states and direct integration for the pausing state, we derive the following expressions for the spatial and temporal distribution of fluorescent neurofilaments post-photoactivation:

$$P(x,t) = P_0 \left(\frac{1}{1+\exp\left(-h(x-x_p)\right)} - \frac{1}{1+\exp\left(-h(x-x_d)\right)} \right),$$

$$A(x,t) = A_0 \left(\frac{1}{1+\exp\left(-h(x-v_a t - x_p)\right)} - \frac{1}{1+\exp\left(-h(x-v_a t - x_d)\right)} \right),$$
$$R(x,t) = R_0 \left(\frac{1}{1+\exp\left(-h(x+v_r t - x_p)\right)} - \frac{1}{1+\exp\left(-h(x+v_r t - x_d)\right)} \right). \quad (5.1.1)$$

Here, the unknowns to be estimated are the initial population partitions P_0, A_0, and R_0, as well as the velocities v_a and v_r. The parameters h, x_p, and x_d, which define the central photoactivation window (e.g., $x_p = 15\,\mu$m, $x_d = 30\,\mu$m, $h = -50$) as illustrated in Figure 5.1, are fixed based on the initial conditions and experimental setup. This formulation in (5.1.1) describes the spatial distribution of neurofilaments following activation, with the sigmoid terms reflecting the initial photoactivation profile constrained within the central window.

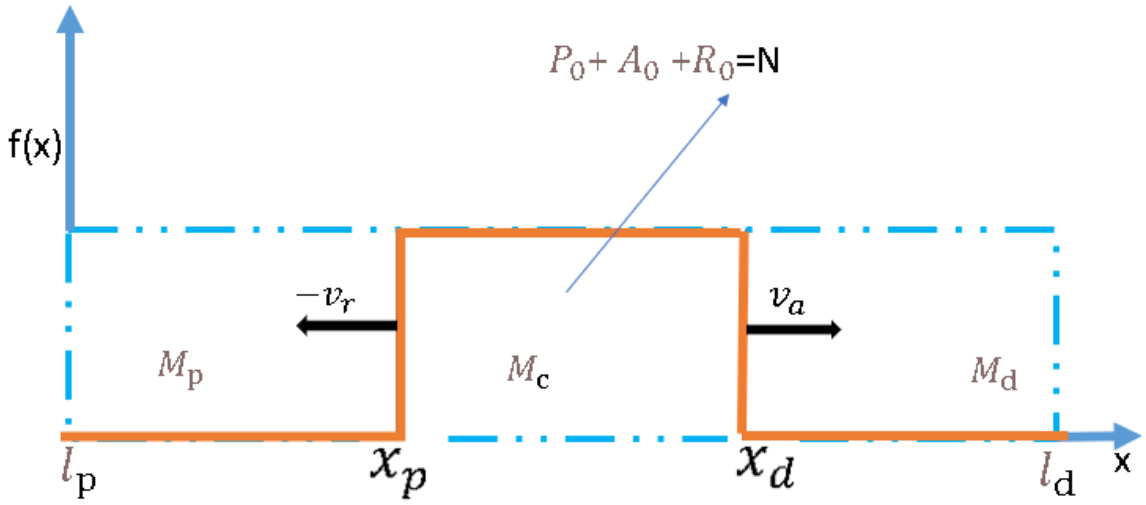

Figure 5.1: **Schematic of Pure Transport in Photoactivation.** The diagram illustrates the initial distribution of photoactivated neurofilaments across the axon, with the total population $P_0 + A_0 + R_0 = N$ confined to the central window (x_p to x_d, e.g., 15–30 μm). Neurofilaments move anterogradely (M_d) and retrogradely (M_p) into the distal (x_d to l_d, e.g., 30–45 μm) and proximal (l_p to x_p, e.g., 0–15 μm) windows, respectively, while M_c represents the remaining population in the central window. Arrows indicate the direction of transport.

To estimate the free parameters P_0, A_0, R_0, v_a, and v_r, we calibrate the model solutions (5.1.1) against experimental data (Average, normalise and photbleaching corrected) from Bomont's lab pulse-spread experiments, which capture neurofilaments

dynamics over time post-photoactivation. Since the data are limited to temporal measurements, we focus on a time-dependent observable by minimizing the error between predicted and observed distributions. This process involves initializing the model with fixed parameters h, x_p, and x_d from the photoactivation setup, then iteratively adjusting the parameters using a GA optimization technique to best match the data. As illustrated in Figure 5.1, post-photoactivation, neurofilaments disperse into the proximal and distal windows due to retrograde and anterograde transport, respectively. To quantify this dispersion over time, we integrate (5.1.1) over the respective spatial domains, defining $M_c(t)$, $M_p(t)$, and $M_d(t)$ as the photoactivated neurofilaments quantities in the central, proximal, and distal windows at time t, respectively (5.1.2). This calibration, detailed in subsequent sections, ensures that the model accurately captures the temporal dynamics observed in the experiment. At the time of photoactivation, all neurofilaments—represented by $P(x,t)$, $A(x,t)$, and $R(x,t)$—are initially confined to the central window (x_p to x_d) and contribute to the photoactivated neurofilaments amount within the central window. As time progresses, photoactivated neurofilaments in the anterograde state $A(x,t)$ and retrograde state $R(x,t)$ redistribute and contribute to the fluorescence amount in the distal and proximal windows, respectively. Thus,

$$\begin{aligned} M_c(t) &= \int_{x_p}^{x_d} [P(x,t) + A(x,t) + R(x,t)]\, dx, \\ M_d(t) &= \int_{x_d}^{l_d} A(x,t)\, dx, \\ M_p(t) &= \int_{l_p}^{x_p} R(x,t)\, dx. \end{aligned} \tag{5.1.2}$$

These integrals, which involve complicated functions, lack explicit analytical solutions, necessitating numerical methods. We employed the ‘integrate‘ function in R [89], which efficiently computes definite integrals over specified ranges.

This approach enable as to calculate the amount of neurofilaments in each window at a given time, and then fitting (5.1.2) to the experimental data ensures the estimation of model parameters.

5.1.2 Data Fitting

To estimate the free parameters v_a, v_r, P_0, A_0, and R_0 of the model(4.2.1), we fit (5.1.2) to our normalised and photobleaching-corrected experimental data as follows.

1. Objective Function

To establish a rigorous comparison between our model and experimental data, we designed an objective (fitness) function that quantifies the fit quality. The model quantifies the amount of activated neurofilaments in each window across time, as described in (5.1.2). To ensure good fit between the model and experimental data, we define an error term based on fluorescence values obtained after photobleach correction.

The objective function is the sum of squared errors (SSE) between the corrected experimental data and model outputs. Specifically, if the experimental data at time t_i is denoted as $F(t_i) = (F_d(t_i), F_p(t_i), F_c(t_i))$ and the corresponding model output is $M(t_i) = (M_d(t_i), M_p(t_i), M_c(t_i))$ (e.g., as defined as in (5.1.2)), the error function can be defined as:

$$\begin{aligned}
\text{Error} &= \sum_{i=1}^{n} \|F(t_i) - M(t_i)\|^2 \\
&= \sum_{i=1}^{n} \sum_{j\in\{d,p,c\}} (F_j(t_i) - M_j(t_i))^2 \\
&= \sum_{i=1}^{n} \left[(F_d(t_i) - M_d(t_i))^2 + (F_p(t_i) - M_p(t_i))^2 + (F_c(t_i) - M_c(t_i))^2\right] \quad (5.1.3)
\end{aligned}$$

Minimizing this error optimizes the parameters, enhancing the model's ability to capture the temporal dynamics of neurofilaments distribution across windows.

2. Genetic Algorithm Optimization

We used a GA, as described in Section 2.3.1, to optimize the model parameters. The GA iteratively generates new candidate solutions through crossover and mutation, evolving the population toward an optimal parameter set that minimizes the SSE (5.1.3). This method effectively navigates complex, multidimensional parameter spaces, avoiding local minima and ensuring a robust fit to the experimental data.

5.2 The Pure Exchange Model

We analyse the pure exchange model (4.3.1), which focuses on state transitions between pausing (P), anterograde (A), and retrograde (R) neurofilaments populations, neglecting transport terms:

$$\begin{aligned}\frac{dP}{dt} &= -(\lambda_2 + \gamma_2)P + \gamma_1 A + \lambda_1 R,\\ \frac{dA}{dt} &= \gamma_2 P - (\ell_2 + \gamma_1)A + \ell_1 R,\\ \frac{dR}{dt} &= \lambda_2 P + \ell_2 A - (\lambda_1 + \ell_1)R,\end{aligned}$$

with non-negative initial conditions $P(0) \geqslant 0$, $A(0) \geqslant 0$, and $R(0) \geqslant 0$.

5.2.1 Conservation and System Reduction

The total population of neurofilaments remains constant over time ($t \geqslant 0$):

$$\frac{dP}{dt} + \frac{dA}{dt} + \frac{dR}{dt} = 0. \tag{5.2.1}$$

Integrating with respect to time yields:

$$P(t) + A(t) + R(t) = K, \quad t \geqslant 0, \tag{5.2.2}$$

where K is the total initial neurofilaments population. Substituting $R(t) = K - A(t) - P(t)$ into (4.3.1), the system reduces to:

$$\begin{aligned} \frac{dP}{dt} &= -(\lambda_2 + \gamma_2 + \lambda_1)P + (\gamma_1 - \lambda_1)A + \lambda_1 K, \\ \frac{dA}{dt} &= (\gamma_2 - \ell_1)P - (\ell_1 + \ell_2 + \gamma_1)A + \ell_1 K. \end{aligned} \tag{5.2.3}$$

5.2.2 Non-Dimensionalization

To simplify analysis, we non-dimensionalize the system using a change of variables:

$$\tau = \frac{t}{T_o}, \quad p(\tau) = \frac{P(t)}{K}, \quad a(\tau) = \frac{A(t)}{K}, \tag{5.2.4}$$

where $T_o = \frac{1}{\lambda_2+\gamma_2+\lambda_1}$, and τ, p, and a are dimensionless variables. Substituting into (5.2.3), the system becomes:

$$\begin{aligned} \frac{dp}{d\tau} &= -p + \eta a + b, \\ \frac{da}{d\tau} &= \xi p - \mu a + d, \end{aligned} \tag{5.2.5}$$

where the dimensionless parameters are:

$$b = \frac{\lambda_1}{\lambda_2 + \gamma_2 + \lambda_1}, \quad d = \frac{\ell_1}{\lambda_2 + \gamma_2 + \lambda_1}, \quad \eta = \frac{\gamma_1 - \lambda_1}{\lambda_2 + \gamma_2 + \lambda_1}, \quad \xi = \frac{\gamma_2 - \ell_1}{\lambda_2 + \gamma_2 + \lambda_1},$$

$$\mu = \frac{\ell_1 + \ell_2 + \gamma_1}{\lambda_2 + \gamma_2 + \lambda_1}.$$

This linear system can be written in matrix form as:

$$\begin{bmatrix} p \\ a \end{bmatrix}' = \begin{bmatrix} -1 & \eta \\ \xi & -\mu \end{bmatrix} \begin{bmatrix} p \\ a \end{bmatrix} + \begin{bmatrix} b \\ d \end{bmatrix}, \tag{5.2.6}$$

where the coefficient matrix is:

$$B = \begin{bmatrix} -1 & \eta \\ \xi & -\mu \end{bmatrix}. \tag{5.2.7}$$

The system is linear, autonomous (with constant coefficients), and non-homogeneous, ensuring a unique solution for any initial condition $p(\tau_0) = p_0$, $a(\tau_0) = a_0$, where $p_0, a_0 \in [0, 1]$, due to the continuity of the system and its derivatives.

5.2.3 Equilibrium, Reactivity, and Resilience

We assess the system's dynamics by examining its equilibrium, resilience (rate of return to equilibrium following a perturbation), and reactivity (potential for perturbation amplification). Understanding these properties is critical to evaluate the model's ability to maintain a stable distribution of neurofilaments states under biological variations, such as changes in switching rates, which are influenced by cellular conditions.

1. Equilibrium and Stability

Theorem 5.2.1. *The system* (5.2.6) *has a unique equilibrium* $\pi^* = (p^*, a^*) = \left(\frac{\mu b+\eta d}{\mu-\xi\eta}, \frac{\xi b+d}{\mu-\xi\eta}\right)$, *which is (globally) asymptotically stable.*

Proof. The equilibrium is found by setting $\frac{dp}{d\tau} = 0$ and $\frac{da}{d\tau} = 0$:

$$\begin{bmatrix} -1 & \eta \\ \xi & -\mu \end{bmatrix} \begin{bmatrix} p \\ a \end{bmatrix} + \begin{bmatrix} b \\ d \end{bmatrix} = \mathbf{0}. \tag{5.2.8}$$

The determinant of the coefficient matrix in (5.2.8) is:

$$\mu - \xi\eta = \frac{\lambda_1(\ell_2 + \gamma_1 + \gamma_2) + \lambda_2(\ell_1 + \ell_2 + \gamma_1) + \gamma_2(\ell_1 + \ell_2) + \ell_1\gamma_1}{(\lambda_1 + \lambda_2 + \gamma_2)^2}.$$

Since all transition rates $(\lambda_1, \lambda_2, \gamma_1, \gamma_2, \ell_1, \ell_2)$ are positive, the denominator and numerator are positive and $\det(B) = \mu - \xi\eta > 0$. Hence, there exists a unique equilibrium $\pi^* = (p^*, a^*)$:

$$\begin{bmatrix} p^* \\ a^* \end{bmatrix} = \begin{bmatrix} 1 & -\eta \\ -\xi & \mu \end{bmatrix}^{-1} \begin{bmatrix} b \\ d \end{bmatrix}.$$

$$\begin{aligned} (p^*, a^*) &= \left(\frac{\mu b + \eta d}{\mu - \xi\eta}, \frac{\xi b + d}{\mu - \xi\eta} \right) \\ &= \left(\frac{(\ell_2 + \gamma_1)\lambda_1 + \gamma_1\ell_1}{\lambda_1(\ell_2 + \gamma_1 + \gamma_2) + \lambda_2(\ell_1 + \ell_2 + \gamma_1) + \gamma_2(\ell_1 + \ell_2) + \ell_1\gamma_1}, \right. \\ &\qquad \left. \frac{\gamma_2\lambda_1 + (\ \lambda_2 + \gamma_2)\ell_1}{\lambda_1(\ell_2 + \gamma_1 + \gamma_2) + \lambda_2(\ell_1 + \ell_2 + \gamma_1) + \gamma_2(\ell_1 + \ell_2) + \ell_1\gamma_1} \right). \end{aligned} \tag{5.2.9}$$

This equilibrium is non-negative and $\pi^* \in [0, 1] \times [0, 1]$.

To assess the stability of the equilibrium point defined by (5.2.9), we analyse the sign of roots of the characteristic polynomial of B (5.2.7), given by:

$$\lambda^2 + (1 + \mu)\lambda + (\mu - \xi\eta) = 0.$$

Using the Routh-Hurwitz criterion (see Section 2.1). Given that $\mu > 0$, we have

$1 + \mu > 0$ and as established above $\mu - \xi\eta > 0$. With both coefficients positive, the Routh-Hurwitz criterion states that all eigenvalues of the characteristic equation have negative real parts. For a linear system with a unique equilibrium, this result guarantees (global) asymptotic stability of the equilibrium (5.2.9) (see Section 2.1.1).

□

The steady-state adimensionalized distribution of neurofilaments is $(p^*, a^*, r^* = 1 - p^* - a^*)$:

$$\begin{aligned} p^* &= \frac{(\ell_2 + \gamma_1)\lambda_1 + \gamma_1\ell_1}{(\lambda_1 + \lambda_2 + \gamma_2)(\ell_1 + \ell_2 + \gamma_1) - (\gamma_2 - \ell_1)(\gamma_1 - \lambda_1)}, \\ a^* &= \frac{\gamma_2\lambda_1 + (\ \lambda_2 + \gamma_2)\ell_1}{(\lambda_1 + \lambda_2 + \gamma_2)(\ell_1 + \ell_2 + \gamma_1) - (\gamma_2 - \ell_1)(\gamma_1 - \lambda_1)}, \\ r^* &= \frac{(\ell_2 + \gamma_1)\lambda_2 + \ell_2\gamma_2}{(\lambda_1 + \lambda_2 + \gamma_2)(\ell_1 + \ell_2 + \gamma_1) - (\gamma_2 - \ell_1)(\gamma_1 - \lambda_1)}. \end{aligned} \tag{5.2.10}$$

Research data from the axons of newborn mice and rats, as analysed by Li *et al.*[2] based on studies by Alami et al. [90] and Trivedi *et al.* [46], indicate that approximately 60-80% of neurofilaments are in a pausing state, reflecting a significant off-track population. This observation is further supported by Li *et al.*[46], that neurofilaments spend approximately 92% of their time pausing. This suggests that the extent of pausing is a key factor influencing their overall transport efficiency and distribution along axons. To model this biological phenomenon, we assume a steady-state dominant pausing population, where the pausing proportion p^* exceeds the combined proportions of the anterograde a^* and retrograde r^* states. This assumption is imposed to align the mathematical model with empirical evidence. This implies that for a higher pausing population ($p^* > a^* + r^*$) to exist, the steady-state from (5.2.10) yields $\frac{(\lambda_1-\lambda_2)(\ell_2+\gamma_1)+(\gamma_1-\gamma_2)\ell_1}{(\lambda_1+\ell_2)\gamma_2+\lambda_2\ell_1} > 1$, which imposes the following constraints on the system parameters:

1. High transition rates into pausing ($\gamma_1, \lambda_1 \gg \gamma_2, \lambda_2$), reflecting biological preva-

lence of pausing in neurofilaments.

2. Balanced anterograde-retrograde switching (ℓ_1, ℓ_2 not dominant), ensuring prolonged pausing.

2. Resilience

Resilience is the rate at which the system returns to stable equilibrium after a perturbation [91], is determined by the eigenvalue of B (5.2.7) with the largest (maximum) real part (see Section 2.1.3). The eigenvalues of B are:

$$\lambda_{1,2}^B = \frac{-(1+\mu) \pm \sqrt{(1+\mu)^2 - 4(\mu - \xi\eta)}}{2}.$$

Since $\mu - \xi\eta > 0$, the discriminant $(1+\mu)^2 - 4(\mu - \xi\eta) < (1+\mu)^2$, and the eigenvalues are real and negative (as proven in Theorem 5.2.3). The eigenvalue with the largest real part is:

$$\lambda_L^B = \frac{-(1+\mu) + \sqrt{(1+\mu)^2 - 4(\mu - \xi\eta)}}{2}.$$

Resilience is defined as $R(\pi^*) = -\mathrm{Re}(\lambda_L^B) = -\lambda_L^B$:

$$R(\pi^*) = \frac{(1+\mu) - \sqrt{(1+\mu)^2 - 4(\mu - \xi\eta)}}{2}.$$

Substituting the dimensionless parameters:

$$R(\pi^*) = \frac{(\lambda_1 + \lambda_2 + \ell_1 + \ell_2 + \gamma_1 + \gamma_2) - \sqrt{\begin{array}{l}(\lambda_1 + \lambda_2 + \ell_1 + \ell_2 + \gamma_1 + \gamma_2)^2 \\ \quad - 4\Big[(\ell_1 + \ell_2 + \gamma_1)(\lambda_1 + \lambda_2 + \gamma_2) \\ \qquad - (\gamma_2 - \ell_1)(\gamma_1 - \lambda_1)\Big]\end{array}}}{2(\lambda_1 + \lambda_2 + \gamma_2)}.$$

This represents the neurofilaments system's ability to rapidly restore its equilibrium through antagonistic processes: anterograde vs. retrograde switching rate, and

off-track pausing vs. on-track rate processes. The higher the value, the shorter the equilibrium restoration time.

The average return time to equilibrium is given by $\frac{-1}{\lambda_L^B}$, which decreases with higher resilience, reflecting faster recovery from perturbations such as cellular stress or molecular changes in neurofilaments dynamics.

3. Reactivity

Reactivity measures the initial amplification rate of perturbations [72]. A system is non-reactive if perturbations decay monotonically (see Chapter 2.1). Then matirx $H(B)$ is:

$$H(B) = \begin{bmatrix} -1 & (\eta+\xi)/2 \\ (\eta+\xi)/2 & -\mu \end{bmatrix},$$

with eigenvalues:

$$\lambda_{1,2}^{H(B)} = \frac{-(1+\mu) \pm \sqrt{(1+\mu)^2 - (4\mu - (\eta+\xi)^2)}}{2}.$$

Reactivity is $\Re(B) = \lambda_L^{H(B)}$, where:

$$\lambda_L^{H(B)} = \frac{-(1+\mu) + \sqrt{(1+\mu)^2 - (4\mu - (\eta+\xi)^2)}}{2}.$$

The system is reactive if $\lambda_L^{H(B)} > 0$, i.e.:

$$\sqrt{(1+\mu)^2 - (4\mu - (\eta+\xi)^2)} > 1+\mu \quad \Rightarrow \quad 4\mu < (\eta+\xi)^2.$$

Substituting μ, η, and ξ:

$$4(\ell_1+\ell_2+\gamma_1)(\lambda_1+\lambda_2+\gamma_2) < (\gamma_2-\ell_1+\gamma_1-\lambda_1)^2.$$

We let,

$$\begin{aligned}\Delta &= 4(\ell_1 + \ell_2 + \gamma_1)(\lambda_1 + \lambda_2 + \gamma_2) - (\gamma_1 + \gamma_2 - \ell_1 - \lambda_1)^2, \\ &= 2\gamma_1\gamma_2 + 4\gamma_1\lambda_2 + 4\ell_1\lambda_2 + 4\ell_2\lambda_1 + 4\ell_2\lambda_2 + 4\ell_2\gamma_2 + 2\ell_1\lambda_1 \\ &\quad + 2\gamma_1\ell_1 + 2\gamma_2\ell_1 + 2\gamma_2\lambda_1 - \gamma_1^2 - \gamma_2^2 - \ell_1^2 - \lambda_1^2;\end{aligned}$$

hence,

- if $\Delta > 0$, the inequality is **false** and the system is generally non-reactive,
- if $\Delta < 0$, the inequality is **true** and the system is generally reactive.

Given that the positive terms are typically large due to the factor of 4 or 2, while the negative terms are squared and may be small under typical biological conditions, this inequality is unlikely to hold. Thus, the system is most likely to be non-reactive, with perturbations decaying monotonically.

The lack of reactivity indicates that the system is self-regulating and resistant to disruption, protecting axonal integrity and preventing harmful buildup of neurofilaments. Moreover, the monotonic decay of perturbations means that any temporary imbalances are quickly corrected through the coordinated action of anterograde, retrograde and pausing exchange rates.

5.3 The Transport-Exchange Model

5.3.1 Solution of Irreversible Pausing Model

Just like in the pure transport model, we also need to solve and restructure the model (4.4.1) in order to fit it to our data. In that regard, to solve (4.4.1), we assume that diffusion in pulse-spread is negligible, $D = 0$, and apply the method of characteristics from Section 2.2.1 to the equations governing A and R, which are first-order linear

PDEs. We obtain solutions for $A(x,t)$ and $R(x,t)$, and then plug these solutions into $P(x,t)$ and integrate the results. The resulting solutions are

$$\begin{aligned} A(x,t) &= A_0 f(x - v_a t) e^{-\gamma_1 t}, \\ R(x,t) &= R_0 f(x + v_r t) e^{-\lambda_1 t}, \\ P(x,t) &= P(x,0) + \int_0^t \left(\gamma_1 A(x,\tau) + \lambda_1 R(x,\tau)\right) d\tau, \end{aligned} \tag{5.3.1}$$

where $f(x) = \left(\frac{1}{1+\exp(-h(x-x_p))} - \frac{1}{1+\exp(-h(x-x_d))}\right)$.

These solutions describe the spatiotemporal evolution of the neurofilament populations. To facilitate the model fitting to our data, we adapt (5.3.1) by integrating the solutions over a spatial window, as expressed in (5.1.2), reducing it to the dependency on time alone. This temporal formulation allows us to estimate the unknown parameters (v_a, v_r, γ_1, λ_1, P_0, R_0, and A_0) through GA model fitting, utilizing the error minimization approach outlined in (5.1.3).

5.3.2 Steady State of Irreversible Pausing Model

Having looked at the short-time dynamics of the model (4.4.1), by fitting it to pulse-spread data, we will also want to study its steady state behaviour. At equilibrium, the time derivatives vanish. Therefore, we set $\frac{\partial P}{\partial t} = 0$, $\frac{\partial A}{\partial t} = 0$, and $\frac{\partial R}{\partial t} = 0$. Substituting into (4.4.1), we obtain:

$$0 = D\frac{\partial^2 P}{\partial x^2} + \gamma_1 A_\infty(x) + \lambda_1 R_\infty(x), \tag{5.3.2}$$

$$0 = -v_a \frac{dA_\infty}{dx} - \gamma_1 A_\infty, \tag{5.3.3}$$

$$0 = v_r \frac{dR_\infty}{dx} - \lambda_1 R_\infty, \tag{5.3.4}$$

where $A_\infty(x)$, $R_\infty(x)$, and $P_\infty(x)$ represent the steady-state populations.

Solving (5.3.3) and (5.3.4), we get:

$$\frac{dA_\infty}{dx} = -\frac{\gamma_1}{v_a}A_\infty \quad \Rightarrow \quad A_\infty(x) = C_1 e^{-\frac{\gamma_1}{v_a}x}, \tag{5.3.5}$$

$$\frac{dR_\infty}{dx} = \frac{\lambda_1}{v_r}R_\infty \quad \Rightarrow \quad R_\infty(x) = C_2 e^{\frac{\lambda_1}{v_r}x}. \tag{5.3.6}$$

Recall the boundary conditions

$$\left.\frac{dA_\infty}{dx}\right|_{x=0,L} = 0, \quad \left.\frac{dR_\infty}{dx}\right|_{x=0,L} = 0$$

and apply to $A_\infty(x) = C_1 e^{-\frac{\gamma_1}{v_a}x}$:

$$\left.\frac{dA_\infty}{dx}\right|_{x=o} = C_1 = 0 \quad \Rightarrow \quad A_\infty(x) \equiv 0.$$

Similarly, $\left.\frac{dR_\infty}{dx}\right|_{x=0} = C_2 = 0 \Rightarrow R_\infty(x) \equiv 0.$

Plug $A_\infty = R_\infty = 0$ into (5.3.2)

$$0 = D\frac{d^2_\infty P}{dx^2} + \gamma_1 A_\infty + \lambda_1 R_\infty = D\frac{d^2 P_\infty}{dx^2} \Rightarrow \frac{d^2 P_\infty}{dx^2} = 0.$$

So, the general solution is:

$$P_\infty(x) = mx + c.$$

Apply our boundary conditions:

$$\left.\frac{dP_\infty}{dx}\right|_{x=0} = m = 0, \quad \left.\frac{dP_\infty}{dx}\right|_{x=L} = m = 0,$$

$$\Rightarrow m = 0 \Rightarrow P_\infty(x) = c = \text{constant}.$$

Hence, $A_\infty(x) = 0$, $R_\infty(x) = 0$ and $P_\infty(x) = N$.

Under these assumptions, the steady-state solution reveals that the anterograde (A) and retrograde (R) populations diminish to zero, while the pausing population (P) reaches a value equal to the initial total neurofilaments amount per unit length N across the domain, reflecting a complete halt of active transport in the axon.

5.3.3 Steady State of Reversible Pausing Model

On the other hand, assuming the case where only diffusion is negligible while γ_2 and λ_2 are small but non-zero, instead of completely negligible, means that they act as perturbative effects (see Figure 4.3). Therefore, the equations of the system describing the equilibrium state of (4.4.2) are

$$\begin{aligned} 0 &= -(\lambda_2 + \gamma_2)P_\infty + \gamma_1 A_\infty + \lambda_1 R_\infty, \\ 0 &= -v_a \frac{dA_\infty}{\partial x} + \gamma_2 P_\infty - \gamma_1 A_\infty, \\ 0 &= v_r \frac{dR_\infty}{\partial x} + \lambda_2 P_\infty - \lambda_1 R_\infty. \end{aligned} \tag{5.3.7}$$

Here, P_∞, A_∞, and R_∞ are functions of x, and all parameters $(\lambda_1, \lambda_2, \gamma_1, \gamma_2, v_a, v_r)$ are constants. The first-order spatial derivatives $\frac{dA_\infty}{\partial x}$ and $\frac{dR_\infty}{\partial x}$ represent the spatial rates of change of the anterograde and retrograde populations along the axon, respectively (5.3.7). Since there are no diffusion terms, the steady-state system reduces to a boundary value problem with first-order spatial dependence. Hence, we solve it as follows:

$$(\lambda_2 + \gamma_2)P_\infty = \lambda_1 R_\infty + \gamma_1 A_\infty, \tag{5.3.8}$$

$$v_a \frac{dA_\infty}{dx} = \gamma_2 P_\infty - \gamma_1 A_\infty, \tag{5.3.9}$$

$$v_r \frac{dR_\infty}{dx} = \lambda_1 R_\infty - \lambda_2 P_\infty. \tag{5.3.10}$$

From (5.3.8), we can express P_∞ in terms of A_∞ and R_∞:

$$P_\infty(x) = \frac{\lambda_1 R_\infty(x) + \gamma_1 A_\infty(x)}{\lambda_2 + \gamma_2}.$$

Substitute P_∞ into (5.3.9) and (5.3.10) to eliminate P_∞ gives two coupled first-order linear ODEs:

$$\begin{aligned} v_a(\lambda_2 + \gamma_2)\frac{dA_\infty}{dx} &= \gamma_2\lambda_1 R_\infty - \gamma_1\lambda_2 A_\infty \\ v_r(\lambda_2 + \gamma_2)\frac{dR_\infty}{dx} &= \lambda_1\gamma_2 R_\infty - \lambda_2\gamma_1 A_\infty. \end{aligned}$$

This can be written in matrix form as:

$$\frac{d}{dx}\begin{pmatrix} A_\infty \\ R_\infty \end{pmatrix} = \frac{1}{(\lambda_2 + \gamma_2)}\begin{pmatrix} \frac{-\gamma_1\lambda_2}{v_a} & \frac{\gamma_2\lambda_1}{v_a} \\ \frac{-\lambda_2\gamma_1}{v_r} & \frac{\lambda_1\gamma_2}{v_r} \end{pmatrix}\begin{pmatrix} A_\infty \\ R_\infty \end{pmatrix}, \tag{5.3.11}$$

with the coefficient matrix M:

$$M = \frac{1}{(\lambda_2 + \gamma_2)}\begin{pmatrix} \frac{-\gamma_1\lambda_2}{v_a} & \frac{\gamma_2\lambda_1}{v_a} \\ \frac{-\lambda_2\gamma_1}{v_r} & \frac{\lambda_1\gamma_2}{v_r} \end{pmatrix}.$$

To solve (5.3.11), we need the eigenvalues and eigenvectors of M. The characteristic equation of M is:

$$\det[M - \mu I] = 0,$$

with

$$\det[M-\mu I] = \left(\frac{-\gamma_1\lambda_2}{v_a(\lambda_2 + \gamma_2)} - \mu\right)\left(\frac{\lambda_1\gamma_2}{v_r(\lambda_2 + \gamma_2)} - \mu\right) - \left(\frac{\gamma_2\lambda_1}{v_a(\lambda_2 + \gamma_2)}\right)\left(\frac{-\lambda_2\gamma_1}{v_r(\lambda_2 + \gamma_2)}\right).$$

The eigenvalues of M are

$$\mu_1 = 0, \quad \mu_2 = \frac{\lambda_1\gamma_2 v_a - \gamma_1\lambda_2 v_r}{v_a v_r(\lambda_2 + \gamma_2)},$$

with the corresponding eigenvectors $\begin{pmatrix} 1 \\ \frac{\gamma_1\lambda_2}{\gamma_2\lambda_1} \end{pmatrix}$ and $\begin{pmatrix} 1 \\ \frac{v_a}{v_r} \end{pmatrix}$ (see details in Appendix A). Hence, assuming $\frac{\gamma_1\lambda_2}{\gamma_2\lambda_1} \neq \frac{v_a}{v_r}$, the general solution of (5.3.11) (see Section 2.1.1) is:

$$\begin{pmatrix} A_\infty(x) \\ R_\infty(x) \end{pmatrix} = c_1 \begin{pmatrix} 1 \\ \frac{\gamma_1\lambda_2}{\gamma_2\lambda_1} \end{pmatrix} e^{\mu_1 x} + c_2 \begin{pmatrix} 1 \\ \frac{v_a}{v_r} \end{pmatrix} e^{\mu_2 x}.$$

Substituting $A_\infty(x)$ and $R_\infty(x)$ into $P_\infty(x)$, the general steady-state solution is

$$\begin{aligned} A_\infty(x) &= c_1 + c_2 e^{\mu_2 x}, \\ R_\infty(x) &= c_1 \frac{\gamma_1\lambda_2}{\gamma_2\lambda_1} + c_2 \frac{v_a}{v_r} e^{\mu_2 x}, \\ P_\infty(x) &= \frac{c_1\gamma_1 \left(\frac{\lambda_2}{\gamma_2} + 1\right) + c_2 \left(\lambda_1 \frac{v_a}{v_r} + \gamma_1\right) e^{\mu_2 x}}{\lambda_2 + \gamma_2}, \end{aligned} \tag{5.3.12}$$

where c_1 and c_2 are constants determined by boundary conditions:

$$\left.\frac{dA_\infty}{dx}\right|_{x=0,L} = 0, \quad \left.\frac{dR_\infty}{dx}\right|_{x=0,L} = 0.$$

This gives $c_2 = 0$ and (5.3.12) becomes (see details in Appendix A)

$$A_\infty(x) = c_1,$$

$$R_\infty(x) = c_1 \frac{\gamma_1\lambda_2}{\gamma_2\lambda_1},$$

$$P_\infty(x) = \frac{c_1\gamma_1 \left(\frac{\lambda_2}{\gamma_2} + 1\right)}{\lambda_2 + \gamma_2}.$$

Since the total neurofilaments population is conserved over time, the sum of the steady-state proportions $\int_0^L P_\infty(x) + A_\infty(x) + R_\infty(x)dx$ must equal the total initial

population $(x_d - x_p)N$. Substituting the expressions, we get

$$\frac{c_1\gamma_1\left(\frac{\lambda_2}{\gamma_2}+1\right)}{\lambda_2+\gamma_2} + c_1 + c_1\frac{\gamma_1\lambda_2}{\gamma_2\lambda_1} = \frac{(x_d-x_p)}{L}N,$$

and solving for c_1, $c_1 = \frac{(x_d-x_p)N\gamma_2\lambda_1}{[\gamma_1(\lambda_1+\lambda_2)+\gamma_2\lambda_1]L}$.

Hence, the steady state repartition of neurofilaments in axons assuming a reversible pausing is

$$A_\infty(x) = \frac{(x_d-x_p)N\gamma_2\lambda_1}{[\gamma_1(\lambda_1+\lambda_2)+\gamma_2\lambda_1]L},$$

$$R_\infty(x) = \frac{(x_d-x_p)N\gamma_1\lambda_2}{[\gamma_1(\lambda_1+\lambda_2)+\gamma_2\lambda_1]L},$$

$$P_\infty(x) = \frac{(x_d-x_p)N\gamma_1\lambda_1}{[\gamma_1(\lambda_1+\lambda_2)+\gamma_2\lambda_1]L},$$

under the condition $\frac{\gamma_1\lambda_2}{\gamma_2\lambda_1} \neq \frac{v_a}{v_r}$.

These steady-state solutions are constant across the axon (independent of x), indicating the anterograde (A), retrograde (R), and pausing (P) states maintain a fixed proportion along the axon. Their independence from velocities v_a and v_r shows that, over time, the equilibrium depends only on exchange rates (γ_1, γ_2, λ_1, λ_2), with transport effects become negligible, aligning with the pure exchange model's assumption that the impact of transport fades out in the long run.

The reversible pausing model's steady state differs from the irreversible model, where $A_\infty = 0$, $R_\infty = 0$, and $P_\infty = N$, showing all neurofilaments eventually pause. The reversible model allows non-zero A_∞ and R_∞, creating a balance of mobile and pausing states with exchange dominating if $\frac{\gamma_1\lambda_2}{\gamma_2\lambda_1} \neq \frac{v_a}{v_r}$, while irreversibility leads to all pausing.

6

Numerical Work

In this section, we show the numerical results for the pure transport model, the pure exchange model and the transport-exchange model. The data used is the normalised, photobleaching corrected and averaged fluorescence data after photoactivation as explained in Section 3.2. All numerical work was done in *R*.

6.1 Results of the Pure Transport Model

6.1.1 Effect of Age on Neurofilament Transport

As indicated by our data analysis in Section 3.2, neurofilaments transport, among others, is anterograde bias and reverses with age. To further extend our investigation to gain insights about retrograde and anterograde speeds and proportions of mobile and immobile states, we then performed more parameter estimation by calibrating our pure transport model (4.2.1), using a GA optimization as detailed in Section 2.3.1. Given the stochastic nature of GA, we conducted 300 independent runs optimizing (5.1.3) for each experimental condition (72 hpf, 96 hpf, and 120 hpf) to ensure robustness. For each run, model outputs were computed using (5.1.2) and fitted to experimental data up to 5, 8 and 10 minutes. This multi-run approach allowed us

to assess the consistency of the parameters (v_a, v_r, P_0, A_0, and R_0) estimates and the quality of the fit across the proximal, central, and distal windows.

Figure 6.1 presents the results of the multi-run fitting process up to 5 minutes. The green dots represent the normalised-corrected fluorescence data obtained from the pulse-spread experiment for the proximal, central, and distal windows at 72 hpf (first row), 96 hpf (second row), and 120 hpf (third row). The coloured lines show the model output for $M_c(t)$, $M_d(t)$, and $M_p(t)$ from (5.1.2) over time, with each line corresponding to one of the 300 GA runs. The error scale on the right indicates the range of fitting errors, with darker colours (lower errors) corresponding to better fits.

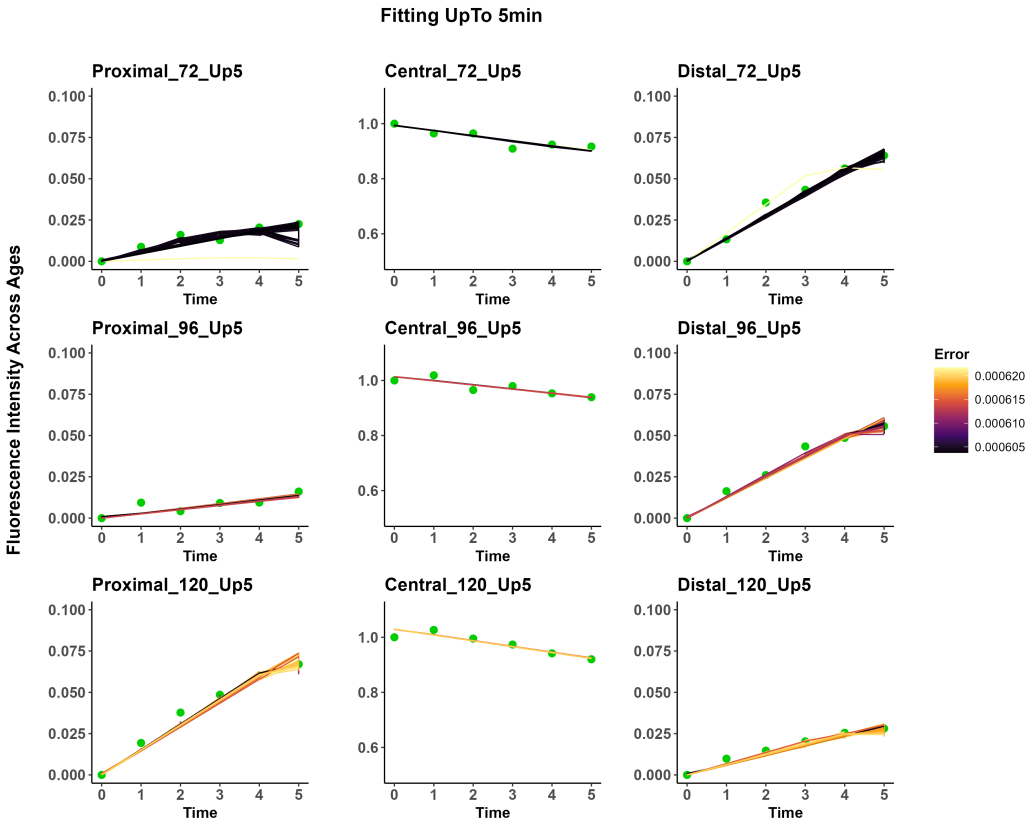

Figure 6.1: **Fitting of the pure transport** (5.1.2) **model to experimental data for 72, 96, and 120 hpf up to 5 minutes.** The first row is 72 hpf, the second row is 96 hpf and the third row is 120 hpf. While the first column is proximal, the second column is central and the third column is distal windows. Green points represent experimental data, while coloured lines show the model responses with the colour gradient indicating error levels (darker shades denote lower errors).

To explore the model beyond the linear regime, we extended the fitting to 8 and 10 minutes, because the data is conserved up to 10 minutes (Figure 6.14). Presented in Figure 6.2, the left panel shows fittings of up to 8 minutes, and the right panel extends to 10 minutes. The model continues to closely match the experimental data as the time frame increases from 5 to 10 minutes, demonstrating its accuracy of fit over a broader temporal range and beyond the linear regime. This progressive extension, detailed in the next section through parameter analysis, confirms the model's robustness in capturing the underlying biological dynamics.

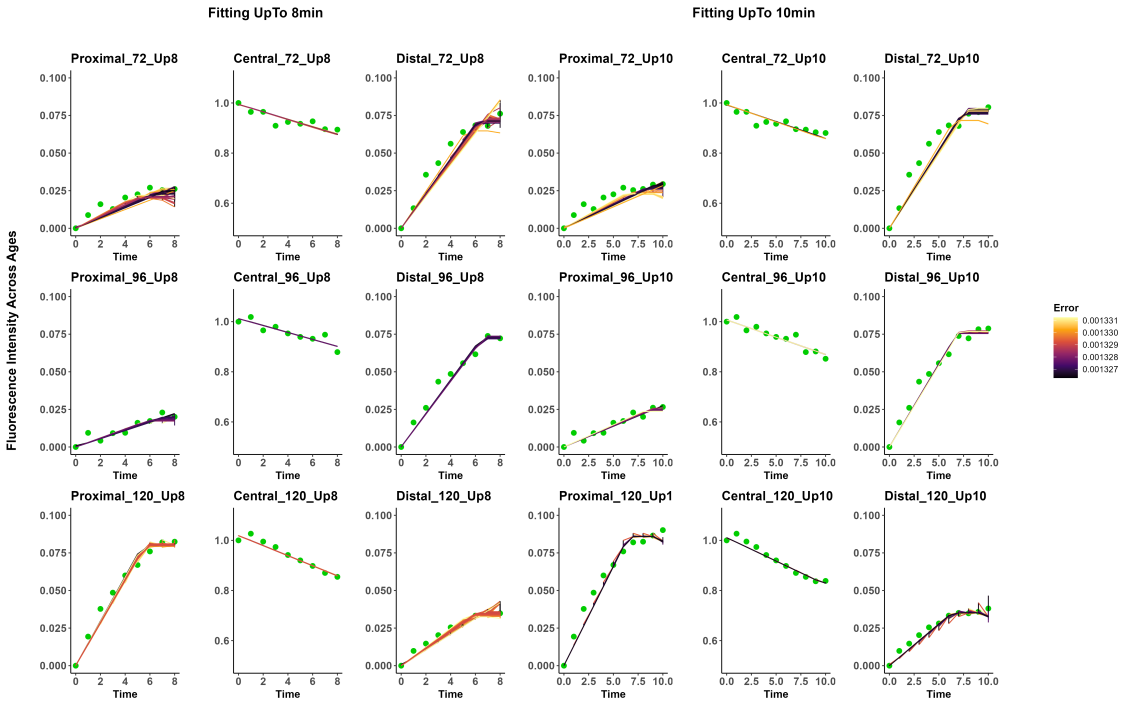

Figure 6.2: **Fitting of the pure transport** (5.1.2) **model to experimental data extended to 8 and 10 minutes.** the left panel shows fittings up to 8 minutes and the right panel extends to 10 minutes, with green points representing experimental data and coloured lines indicating model predictions coloured by error (darker shades indicate lower errors).

6.1.2 Parameters Analysis

We extracted transport parameters values (v_a, v_r, P_0, A_0, R_0) from 300 GA runs. To assess parameter ranges and their dynamics across developmental stages (72, 96, and 120 hpf), we generated scatter plots (Figure 6.3). These plots enable us to visualize the parameter value distributions over the different runs across three fitting time intervals: 5, 8, and 10 minutes (i.e. rows A, B, and C, respectively). In these plots, each estimated parameter value is represented by a coloured dot with colours indicating fitting errors (lower error is black and highest is yellow). Columns 1 to 5 represent v_a, v_r, P_0, A_0, and R_0, respectively. As the fitting interval extends from 5 to 10 minutes, the parameter estimates exhibit greater consistency and tighter convergence. The shift from A_0 dominance at 72 hpf to R_0 at 120 hpf reflects a developmental transition toward retrograde dominance. Table 6.1 is the summary of each parameter estimate from Figure 6.3 10 minutes, which shows that $\approx 80\%$ of the neurofilament population is pausing.

Table 6.1: Parameter estimates for pure transport model (5.1.2) across developmental stages (hpf) as derived from Figure 6.3C - 10 minutes estimates.

	72 hpf (lowest error)	96 hpf (lowest error)	120 hpf (lowest error)	Units
v_a	1.22-1.54 (1.53)	1.36-1.49 (1.39)	1.08-1.87 (1.34)	μm(min)$^{-1}$
v_r	0.05-1.71 (1.05)	0.08-1.54 (1.54)	1.45-1.58 (1.55)	μm(min)$^{-1}$
P_0	80–86 (85.11)	80–85.5 (85.44)	80–82.3 (81.50)	%
A_0	10.7–12.2 (10.79)	11.1–11.8(11.45)	5.1-15.8 (5.63)	%
R_0	3.3-10.8 (4.10)	3.11-15.6 (3.11)	12.6-13.1 (12.86)	%

6.1.3 Best Solution Analysis

To evaluate the performance of model (5.1.2), we selected the set of parameters – estimated up to 5, 8 and 10 minutes - corresponding to the lowest error among the 300 runs shown in Figure 6.3. These parameters were then used to simulate the model and compare its output with the experimental data (Figure 6.4, 6.5 and 6.6).

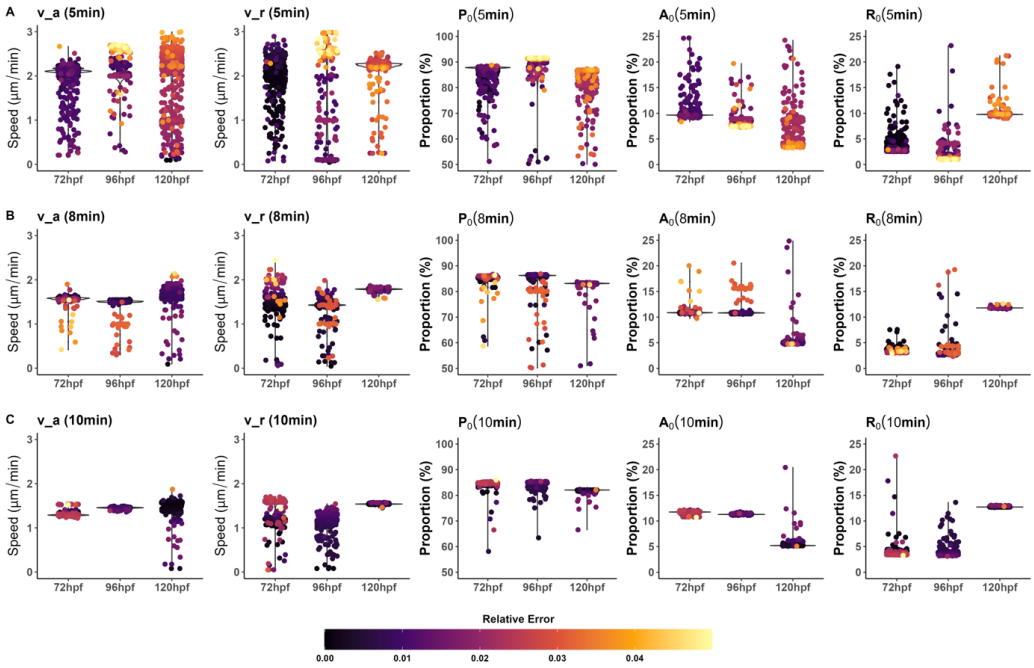

Figure 6.3: **Assessing uncertainty of pure transport model** (5.1.2) **parameters (v_a, v_r, P_0, A_0, R_0) from GA runs across 72, 96 and 120 hpf and time intervals 5, 8 and 10 minutes (rows A, B, and C, respectively).** Columns 1–5 represent v_a, v_r, P_0, A_0, and R_0, respectively. The dotted points are parameter values for different runs, with colours reflecting error (darker shades denote lower errors).

Fluorescence Intensity Over Time

Figures 6.4, 6.5 and 6.6 present the experimental data conservation range and best simulated fluorescence intensities using parameter values estimated from fitting up to 5, 8 and 10 minutes, respectively. Columns 1 show that the initial amount of photoactivated neurofilament in the central window is conserved (sum to 1: horizontal line) up to 10 minutes (vertical dashed line). Columns 2–4 show the fluorescence evolution for the proximal, central and distal compartments across 72, 96 and 120 hpf (rows 1–3). The model (5.1.2) accurately predicts the experimental data up to the respective fitting times—5, 8, and 10 minutes in Figure 6.4, 6.5 and 6.6, respectively. This alignment holds particularly well in capturing key trends: gradual increases in proximal fluorescence and steeper rises in distal fluorescence at 72 and 96 hpf, as well as a transition to a steeper increase in proximal fluorescence at 120

hpf. However, beyond the fitted time points, the model diverges from the experimental data. In particular, simulated fluorescence in the central compartment tends to plateau—where pausing becomes dominant ($\approx 80\%$)—while filament movement into the flanking windows slows down, and outward transport from the flanking windows persists. This deviation is likely due to the model's simplifying assumption of no exchange between the pausing, anterograde, and retrograde states.

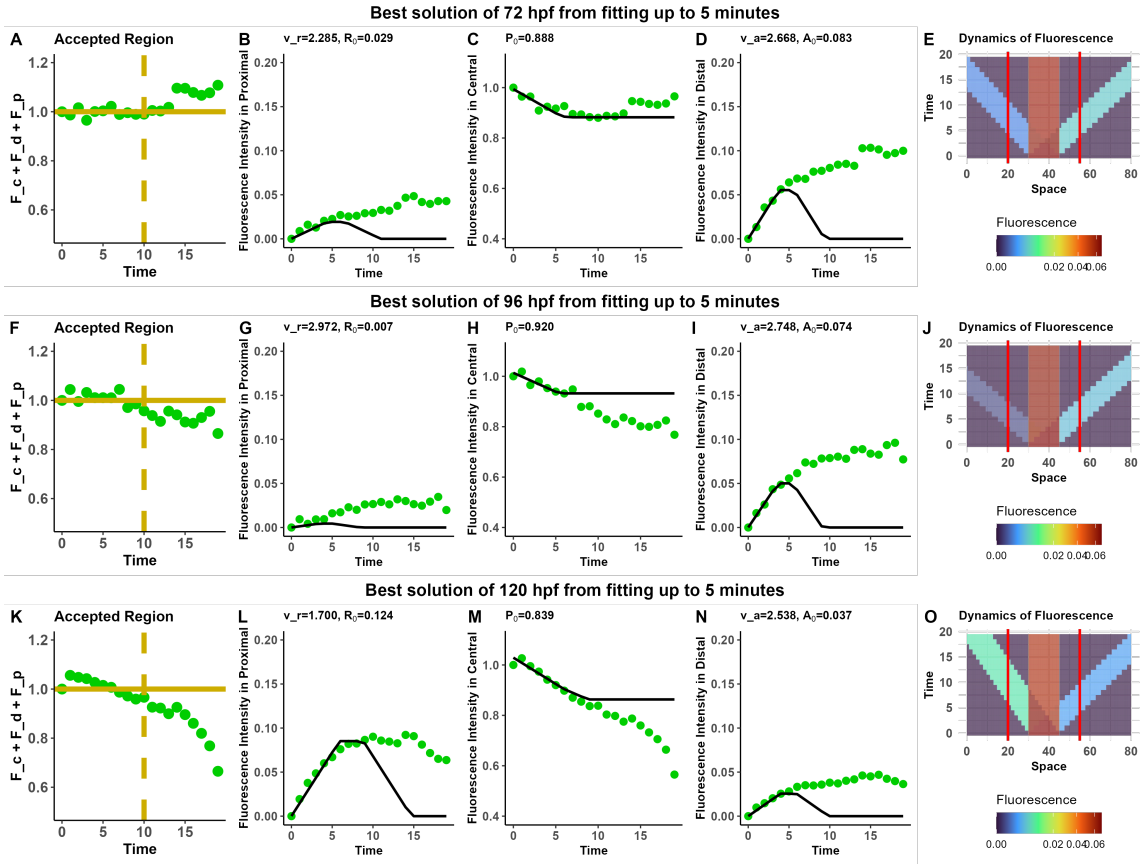

Figure 6.4: **Best solutions for the pure transport model** (5.1.2) **at 72, 96, and 120 hpf when fitting is performed up to 5 minutes.** Rows 1–3 correspond to 72, 96, and 120 hpf. Column 1 shows the conservation of photobleaching-corrected normalized fluorescence over time. The solid horizontal yellow line marks the expected conservation of photoactivated neurofilaments (total normalized fluorescence across all windows sums to 1), and the vertical dashed line indicates the end of conservation (10 minutes). Columns 2–5 show the results of parameters with the lowest error obtained from fitting up to 5 minutes. Columns 2–4 show fluorescence intensity over time for proximal (B, G, L), central (C, H, M), and distal windows (D, I, N), with green points representing experimental data and solid lines indicating model predictions. Column 5 (E, J, O) displays space-time dynamics of fluorescence, where colour intensity of fluorescence ranges from blue (low fluorescence) to red (high fluorescence). Vertical red lines mark flanking window boundaries: distal (20–30 μm), central (30–45 μm), and proximal (45–55 μm).

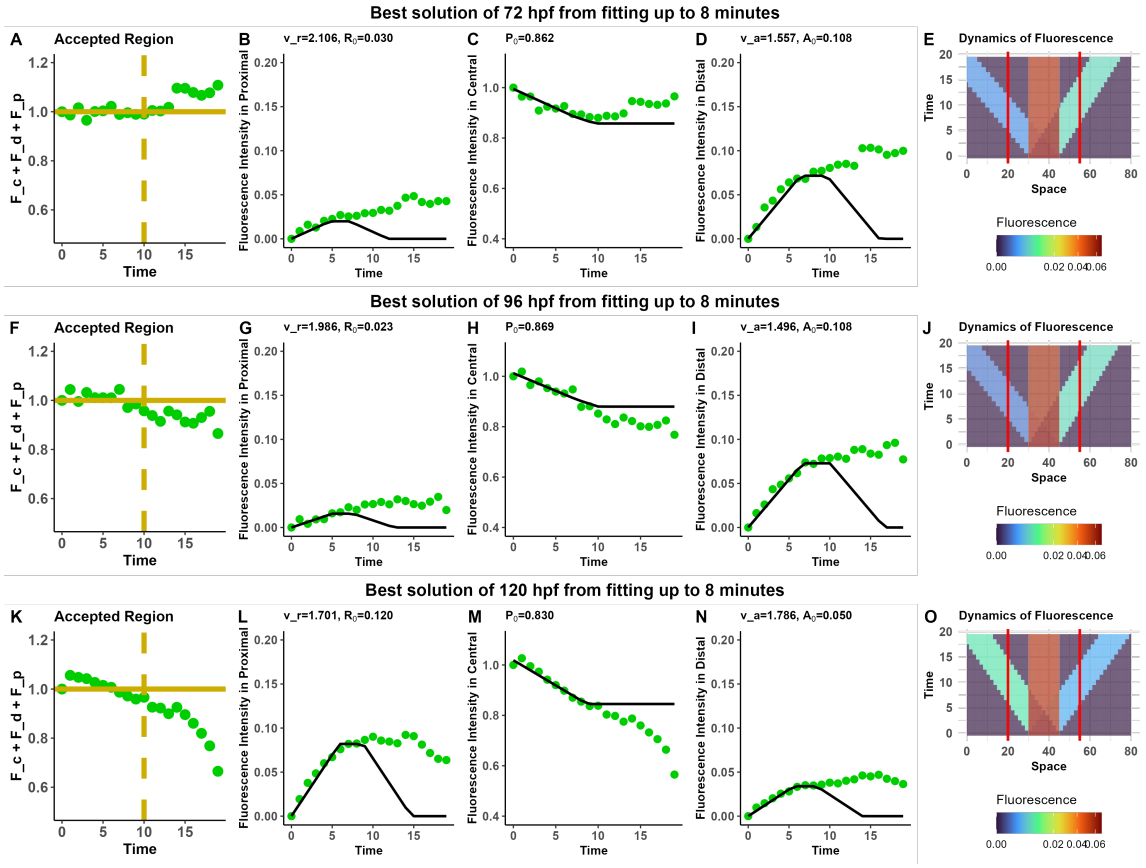

Figure 6.5: **Best solutions for the pure transport model** (5.1.2) **at 72, 96, and 120 hpf when fitting is performed up to 8 minutes.** Rows 1–3 correspond to 72, 96, and 120 hpf. Column 1 shows the conservation of photobleaching-corrected normalized fluorescence over time. The solid horizontal yellow line marks the expected conservation of photoactivated neurofilaments (total normalized fluorescence across all windows sums to 1), and the vertical dashed line indicates the end of conservation (10 minutes). Columns 2–5 show the results of parameters with the lowest error obtained from fitting up to 8 minutes. Columns 2–4 show fluorescence intensity over time for proximal (B, G, L), central (C, H, M), and distal windows (D, I, N), with green points representing experimental data and solid lines indicating model predictions. Column 5 (E, J, O) displays space-time dynamics of fluorescence, where colour intensity of fluorescence ranges from blue (low fluorescence) to red (high fluorescence). Vertical red lines mark flanking window boundaries: distal (20–30 μm), central (30–45 μm), and proximal (45–55 μm).

Space-Time Dynamics

Panels E, J, and O in Figures 6.4, 6.5 and 6.6 show solutions (5.1.1) that best represent data at 72, 96 and 120 hpf. These simulations visualize neurofilaments transport

through the spatial and temporal evolution of activated fluorescence intensity across the distal (20–30 μm), central (30–45 μm), and proximal (45–55 μm) windows. The region to the left of the central window up to the vertical red line is the proximal window and on the right up to the vertical red line marks the distal window.The horizontal axis represents the spatial domain along the axon, and the vertical axis represents time. The colour scale indicates fluorescence intensity, with dark red corresponding to higher neurofilaments concentrations. At the photoactivation time ($t = 0$), all photoactivated fluorescence is located in the central window (dark red region). Over time, fluorescence is transported bidirectionally - anterogradely toward the distal window (right) and retrogradely toward the proximal window (left) - driven by mobile neurofilaments transport. The slopes of these spreading regions reflect the velocities of the mobile neurofilaments populations. The fluorescence in the central region gradually decreases as mobile neurofilaments are transported out over time leaving only pausing neurofilaments in the central window.

At 72 and 96 hpf, the central compartment retains the highest fluorescence intensity (brown), with the distal region (light green) showing greater intensity than the proximal region (sky blue), confirming predominant anterograde transport. By 120 hpf, the proximal region displays stronger fluorescence than the distal region, indicating a clear shift to retrograde dominance, while the central compartment maintains elevated fluorescence due to sustained pausing.

This transition from anterograde dominance at earlier stages (72 and 96 hpf) to retrograde dominance at a later stage (120 hpf) is consistent with the pulse-spread analysis results presented in Section 3.2.4.

With this, our pure transport model (4.2.1), unlike the pulse-spread model, fits not only the linear stage of the data but also the nonlinear stage, which still retains the observations of linear fitting. So, our results, such as the amount of pausing population is 80% (Table 6.1), make sense.

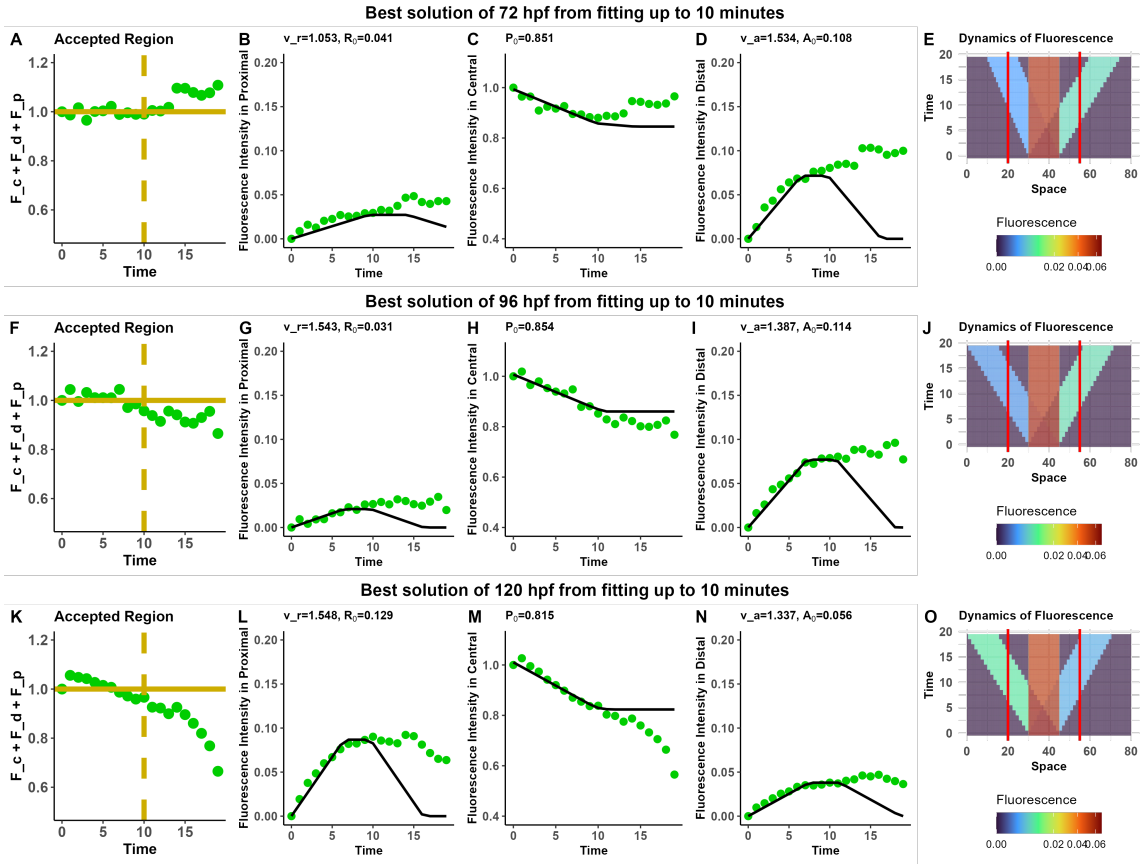

Figure 6.6: **Best solutions for the pure transport model** (5.1.2) **at 72, 96, and 120 hpf when fitting is performed up to 10 minutes.** Rows 1–3 correspond to 72, 96, and 120 hpf. Column 1 shows the conservation of photobleaching-corrected normalized fluorescence over time. The solid horizontal yellow line marks the expected conservation of photoactivated neurofilaments (total normalized fluorescence across all windows sums to 1), and the vertical dashed line indicates the end of conservation (10 minutes). Columns 2–5 show the results of parameters with the lowest error obtained from fitting up to 10 minutes. Columns 2–4 show fluorescence intensity over time for proximal (B, G, L), central (C, H, M), and distal windows (D, I, N), with green points representing experimental data and solid lines indicating model predictions. Column 5 (E, J, O) displays space-time dynamics of fluorescence, where colour intensity of fluorescence ranges from blue (low fluorescence) to red (high fluorescence). Vertical red lines mark flanking window boundaries: distal (20–30 μm), central (30–45 μm), and proximal (45–55 μm).

6.1.4 Effect of Central Window Length

Studies suggest that the length of the central window influences the estimation of departure rate of photoactivated neurofilaments, with longer windows increasing the

likelihood of on-track pausing and reducing the exit rate [1, 2]. To test this with our pure transport model, we fitted the model to data from two central window sizes: 15 μm and 5 μm. Data were collected at 0.5-minute intervals, and fitting was performed up to 2.5 minutes (Figure 6.7), as explained in Section 6.1.1.

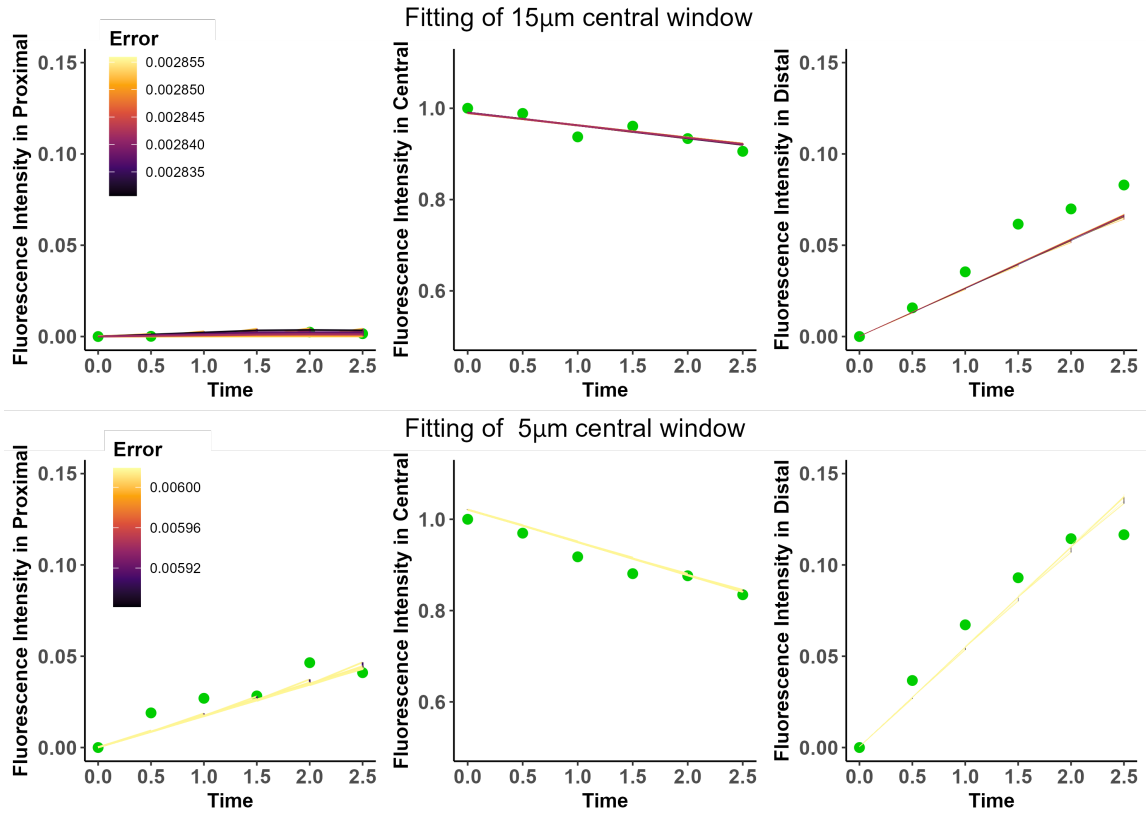

Figure 6.7: **Fitting of the pure transport model** (5.1.2) **to experimental data for central window sizes of 15 μm and 5 μm up to 2.5 minutes.** Green points represent experimental data for the proximal (first column), central (second column), and distal (third column) windows, while the coloured lines represent model outputs, with the colour gradient indicating fitting error levels (darker shades denote lower errors and better fit).

1. Parameter Distributions

The GA parameters were analysed using scatter plots (Figure 6.8), revealing converged values across time intervals for the central window lengths of 5 and 15μm.

- For the 5 μm windows, estimated velocities are $v_a \approx 1.5\,\mu\text{m(min)}^{-1}$ and $v_r \approx$

$1.7\,\mu\text{m}(\text{min})^{-1}$, with proportions $A_0 \approx 16\%$, $R_0 \approx 4\%$, and $P_0 \approx 80\%$.

- For the 15 μm window, velocities are $v_a \approx 2\,\mu\text{m}(\text{min})^{-1}$ and $v_r \approx 6\,\mu\text{m}(\text{min})^{-1}$, with proportions $A_0 \approx 19\%$, $R_0 \approx 1\%$, and $P_0 \approx 80\%$.

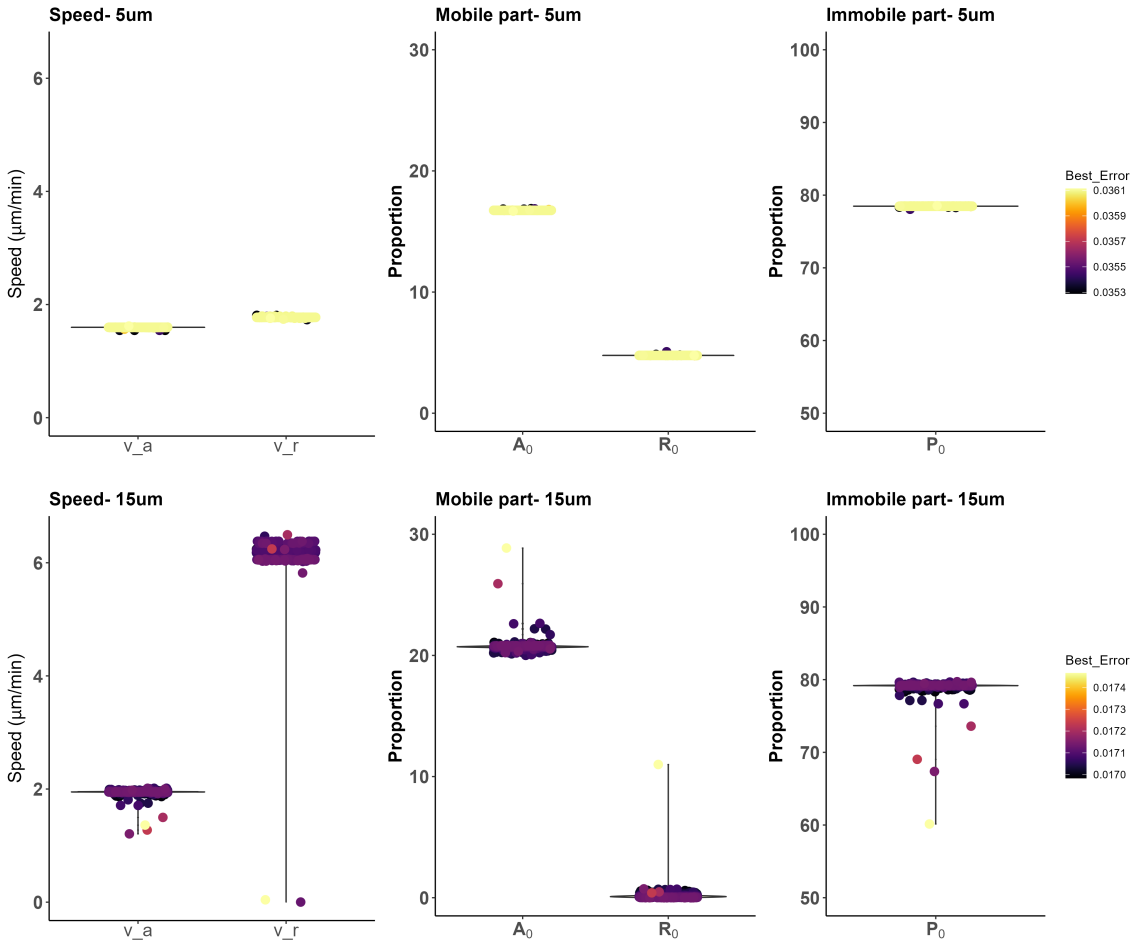

Figure 6.8: **Assessing uncertainty of pure transport model** (5.1.2) **parameters (v_a, v_r, P_0, A_0, R_0) from GA runs for central window sizes of 5 μm and 15 μm**. The first row is 5 μm central window and second row is 15 μm with colours indicating error (darker shades denote lower errors).

2. Best Solution and Dynamics

The best solution, based on the lowest error, was simulated to assess model performance and is compared to experimental data (Figure 6.9). The distal window shows a sharper fluorescence increase than the proximal window for both 5 μm (G) and 15

μm (C), confirming an anterograde bias of neurofilaments transport as stated above, unless reversed to retrograde bias only by age. Space-time plots of Figure 6.9 D, H, (see details in Section 6.1.3) support this, with light-green regions in the distal direction indicating higher fluorescence. The central window's fluorescence declines faster for 5 μm (F) than 15 μm (B), with all on-track filaments exiting the 5 μm window by approximately 2 minutes (H) versus after 6 minutes for 15 μm (D). This prolonged residence in the 15 μm window reflects a low exiting rate in a longer central window length, probably due to pausing or switching. This observation is consistent with our findings in Section 3.2.4

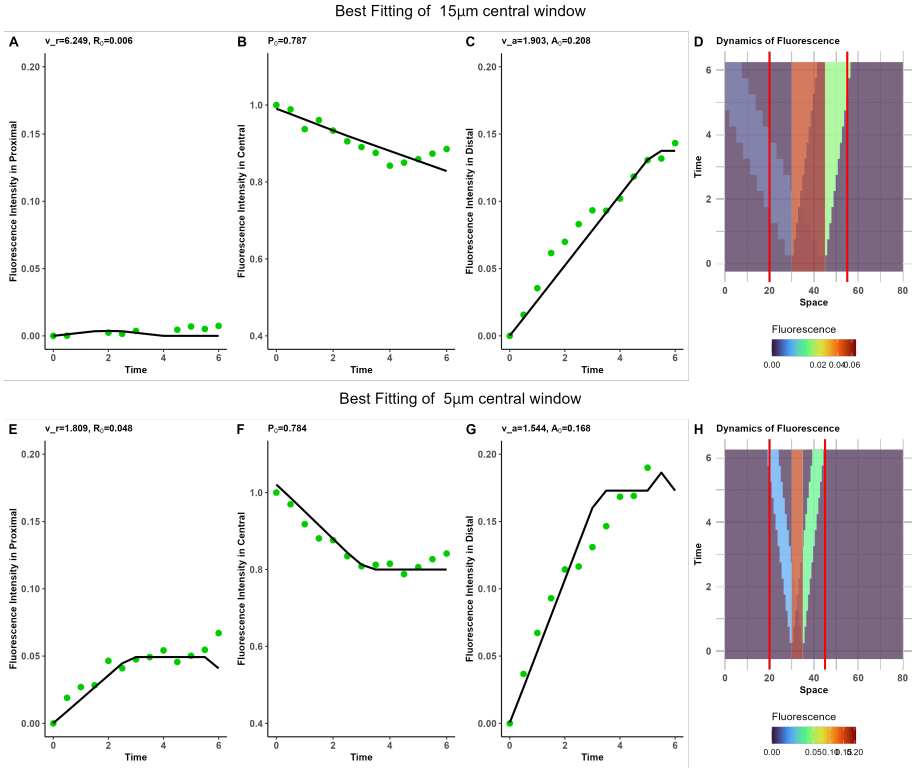

Figure 6.9: **Best solution simulation for central window sizes of 15 μm and 5 μm of** (5.1.2)**.** The first row (A–D) corresponds to 15 μm, and the second row (E–H) corresponds to 5 μm. Columns 1–3 (A–C, E–G) show fluorescence intensity over time for proximal, central, and distal windows, with green points as experimental data and coloured lines as model output (darker shades for lower errors). Columns 4 (D, H) depict space-time dynamics, with colours from blue (low fluorescence) to red (high fluorescence) and vertical red lines marking window boundaries (distal: 20–30 μm, central: 30–45 μm, proximal: 45–55 μm for D and distal: 20–30 μm, central: 30–35 μm, proximal: 35–45 μm for H).

6.2 Sensitivity of Pure Exchange Equilibrium

For the pure exchange model (4.3.1), this section analysed the sensitivity of the variations in parameters (λ_1, λ_2, γ_1, γ_2, ℓ_1, ℓ_2) on equilibrium distribution of neurofilaments populations as defined in (5.2.10). Sensitivity analysis quantifies how changes in these parameters affect the distribution of equilibrium values, offering insights into the factors driving the steady-state value of neurofilaments states in the pure exchange model. We employed Latin Hypercube Sampling (LHS) to conduct the sensitivity analysis and then used Partial Rank Correlation Coefficients (PRCCs) to assess the strength and direction of the relationship between parameters and equilibrium values[92, 93]. A positive PRCC indicates that increasing a parameter leads to an increase in the corresponding equilibrium value, while a negative PRCC implies that increasing the parameter leads to a decrease in the equilibrium value [94, 95, 96]. The PRCC values span from -1 to $+1$, with values exceeding $+0.5$ or falling below -0.5 indicating strong positive or negative correlations, respectively. Values around zero imply a minimal effect of the parameter on the model outcome [96].

The sensitivity analysis evaluates how model parameters influence the steady-state proportions of pausing, anterograde, and retrograde states using PRCCs. In addition, we simultaneously quantifies the steady-state neurofilaments populations (5.2.10) -p^*, a^*, and r^* - that represent the long-term distribution across the pausing, anterograde, and retrograde states, respectively.

6.2.1 Sensitivity with the Same Parameters Range

We first used the same range - $9 \times 10^{-7} s^{-1}$ to $5 \times 10^{-3} s^{-1}$ - for all parameter values to systematically explore the parameter space (first row in Table 6.2). The sensitivity analysis results are depicted in Figure 6.10(a).

In panel A, the analysis focuses on the effect of parameters uncertainty on the

steady-state pausing proportion, p^*. Parameters γ_1 and λ_1 exhibit strong positive PRCCs, indicating that increasing either parameter leads to an increase in p^*. Conversely, γ_2 and λ_2 show strong negative PRCCs, meaning that increasing them significantly reduces p^*. The parameters ℓ_1 and ℓ_2 have only minor positive effects on p^*.

In panel B, the focus shifts to the steady-state anterograde proportion, a^*. Here, ℓ_1 and γ_2 display strong positive PRCCs, suggesting that their increase promotes a higher a^*. In contrast, ℓ_2 and γ_1 show strong negative PRCCs, reducing a^* when increased. Parameters λ_1 and λ_2 contribute minimally to a^*.

Panel C examines the influences on the steady-state retrograde proportion, r^*. Parameters ℓ_2 and λ_2 exhibit strong positive PRCCs, meaning they significantly increase r^*, while ℓ_1 and λ_1 have strong negative PRCCs, decreasing r^* when increased. The effects of γ_1 and γ_2 on r^* are relatively minor but still positive.

These results reveal that parameters directly governing the flow into or out of a compartment—such as γ_1 and λ_1 for p^*—strongly affect the corresponding steady-state proportion. In contrast, parameters with no direct influence on a compartment's inflow or outflow—like ℓ_1 and ℓ_2 for p^*—exert minimal influence.

The accompanying distribution box plot (Figure 6.10(a)D) shows that the steady-state proportions p^*, a^*, and r^* are approximately uniformly distributed around 30%. This prediction contrasts with experimental observations that suggest a dominant pausing state.

6.2.2 Sensitivity Analysis Using Literature-Based Parameter Ranges

To refine the analysis, we applied parameter ranges derived from experimental studies, as outlined in Table 6.2. These ranges are based on literature-reported values, such as γ_1 and λ_1 ranging from 1.81×10^{-4} s^{-1} to 4.5×10^{-3} s^{-1}, and ℓ_1 from

3.7×10^{-7} s^{-1} to 4.7×10^{-5} s^{-1} [2, 3, 4].

This approach, illustrated in Figure 6.10(b), shows that the reversal rates ℓ_1 and ℓ_2 have negligible effects on the steady-state proportions p^*, a^*, and r^*, suggesting their minimal role in shaping the equilibrium distribution.

While the sensitivity of the pausing proportion p^* remains largely consistent across both parameter sets—dominated by γ_1, γ_2, λ_1, and λ_2—the sensitivity profiles of a^* and r^* differ markedly. Under uniform parameter ranges, many parameters appear influential, but only a few retain strong effects when literature-based ranges are applied. This underscores how biologically informed parameter sets improve model realism and clarify, which parameters truly govern system behaviour.

The distribution box plot (Figure 6.10(b)D) reveals a steady-state configuration dominated by p^* at approximately 80%, while a^* and r^* each stabilize around 12.5%. This outcome aligns more closely with experimental observations, which indicate a predominantly pausing state in the system.

Hence, we conclude that ℓ_1 and ℓ_2 can be reliably ignored in further modelling due to their limited influence.

Table 6.2: Parameter Ranges Used in Sensitivity Analysis are from [2, 3, 4]

Parameter	**Minimum value (s^{-1})**	**Maximum value (s^{-1})**
All	9×10^{-7}	5×10^{-3}
γ_1, λ_1	1.81×10^{-4}	4.5×10^{-3}
γ_2, λ_2	3.17×10^{-5}	2.8×10^{-4}
ℓ_1	3.7×10^{-7}	4.7×10^{-5}
ℓ_2	9×10^{-8}	1.9×10^{-5}

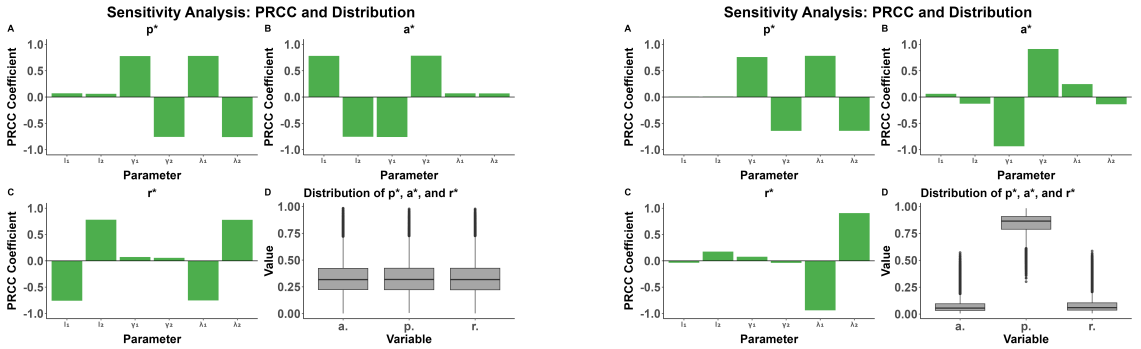

(a) (b)

Figure 6.10: **Sensitivity analysis of equilibrium proportions** (5.2.10) **using Partial Rank Correlation Coefficients (PRCCs) and their distributions. (a):** Panels A, B, and C show PRCCs for p^*, a^*, and r^* respectively, with respect to parameters ℓ_1, ℓ_2, γ_1, γ_2, λ_1, and λ_2. Positive PRCCs (green bars above zero) indicate an increase in the equilibrium value with parameter growth, while negative PRCCs (green bars below zero) indicate a decrease. Panel D displays the distribution of p^*, a^*, and r^* values, with box plots reflecting average values stabilizing around 30% for all variables under the initial uniform parameter range (Table 6.2). **(b):** Panels A, B, and C show PRCCs for p^*, a^*, and r^* respectively, with respect to parameters ℓ_1, ℓ_2, γ_1, γ_2, λ_1, and λ_2. Distribution of equilibrium proportions p^*, a^*, and r^* using literature-based parameter ranges, showing approximately 80% pausing, 12.5% anterograde, and 12.5% retrograde states, as indicated by the box plot medians and spreads.

6.3 The Transport-Exchange Model

To evaluate whether the inclusion of reaction terms improves the pure transport model, we fit the transport-exchange model with irreversible pausing (5.3.1) to experimental data collected at different developmental stages (72 hpf, 96 hpf and 120 hpf), as detailed in Section 6.1.1. As previously, the fitting procedure used 300 independent GA runs, and the resulting model fits are presented in Figure 6.11. The corresponding parameter distributions and summary estimates are shown in Figure 6.12 and Table 6.3. The model fitting was performed using data up to 5 minutes, corresponding to the duration of the linear regime identified in previous analyses.

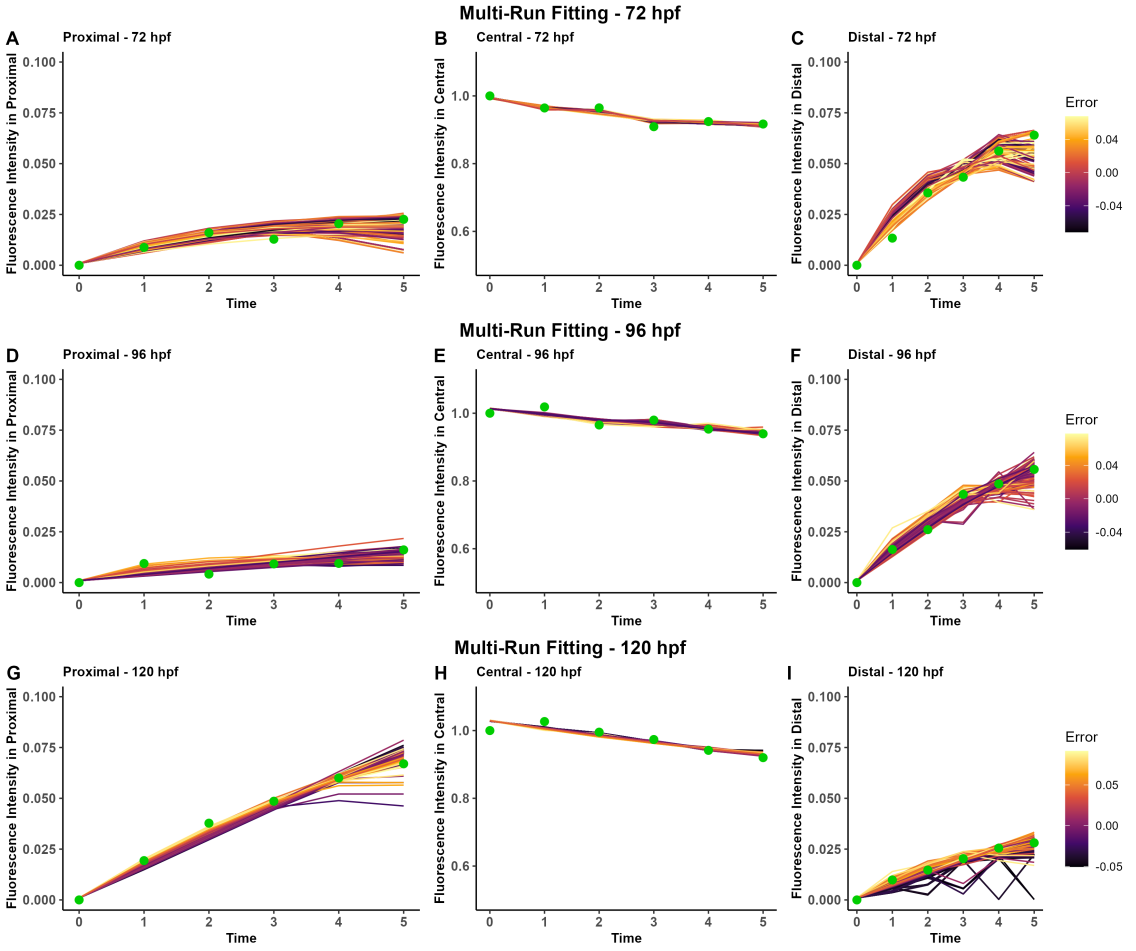

Figure 6.11: **Multi-run fitting of the neurofilaments transport-exchange model** (5.3.1) **to experimental data at 72 hpf (A-C), 96 hpf (D-F) and 120 hpf (G-I) across proximal (A, D, G), central (B, E, H) and distal (C, F, I) windows.** Green dots represent the normalized fluorescence intensity data from the pulse-spread experiment, while the coloured lines depict the transport-exchange model predictions for each of the 300 GA runs. The error scales indicate the range of fitting errors, with lower values (darker colours) reflecting better fits.

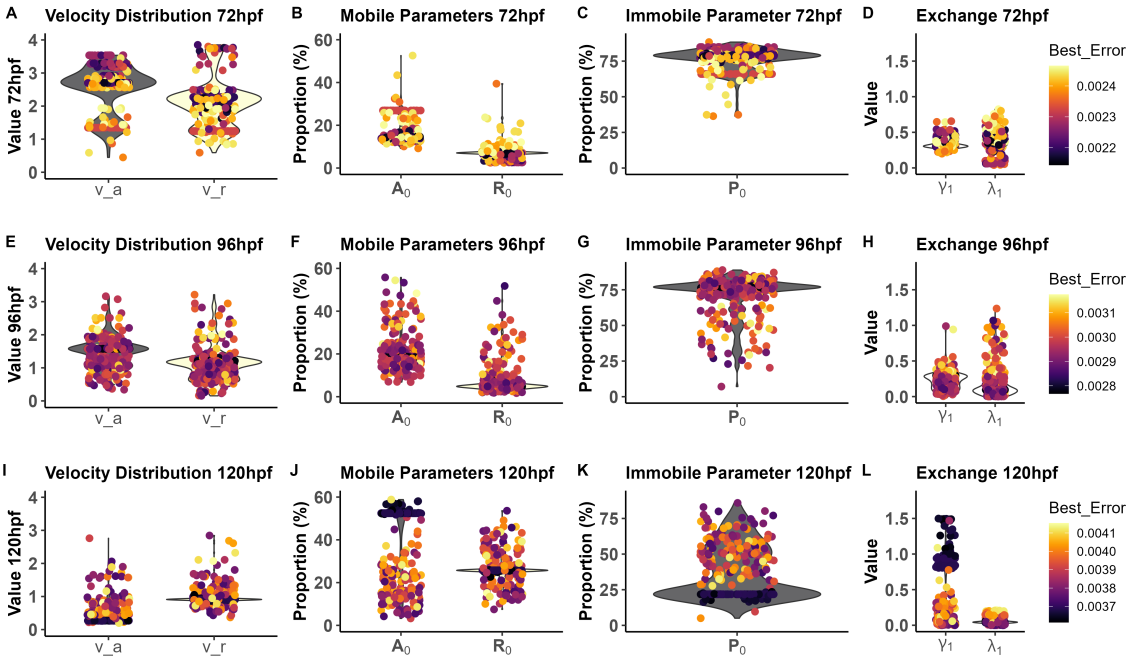

Figure 6.12: **Parameter distributions from 300 GA runs corresponding to Figure 6.11, shown for 72 hpf (A–D), 96 hpf (E–H) and 120 hpf (I–L).** Panels show: (A, E, I) velocities (v_a, v_r); (B, F, J) mobile parameters (A_0, R_0); (C, G, K) immobile parameter (P_0) and (D, H, L) exchange parameters (γ_1, λ_1). The width of each violin represents the density of parameter values and fit errors indicated by colour scales (lower values in darker colours).

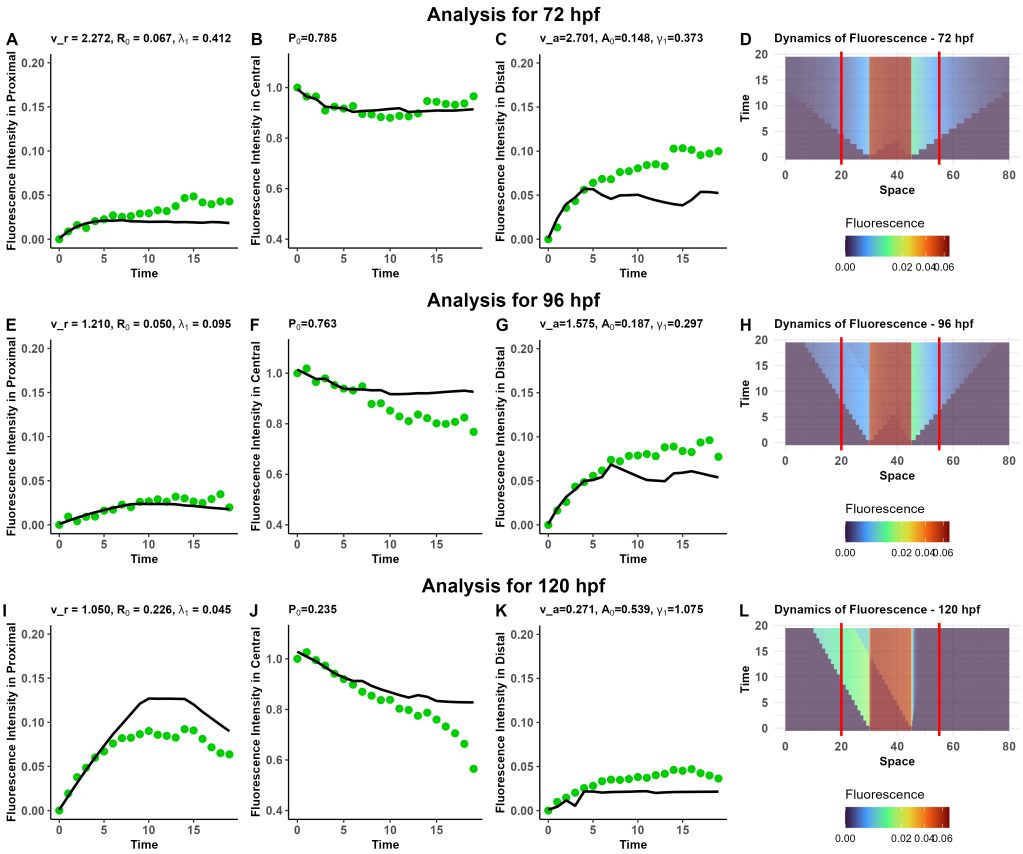

Figure 6.13: **Best fit of the transport-exchange model** (5.3.1) **at 72 hpf (A-D), 96 hpf (E-H) and 120 hpf (I-L).** (A, E, I) Proximal window fits with v_r, R_0 and λ_1 values. (B, F, J) central window fits with P_0 values. (C, G, K) distal window fits with v_a, A_0 and γ_1 values. Black lines represent model fits and green dots are experimental data. (D, H, L) spacetime plots simulating fluorescence dynamics over space and time, with colour intensity reflecting fluorescence levels.

For validation, we selected parameter sets with the lowest fitting error from the GA runs and simulated the model to compare with photobleaching-corrected fluorescence intensity data. Figure 6.13 illustrates these fits: Panels A, E, and I show proximal window fit; Panels B, F, and J depict central window fits; and Panels C, G, and K display distal window fits. The black lines represent the model predictions, which align well with the green experimental data points up to 5 minutes at all stages, although the accuracy decreases thereafter. The spacetime plots (Panels D, H, L) visualize the spread of fluorescence, with colour intensity indicating neurofilament distribution. At 72 hpf and 96 hpf, fluorescence propagates outward from the

central window, with a slight population bias toward the proximal side. This pattern is consistent with the predictions of the pure transport model. At 120 hpf, the retrograde movement dominates, consistent with the pure transport model, suggesting age-dependent transport dynamics.

6.3.1 Comparing Models: Pulse-Spread vs. Pure Transport vs. Transport-Exchange

To evaluate the performance of our neurofilaments transport models, we compared the best-fit results of the pure transport model (4.2.1) and transport-exchange model with irreversible pausing (4.4.1), using fits obtained from the first 5 minutes of data for both models. The pure transport model assumes no reaction terms ($\gamma_1 = \lambda_1 = 0$), focusing exclusively on advection, whereas the transport-exchange model includes irreversible transitions from mobile to immobile states. Model predictions were compared to experimental fluorescence intensity data at 72, 96 and 120 hpf.

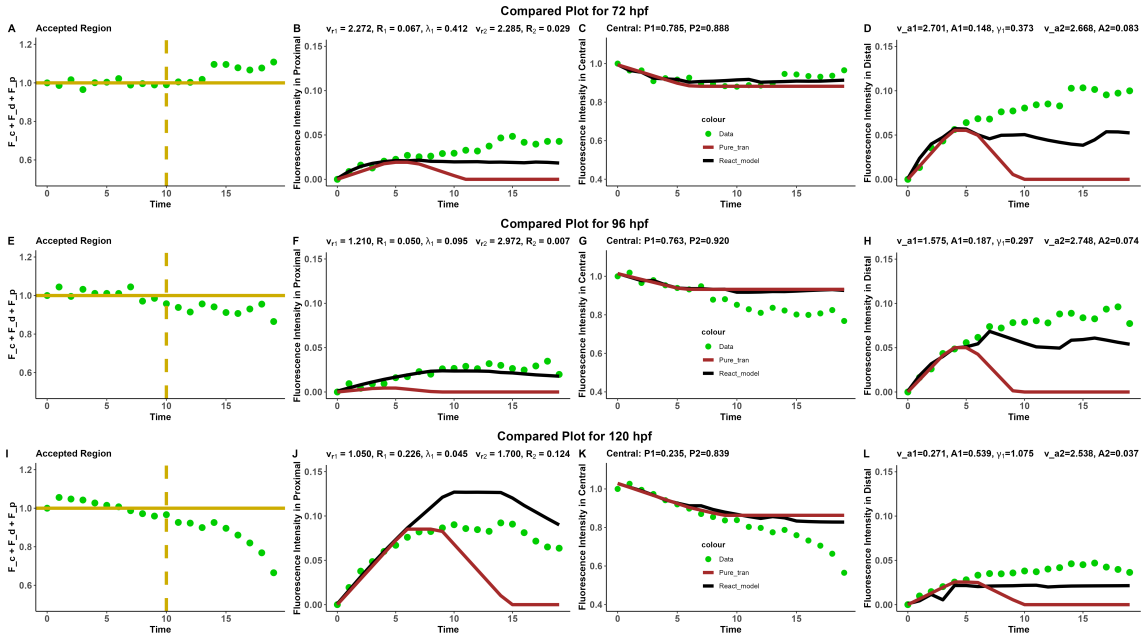

Figure 6.14: **Comparison of best-fit models (pure transport vs. transport-exchange) and conservation of photobleaching-corrected data at 72 hpf (A–D), 96 hpf (E–H) and 120 hpf (I–L).** Panels A, E, and I show the total fluorescence (sum across all windows), while B, F, J correspond to the proximal window, C, G, K to the central window, and D, H, L to the distal window. The solid horizontal yellow line marks the expected conservation of photoactivated neurofilaments (normalized to 1), and the vertical dashed line indicates the end of reliable data (10 minutes). Green dots represent experimental data. Red lines correspond to fits from the pure transport model (5.1.2), and black lines show the transport-exchange model fits (5.3.1).

Figure 6.14 illustrates their comparison. The solid horizontal yellow lines in panels (A, E, I) indicate the conservation of photoactivated neurofilaments after photobleaching correction across all windows, summing to one, while the vertical dashed line marks the endpoint conservation of data at 10 minutes. Experimental data beyond this point are not considered reliable.

In the proximal region (Panels B, F, J), both the pure transport model (red) and the transport-exchange model (black) adequately capture the initial rise and early plateau in fluorescence intensity within the fitting interval (0–5 minutes) at 72 hpf but at 96 hpf transport-exchange predict the fluorescence far better. At 120 hpf, however, both models begin to diverge more noticeably from the data after the 5

minutes point, with the transport-exchange model overshooting the peak and failing to capture the subsequent decline observed in the experimental data. However, the pure transport model could only capture the plateau for about a minute and deviate thereafter.

In the central region (Panels C, G, K), both models fit reasonably well up to 5 minutes but begin to deviate in their predictions beyond that point. Between 5–10 minutes, the data show a more gradual decline in intensity, which neither model fully reproduces.

In the distal region (Panels D, H, L), both models struggle to reproduce the rising fluorescence trend seen beyond 5 minutes. Although both models better track the early rise at 72 hpf and 96 hpf, they fail to match the later plateau. The transport-exchange model, on the other hand, underpredicts fluorescence intensities at 120 hpf, even before 5 minutes.

Overall, both models exhibit similar performance within the fitting window (0–5 minutes), which is expected since they were calibrated using data from this interval. However, they begin to diverge in the prediction window (5–10 minutes), reflecting differences in their underlying mechanisms. The transport-exchange model produced lower fitting errors (0.002144, 0.002767, 0.003613) compared to the pure transport model (0.003128, 0.003147, 0.003764) at 72, 96, and 120 hpf, respectively. This suggests that the transport-exchange model better captures the observed dynamics during the calibration time. Beyond the 5-minute mark, both models deviate from the data, indicating that the inclusion of exchange parameters (γ_1, λ_1) offers limited improvement in predictive accuracy within the short timescale of the pulse-spread experiments. This supports the interpretation that exchange processes may play a minor role in shaping neurofilaments distribution over this duration.

To compare the parameter estimates obtained with data up to 5 minutes across models, we present Table 6.3, which summarizes the parameters from best fit plots

for the transport-exchange, pure transport, and previously analyzed pulse-spread models (3.1.9), (3.1.10) and (3.1.11). The table highlights distinct trends between the models. The pulse-spread model, characterized by the values of S_d, S_p, and $\bar{v}$, indicates a switch from anterograde bias to retrograde dominance with age. Consistent with this, both the transport-exchange model and pure transport model exhibit a shift from A_0 dominance at 72 and 96 hpf, to R_0 dominance at 120 hpf. This is reflected in the directional bias (S_d/S_p, $\bar{v}$), showing a developmental transition from anterograde to retrograde dominance. Furthermore, the transport-exchange model and the pure transport model maintain a consistent P_0 (70-80%) across all ages, underscoring the dominance of pausing behaviour, a feature not captured by the pulse-spread model. In contrast, the transport-exchange model, incorporating the exchange parameters γ_1 and λ_1, displays increasing variability in mobile proportions (A_0, R_0) as development progresses from 72 to 120 hpf, alongside a notable decrease in the immobile proportion P_0 at 120 hpf. This suggests that exchange dynamics diverge from the patterns observed in both the pulse-spread and pure transport models, justifying their exclusion in both models.

Table 6.3: Parameter estimates for pulse-spread, pure transport and transport-exchange models across developmental stages (hpf). The pure transport and transport-exchange model directional bias was calculated as follows: $\frac{S_d}{S_p} \approx \frac{v_a A_0}{v_r R_0}$ and $\bar{v} \approx (v_a A_0 - v_r R_0)$.

Model	Parameter	72 hpf	96 hpf	120 hpf	Units
Pulse-Spread	S_d	1.40	1.39	0.64	min^{-1}
	S_p	0.50	0.32	1.45	min^{-1}
	S_c	2.41	1.10	1.18	min^{-1}
	$\frac{S_d}{S_p}$	2.20	1.50	0.40	-
	$\bar{v}$	0.23	0.26	-0.20	mm(day)^{-1}
Pure Transport	v_a	2.668	2.748	2.538	$\mu\text{m(min)}^{-1}$
	v_r	2.285	2.972	1.7	$\mu\text{m(min)}^{-1}$
	P_0	88.77	91.95	83.89	%
	A_0	8.33	7.4	3.72	%
	R_0	2.9	0.65	12.39	%
	$\frac{v_a A_0}{v_r R_0}(\frac{S_d}{S_p})$	3.35	10.53	0.45	-
	$\bar{v}$	0.22	0.27	-0.17	mm(day)^{-1}
Transport-Exchange	v_a	2.701	1.575	0.271	$\mu\text{m(min)}^{-1}$
	v_r	2.272	1.210	1.050	$\mu\text{m(min)}^{-1}$
	P_0	78.5	76.3	23.5	%
	A_0	14.8	18.7	53.9	%
	R_0	6.7	5	22.6	%
	γ_1	0.373	0.297	1.075	min^{-1}
	λ_1	0.412	0.095	0.045	min^{-1}
	$\frac{v_a A_0}{v_r R_0}(\frac{S_d}{S_p})$	2.63	4.87	0.55	-
	$\bar{v}$	0.36	0.34	-0.15	mm(day)^{-1}

7

Discussion and Conclusion

In this study, we investigated the transport dynamics of neurofilaments in zebrafish through mathematical modelling and computational simulations (Figure 3.7), using experimental pulse-spread data provided by Bomont's lab. Our analysis began by applying the pulse-spread modelling framework developed by Boyer *et al.* [1], which describes neurofilaments dynamics within the initial linear regime and provides estimates of key transport parameters such as mean velocity and directionality (i.e., the rate of neurofilaments entering the flanking windows). This linear approximation, based on a Taylor expansion around $t = 0$, is strictly valid during the very early phase following photoactivation. Consequently, this approach yields early-time parameter estimates. Our results from pulse-spread analysis confirmed that neurofilaments transport in zebrafish is bidirectional with anterograde bias, a trend that reversed with age - a finding consistent with studies in mice [1, 2]. However, the pulse-spread model lacked the capacity to describe essential features such as pausing, the balance of anterograde versus retrograde transport, and the exchange dynamics between states.

To address the limitations of the pulse-spread approach, we developed a reaction–diffusion–advection modelling framework that incorporates key transport fea-

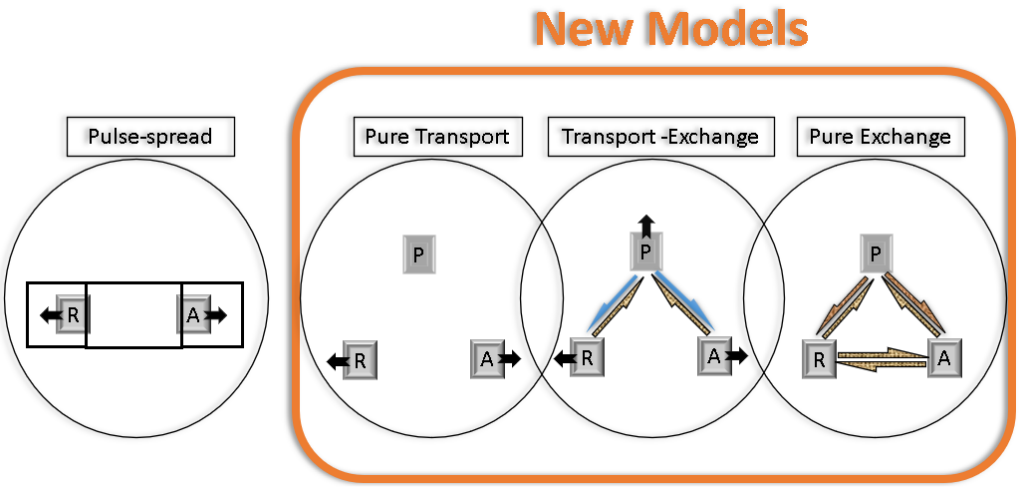

Figure 7.1: **Summary of models developed and analysed in this research work.** The pulse-spread refers to the model previously developed by [1]. The new models - the pure transport, pure exchange, and pure transport-exchange models - were developed here to address specific questions.

tures as well as switching between mobile states and pausing, which missing in previous analyses (Figure 3.7). Our framework is based on earlier neurofilaments transport studies [1, 2, 3], explicitly accounting for bidirectional transport, pausing, and interaction between anterograde and retrograde dynamics. From this generalized PDE system, we derived four sub-models: the pure exchange model, the pure transport model, the transport–exchange model with reversible pausing, and the transport–exchange model with irreversible pausing. Each of these captures distinct aspects of neurofilaments dynamics.

Applying the pure transport model, which neglects reaction and diffusion terms and assumes no state switching, thus extending the pulse-spread approach, to zebrafish neurofilaments data, we investigated the effects of central window length and age on transport dynamics. Our simulations revealed that pausing populations is consistently the highest across different window lengths and ages, while anterograde bias observed at early ages shifts toward retrograde dominance in later stages. We also found that increasing the central window length prolonged the overall residence time of neurofilaments, thereby increasing the likelihood of pausing.

Analysis of the transport-exchange model with reversible pausing, which incorporates both state switching and active transport (but excludes diffusion of pausing states), showed that exchange processes dominate transport at steady state.

Finally, investigation of the pure exchange model, which isolates reaction terms by decoupling diffusion and advection, demonstrated that it possesses a unique and stable equilibrium. This finding indicates robustness in maintaining neurofilaments distributions under steady-state conditions. Importantly, switching rates between anterograde and retrograde directions did not alter the equilibrium distribution, suggesting that neurofilaments transport maintains a stable homeostatic balance. Such stability may ensure consistent intracellular delivery of neurofilaments despite variability in cellular conditions.

In summary, this study developed a general mathematical model and analysed four sub-models to investigate specific features of neurofilament transport in zebrafish (Figure 7.1). The main findings of these models are in Table 7.1. By integrating experimental data with mathematical modelling, we gained valuable insights into the underlying dynamics of this complex biological process. Our findings suggest that the transport mechanisms observed in zebrafish share similarities with those in other species [1, 2], such as mice, but also exhibit unique characteristics that warrant further investigation.

These results open avenues for future research in a key directions: Exploring environmental and developmental influences - Investigating how factors such as stress, injury, or genetic modifications affect neurofilaments transport could enhance our knowledge of neurodegenerative diseases and axonal function.

Overall, our modelling approach provides a valuable framework for studying intracellular transport mechanisms and offers a foundation for future experimental and theoretical advancements in neurofilaments dynamics.

Table 7.1: Main findings in the study.

Model	**Key Finding**
Pulse-spread	• Neurofilaments transport is anterogradely biased • Neurofilaments anterograde bias reverses with age
Pure transport	• Neurofilaments anterograde bias reverses with age • About 80% of Neurofilaments are pausing (<1h)
Transport-exchange	• Switching mobile and immobile states dominates transport at steady state
Pure exchange	• Switching between anterograde and retrograde directions does not affect the steady-state distribution

Appendix A

Appendix

A.1 Eigenvalues and Eigenvectors

Eigenvalues:

To find the engenvalues of the coefficient matrix in (5.3.11), we let

$$M = \frac{1}{(\lambda_2 + \gamma_2)} \begin{pmatrix} \frac{-\gamma_1\lambda_2}{v_a} & \frac{\gamma_2\lambda_1}{v_a} \\ \frac{-\lambda_2\gamma_1}{v_r} & \frac{\lambda_1\gamma_2}{v_r} \end{pmatrix}$$

be the matrix.

The characteristic equation of M (see, Section 2.1.1) is:

$$\det(M - \mu I) = 0,$$

with

$$\det(M-\mu I) = \left(\frac{-\gamma_1\lambda_2}{v_a(\lambda_2+\gamma_2)} - \mu\right)\left(\frac{\lambda_1\gamma_2}{v_r(\lambda_2+\gamma_2)} - \mu\right) - \left(\frac{\gamma_2\lambda_1}{v_a(\lambda_2+\gamma_2)}\right)\left(\frac{-\lambda_2\gamma_1}{v_r(\lambda_2+\gamma_2)}\right).$$

$$\implies \left(\frac{\gamma_2\lambda_1}{v_a(\lambda_2+\gamma_2)}\right)\left(\frac{-\lambda_2\gamma_1}{v_r(\lambda_2+\gamma_2)}\right) = \frac{-\gamma_2\lambda_1\lambda_2\gamma_1}{v_a v_r(\lambda_2+\gamma_2)^2}.$$

Let's define:

$$a = \frac{\gamma_1\lambda_2}{v_a(\lambda_2+\gamma_2)}, \quad b = \frac{\lambda_1\gamma_2}{v_r(\lambda_2+\gamma_2)}, \quad c = \frac{\gamma_2\lambda_1\lambda_2\gamma_1}{v_a v_r(\lambda_2+\gamma_2)^2}.$$

The characteristic equation becomes:

$$(-a-\mu)(b-\mu) - (-c) = 0,$$

$$\mu^2 + (a-b)\mu + (-ab+c) = 0.$$

Compute the coefficients:

- $a - b = \frac{\gamma_1\lambda_2}{v_a(\lambda_2+\gamma_2)} - \frac{\lambda_1\gamma_2}{v_r(\lambda_2+\gamma_2)} = \frac{\gamma_1\lambda_2 v_r - \lambda_1\gamma_2 v_a}{v_a v_r(\lambda_2+\gamma_2)}$,
- $-ab = -\left(\frac{\gamma_1\lambda_2}{v_a(\lambda_2+\gamma_2)}\right)\left(\frac{\lambda_1\gamma_2}{v_r(\lambda_2+\gamma_2)}\right) = -\frac{\gamma_1\lambda_2\lambda_1\gamma_2}{v_a v_r(\lambda_2+\gamma_2)^2}$,
- $c = \frac{\gamma_2\lambda_1\lambda_2\gamma_1}{v_a v_r(\lambda_2+\gamma_2)^2}$,
- So, $-ab + c = -\frac{\gamma_1\lambda_2\lambda_1\gamma_2}{v_a v_r(\lambda_2+\gamma_2)^2} + \frac{\gamma_2\lambda_1\lambda_2\gamma_1}{v_a v_r(\lambda_2+\gamma_2)^2} = 0.$

Thus, the characteristic equation simplifies to:

$$\mu^2 + (a-b)\mu = 0,$$

The eigenvalues are:

$$\mu_1 = 0, \quad \mu_2 = b - a = \frac{\lambda_1\gamma_2 v_a - \gamma_1\lambda_2 v_r}{v_a v_r(\lambda_2+\gamma_2)}.$$

Eigenvectors:

- For $\mu_1 = 0$:

$$M \begin{pmatrix} v_1 \\ v_2 \end{pmatrix} = 0,$$

$$\begin{pmatrix} -a & \frac{\gamma_2\lambda_1}{v_a(\lambda_2+\gamma_2)} \\ \frac{-\lambda_2\gamma_1}{v_r(\lambda_2+\gamma_2)} & b \end{pmatrix} \begin{pmatrix} v_1 \\ v_2 \end{pmatrix} = 0.$$

  First row: $-av_1 + \frac{\gamma_2\lambda_1}{v_a(\lambda_2+\gamma_2)}v_2 = 0$,

$$v_2 = \frac{av_a(\lambda_2+\gamma_2)}{\gamma_2\lambda_1}v_1 = \frac{\gamma_1\lambda_2}{\gamma_2\lambda_1}v_1.$$

  Eigenvector: $\begin{pmatrix} v_1 \\ \frac{\gamma_1\lambda_2}{\gamma_2\lambda_1}v_1 \end{pmatrix}$, so choose $v_1 = 1$: $\begin{pmatrix} 1 \\ \frac{\gamma_1\lambda_2}{\gamma_2\lambda_1} \end{pmatrix}$.

- For $\mu_2 = b - a$:

$$(M - (b-a)I) \begin{pmatrix} v_1 \\ v_2 \end{pmatrix} = 0,$$

$$\begin{pmatrix} -b & \frac{\gamma_2\lambda_1}{v_a(\lambda_2+\gamma_2)} \\ \frac{-\lambda_2\gamma_1}{v_r(\lambda_2+\gamma_2)} & a \end{pmatrix} \begin{pmatrix} v_1 \\ v_2 \end{pmatrix} = 0.$$

  First row: $-bv_1 + \frac{\gamma_2\lambda_1}{v_a(\lambda_2+\gamma_2)}v_2 = 0$,

$$v_2 = \frac{bv_a(\lambda_2+\gamma_2)}{\gamma_2\lambda_1}v_1 = \frac{\lambda_1\gamma_2}{v_r(\lambda_2+\gamma_2)} \cdot \frac{v_a(\lambda_2+\gamma_2)}{\gamma_2\lambda_1}v_1 = \frac{v_a}{v_r}v_1.$$

  Eigenvector: $\begin{pmatrix} v_1 \\ \frac{v_a}{v_r}v_1 \end{pmatrix}$, so choose $v_1 = 1$: $\begin{pmatrix} 1 \\ \frac{v_a}{v_r} \end{pmatrix}$.

We determined the arbitrarily constants c_1 and c_2 from the general solution

(5.3.12) using its boundary conditions. From the general solution, we have

$$A_\infty(x) = c_1 + c_2 e^{\mu_2 x},$$

$$\frac{dA_\infty}{dx} = c_2 \mu_2 e^{\mu_2 x},$$

$$R_\infty(x) = c_1 \frac{\gamma_1 \lambda_2}{\gamma_2 \lambda_1} + c_2 \frac{v_a}{v_r} e^{\mu_2 x},$$

$$\frac{dR_\infty}{dx} = c_2 \frac{v_a}{v_r} \mu_2 e^{\mu_2 x}.$$

For A_∞:

- At $x = 0$:

$$\left.\frac{dA_\infty}{dx}\right|_{x=0} = c_2 \mu_2 e^{\mu_2 \cdot 0} = c_2 \mu_2 = 0.$$

  If $\mu_2 \neq 0$, then $c_2 = 0$.

- At $x = L$:

$$\left.\frac{dA_\infty}{dx}\right|_{x=L} = c_2 \mu_2 e^{\mu_2 L} = 0.$$

  Again, $c_2 = 0$, which is consistent.

For R_∞:

- At $x = 0$:

$$\left.\frac{dR_\infty}{dx}\right|_{x=0} = c_2 \frac{v_a}{v_r} \mu_2 e^{\mu_2 \cdot 0} = c_2 \frac{v_a}{v_r} \mu_2 = 0.$$

  This confirms $c_2 = 0$, consistent with the previous condition.

- At $x = L$:

$$\left.\frac{dR_\infty}{dx}\right|_{x=L} = c_2 \frac{v_a}{v_r} \mu_2 e^{\mu_2 L} = 0.$$

  Again, $c_2 = 0$, which is consistent under the condition that $\frac{\gamma_1 \lambda_2}{\gamma_2 \lambda_1} \neq \frac{v_a}{v_r}$.

References

[1] Nicholas P Boyer, Jean-Pierre Julien, Peter Jung, and Anthony Brown. Neurofilament transport is bidirectional in vivo. eneuro, 9(4), 2022.

[2] Yinyun Li, Anthony Brown, and Peter Jung. Deciphering the axonal transport kinetics of neurofilaments using the fluorescence photoactivation pulse-escape method. Physical biology, 11(2):026001, 2014.

[3] Peter Jung and Anthony Brown. Modeling the slowing of neurofilament transport along the mouse sciatic nerve. Physical Biology, 6(4):046002, 2009.

[4] Rawan M Nowier, Anika Friedman, Anthony Brown, and Peter Jung. The role of neurofilament transport in the radial growth of myelinated axons. Molecular biology of the cell, 34(6):ar58, 2023.

[5] Felix Dujardin. Recherches sur les organismes inférieurs. Impr. chez P. Renouard, 1835.

[6] Manfred Schliwa. The cytoskeleton: An introductory survey, volume 13. Springer Science & Business Media, 2012.

[7] Miri Yoon, Robert D Moir, Veena Prahlad, and Robert D Goldman. Motile properties of vimentin intermediate filament networks in living cells. The Journal of cell biology, 143(1):147–157, 1998.

[8] Bruce Alberts, Alexander Johnson, Julian Lewis, Martin Raff, Keith Roberts, and Peter Walter. Molecular biology of the cell, 5th edn. garland science. New York, 2008.

[9] Daniel A Fletcher and R Dyche Mullins. Cell mechanics and the cytoskeleton. Nature, 463(7280):485–492, 2010.

[10] Simon Muriithi Karuku. Contribution of dynamic instability to microtubule organization. 2008.

[11] Anne-Betty Ndiaye, Gijsje H Koenderink, and Michal Shemesh. Intermediate filaments in cellular mechanoresponsiveness: mediating cytoskeletal crosstalk from membrane to nucleus and back. Frontiers in cell and developmental biology, 10:882037, 2022.

[12] Chung-Liang Ho, Jayme L Martys, Alexei Mikhailov, Gregg G Gundersen, and RK Liem. Novel features of intermediate filament dynamics revealed by green fluorescent protein chimeras. Journal of cell science, 111(13):1767–1778, 1998.

[13] Rudolf E Leube, Marcin Moch, and Reinhard Windoffer. Intracellular motility of intermediate filaments. Cold Spring Harbor perspectives in biology, 9(6):a021980, 2017.

[14] Kyeong Han Yoon, Miri Yoon, Robert D Moir, Satya Khuon, Frederick W Flitney, and Robert D Goldman. Insights into the dynamic properties of keratin intermediate filaments in living epithelial cells. The Journal of cell biology, 153(3):503–516, 2001.

[15] Cécile Leduc and Sandrine Etienne-Manneville. Regulation of microtubule-associated motors drives intermediate filament network polarization. Journal of Cell Biology, 216(6):1689–1703, 2017.

[16] Amélie Robert, Peirun Tian, Stephen A Adam, Mark Kittisopikul, Khuloud Jaqaman, Robert D Goldman, and Vladimir I Gelfand. Kinesin-dependent transport of keratin filaments: a unified mechanism for intermediate filament transport. The FASEB Journal, 33(1):388, 2019.

[17] Gülsen Çolakoğlu and Anthony Brown. Intermediate filaments exchange subunits along their length and elongate by end-to-end annealing. Journal of Cell Biology, 185(5):769–777, 2009.

[18] Lynne Chang and Robert D Goldman. Intermediate filaments mediate cytoskeletal crosstalk. Nature reviews Molecular cell biology, 5(8):601–613, 2004.

[19] Sandrine Etienne-Manneville. Microtubules in cell migration. Annual review of cell and developmental biology, 29(1):471–499, 2013.

[20] Gerhard Wiche. Plectin-mediated intermediate filament functions: why isoforms matter. Cells, 10(8):2154, 2021.

[21] Yaming Jiu, Jaakko Lehtimäki, Sari Tojkander, Fang Cheng, Harri Jäälinoja, Xiaonan Liu, Markku Varjosalo, John E Eriksson, and Pekka Lappalainen. Bidirectional interplay between vimentin intermediate filaments and contractile actin stress fibers. Cell reports, 11(10):1511–1518, 2015.

[22] Emma J van Bodegraven and Sandrine Etienne-Manneville. Intermediate filaments from tissue integrity to single molecule mechanics. Cells, 10(8):1905, 2021.

[23] Caroline Hookway, Liya Ding, Michael W Davidson, Joshua Z Rappoport, Gaudenz Danuser, and Vladimir I Gelfand. Microtubule-dependent transport and dynamics of vimentin intermediate filaments. Molecular biology of the cell, 26(9):1675–1686, 2015.

[24] Chihung H Lin, Enilza M Espreafico, Mark S Mooseker, and Paul Forscher. Myosin drives retrograde f-actin flow in neuronal growth cones. Neuron, 16(4):769–782, 1996.

[25] Selma Osmanagic-Myers, Stefanie Rus, Michael Wolfram, Daniela Brunner, Wolfgang H Goldmann, Navid Bonakdar, Irmgard Fischer, Siegfried Reipert, Aurora Zuzuarregui, Gernot Walko, et al. Plectin reinforces vascular integrity by mediating crosstalk between the vimentin and the actin networks. Journal of cell science, 128(22):4138–4150, 2015.

[26] Florian Huber, Adeline Boire, Magdalena Preciado López, and Gijsje H Koenderink. Cytoskeletal crosstalk: when three different personalities team up. Current opinion in cell biology, 32:39–47, 2015.

[27] Sandra Maday, Alison E Twelvetrees, Armen J Moughamian, and Erika LF Holzbaur. Axonal transport: cargo-specific mechanisms of motility and regulation. Neuron, 84(2):292–309, 2014.

[28] Nobutaka Hirokawa, Shinsuke Niwa, and Yosuke Tanaka. Molecular motors in neurons: transport mechanisms and roles in brain function, development, and disease. Neuron, 68(4):610–638, 2010.

[29] Lukas C Kapitein and Casper C Hoogenraad. Building the neuronal microtubule cytoskeleton. Neuron, 87(3):492–506, 2015.

[30] Nicholas P Boyer, Maite Azcorra, Peter Jung, and Anthony Brown. Imaging and analysis of neurofilament transport in excised mouse tibial nerve. Journal of Visualized Experiments, (162), 2020.

[31] Cynthia L Walker, Atsuko Uchida, Yinyun Li, Niraj Trivedi, J Daniel Fenn, Paula C Monsma, Roxanne C Lariviére, Jean-Pierre Julien, Peter Jung, and

Anthony Brown. Local acceleration of neurofilament transport at nodes of ranvier. Journal of Neuroscience, 39(4):663–677, 2019.

[32] Francis O Schmitt and Betty B Geren. The fibrous structure of the nerve axon in relation to the localization of" neurotubules". The Journal of Experimental Medicine, 91(5):499–504, 1950.

[33] J Daniel Fenn, Christopher M Johnson, Juan Peng, Peter Jung, and Anthony Brown. Kymograph analysis with high temporal resolution reveals new features of neurofilament transport kinetics. Cytoskeleton, 75(1):22–41, 2018.

[34] Yanping Yan and Anthony Brown. Neurofilament polymer transport in axons. Journal of Neuroscience, 25(30):7014–7021, 2005.

[35] Mark M Black, Patricia Keyser, and E Sobel. Interval between the synthesis and assembly of cytoskeletal proteins in cultured neurons. Journal of Neuroscience, 6(4):1004–1012, 1986.

[36] Paul N Hoffman. The synthesis, axonal transport, and phosphorylation of neurofilaments determine axonal caliber in myelinated nerve fibers. The Neuroscientist, 1(2):76–83, 1995.

[37] Paul N Hoffman and Raymond J Lasek. The slow component of axonal transport. identification of major structural polypeptides of the axon and their generality among mammalian neurons. The Journal of cell biology, 66(2):351–366, 1975.

[38] Anthony Brown. Slow axonal transport: stop and go traffic in the axon. Nature Reviews Molecular Cell Biology, 1(2):153–156, 2000.

[39] Subhojit Roy, Bin Zhang, Virginia M-Y Lee, and John Q Trojanowski. Axonal transport defects: a common theme in neurodegenerative diseases. Acta neuropathologica, 109:5–13, 2005.

[40] I Nilsson and CH Berthold. Axon classes and internodal growth in the ventral spinal root l7 of adult and developing cats. Journal of anatomy, 156:71, 1988.

[41] Stephen G Waxman. Determinants of conduction velocity in myelinated nerve fibers. Muscle & Nerve: Official Journal of the American Association of Electrodiagnostic Medicine, 3(2):141–150, 1980.

[42] Joel Eyer and Alan Peterson. Neurofilament-deficient axons and perikaryal aggregates in viable transgenic mice expressing a neurofilament-β-galactosidase fusion protein. Neuron, 12(2):389–405, 1994.

[43] Hélène Jacomy, Qinzang Zhu, Sébastien Couillard-Després, Jean-Martin Beaulieu, and Jean-Pierre Julien. Disruption of type iv intermediate filament network in mice lacking the neurofilament medium and heavy subunits. Journal of neurochemistry, 73(3):972–984, 1999.

[44] Osamu Ohara, Yoshinari Gahara, Toshihiko Miyake, Hiroshi Teraoka, and Tadahisa Kitamura. Neurofilament deficiency in quail caused by nonsense mutation in neurofilament-l gene. The Journal of Cell Biology, 121(2):387–395, 1993.

[45] Takuya Sakaguchi, Manabu Okada, Tadahisa Kitamura, and Kazuo Kawasaki. Reduced diameter and conduction velocity of myelinated fibers in the sciatic nerve of a neurofilament-deficient mutant quail. Neuroscience letters, 153(1):65–68, 1993.

[46] Niraj Trivedi, Peter Jung, and Anthony Brown. Neurofilaments switch between distinct mobile and stationary states during their transport along axons. Journal of Neuroscience, 27(3):507–516, 2007.

[47] J Daniel Fenn, Yinyun Li, Jean-Pierre Julien, Peter Jung, and Anthony Brown.

The mobility of neurofilaments in mature myelinated axons of adult mice. eneuro, 10(3), 2023.

[48] Olaf Wolkenhauer and Mihajlo Mesarović. Feedback dynamics and cell function: why systems biology is called systems biology. Molecular BioSystems, 1(1):14–16, 2005.

[49] Rodolphe Perrot and Joël Eyer. Neuronal intermediate filaments and neurodegenerative disorders. Brain research bulletin, 80(4-5):282–295, 2009.

[50] Stéphanie Millecamps and Jean-Pierre Julien. Axonal transport deficits and neurodegenerative diseases. Nature Reviews Neuroscience, 14(3):161–176, 2013.

[51] Nobutaka Hirokawa. Cross-linker system between neurofilaments, microtubules and membranous organelles in frog axons revealed by the quick-freeze, deep-etching method. The Journal of cell biology, 94(1):129–142, 1982.

[52] Shoichiro Tsukita and Harunori Ishikawa. The cytoskeleton in myelinated axons: serial section study. Biomedical Research, 2(4):424–437, 1981.

[53] Gian Maria Fabrizi, Tiziana Cavallaro, Chiara Angiari, Ilaria Cabrini, Federica Taioli, Giovanni Malerba, Laura Bertolasi, and Nicolo' Rizzuto. Charcot–marie–tooth disease type 2e, a disorder of the cytoskeleton. Brain, 130(2):394–403, 2007.

[54] Alex Mogilner, Roy Wollman, and Wallace F Marshall. Quantitative modeling in cell biology: what is it good for? Developmental cell, 11(3):279–287, 2006.

[55] Adam P Arkin. Synthetic cell biology. Current Opinion in Biotechnology, 12(6):638–644, 2001.

[56] JJ Blum and MC Reed. A model for slow axonal transport and its application to

neurofilamentous neuropathies. Cell motility and the cytoskeleton, 12(1):53–65, 1989.

[57] Anthony Brown, Lei Wang, and Peter Jung. Stochastic simulation of neurofilament transport in axons: the "stop-and-go" hypothesis. Molecular biology of the cell, 16(9):4243–4255, 2005.

[58] JC Dallon, Cécile Leduc, Sandrine Etienne-Manneville, and Stéphanie Portet. Stochastic modeling reveals how motor protein and filament properties affect intermediate filament transport. Journal of theoretical biology, 464:132–148, 2019.

[59] Stéphanie Portet, Cécile Leduc, Sandrine Etienne-Manneville, and John Dallon. Deciphering the transport of elastic filaments by antagonistic motor proteins. Physical Review E, 99(4):042414, 2019.

[60] Chuan Xue, Blerta Shtylla, and Anthony Brown. A stochastic multiscale model that explains the segregation of axonal microtubules and neurofilaments in neurological diseases. PLoS computational biology, 11(8):e1004406, 2015.

[61] JC Dallon, Emily Evans, Christopher P Grant, and Stephanie Portet. Steady state distributions of moving particles in one dimension: with an eye towards axonal transport. Journal of Mathematical Biology, 89(5):56, 2024.

[62] J Daniel Fenn, Christopher M Johnson, Juan Peng, Peter Jung, and Anthony Brown. Kymograph analysis with high temporal resolution reveals new features of neurofilament transport kinetics. Cytoskeleton, 75(1):22–41, 2018.

[63] Aidong Yuan, Mala V Rao, Ralph A Nixon, et al. Neurofilaments and neurofilament proteins in health and disease. Cold Spring Harbor perspectives in biology, 9(4):a018309, 2017.

[64] Aidong Yuan, Takahiro Sasaki, Mala V Rao, Asok Kumar, Vivek Kanumuri, David S Dunlop, Ronald K Liem, and Ralph A Nixon. Neurofilaments form a highly stable stationary cytoskeleton after reaching a critical level in axons. Journal of Neuroscience, 29(36):11316–11329, 2009.

[65] Rob C van Wijk, Elke HJ Krekels, Thomas Hankemeier, Herman P Spaink, and Piet H van der Graaf. Systems pharmacology of hepatic metabolism in zebrafish larvae. Drug Discovery Today: Disease Models, 22:27–34, 2016.

[66] Adrian J Hill, Hiroki Teraoka, Warren Heideman, and Richard E Peterson. Zebrafish as a model vertebrate for investigating chemical toxicity. Toxicological sciences, 86(1):6–19, 2005.

[67] Wassim M Haddad and VijaySekhar Chellaboina. Nonlinear dynamical systems and control: a Lyapunov-based approach. Princeton university press, 2008.

[68] H. K. Khalil. Nonlinear system, 3rd ed. Prentice Hall, New Jersey, 2002.

[69] Robert M May. Will a large complex system be stable? Nature, 238(5364):413–414, 1972.

[70] Morris W Hirsch, Robert L Devaney, and Stephen Smale. Differential equations, dynamical systems, and linear algebra, volume 60. Academic press, 1974.

[71] Leah Edelstein-Keshet. Mathematical models in biology. SIAM, 2005.

[72] Michael G Neubert and Hal Caswell. Alternatives to resilience for measuring the responses of ecological systems to perturbations. Ecology, 78(3):653–665, 1997.

[73] Sergey S Demidov. The study of partial differential equations of the first order in the 18th and 19th centuries. Archive for History of Exact Sciences, 26(4):325–350, 1982.

[74] Ramadan Abdelaziz. Introducing global optimization vs. local optimization in water resource management. 2025.

[75] Eligius MT Hendrix, G Boglárka, et al. Introduction to nonlinear and global optimization, volume 37. Springer, 2010.

[76] Leo Liberti. Introduction to global optimization. Ecole Polytechnique, 1:1–43, 2008.

[77] Goldberg D. E. Genetic algorithms in search, optimization, and machine learning. Reading: Addison-Wesley., 1989.

[78] Melanie Mitchell. An Introduction to Genetic Algorithms. MIT Press, Cambridge, MA, 1996.

[79] Tom V Mathew. Genetic algorithm. Report submitted at IIT Bombay, 53, 2012.

[80] Lingaraj Haldurai, T Madhubala, and R Rajalakshmi. A study on genetic algorithm and its applications. Int. J. Comput. Sci. Eng, 4(10):139–143, 2016.

[81] Bibek Rawat, Dipesh Duwal, Sagar Phuyal, and Aparana Pant. A comparative review between various selection techniques in genetic algorithm for finding optimal solutions. Int. J. Comput. Sci. Eng., 10(10):15–22, 2022.

[82] Luca Scrucca. Ga: A package for genetic algorithms in r. Journal of Statistical Software, 53:1–37, 2013.

[83] Jennifer Lippincott-Schwartz, Nihal Altan-Bonnet, and George H Patterson. Photobleaching and photoactivation: following protein dynamics in living cells. Nature Biotechnology, 20:87–90, 2002.

[84] PAUL N Hoffman, RAYMOND J Lasek, JOHN W Griffin, and DL Price. Slowing of the axonal transport of neurofilament proteins during development. Journal of Neuroscience, 3(8):1694–1700, 1983.

[85] Gheorghe Craciun, Anthony Brown, and Avner Friedman. A dynamical system model of neurofilament transport in axons. Journal of Theoretical Biology, 237(3):316–322, 2005.

[86] Lei Wang, Chung-liang Ho, Dongming Sun, Ronald KH Liem, and Anthony Brown. Rapid movement of axonal neurofilaments interrupted by prolonged pauses. Nature cell biology, 2(3):137–141, 2000.

[87] Atsuko Uchida and Anthony Brown. Arrival, reversal, and departure of neurofilaments at the tips of growing axons. Molecular biology of the cell, 15(9):4215–4225, 2004.

[88] Lei Wang and Anthony Brown. Rapid intermittent movement of axonal neurofilaments observed by fluorescence photobleaching. Molecular biology of the cell, 12(10):3257–3267, 2001.

[89] Robert Piessens, Elise de Doncker-Kapenga, Christoph W Überhuber, and David K Kahaner. Quadpack: a subroutine package for automatic integration, volume 1. Springer Science & Business Media, 2012.

[90] Nael H Alami, Peter Jung, and Anthony Brown. Myosin va increases the efficiency of neurofilament transport by decreasing the duration of long-term pauses. Journal of Neuroscience, 29(20):6625–6634, 2009.

[91] SL Pimm and JH Lawton. Number of trophic levels in ecological communities. Nature, 268(5618):329–331, 1977.

[92] TUFAIL Malik, PAUL Salceanu, ANUJ Mubayi, ABDESSAMAD Tridane, and MUDASSAR Imran. West nile dynamics: virus transmission between domestic

and wild bird populations through vectors. Can. Appl. Math. Quart, 20(4):535–556, 2012.

[93] Anuj Mubayi, Priscilla Greenwood, Xiaohong Wang, Carlos Castillo-Chávez, Dennis M Gorman, Paul Gruenewald, and Robert F Saltz. Types of drinkers and drinking settings: an application of a mathematical model. Addiction, 106(4):749–758, 2011.

[94] Jon C Helton. Uncertainty and sensitivity analysis techniques for use in performance assessment for radioactive waste disposal. Reliability Engineering & System Safety, 42(2-3):327–367, 1993.

[95] Andrea Saltelli, Karen Chan, and E Marian Scott. Sensitivity analysis: Gauging the worth of scientific models. John Wiley & Sons, 2000.

[96] Salaheldin Omer and Hermane Mambili-Mamboundou. Analysis of a combination of cancer treatments in efforts to overcome drug resistance. Computers in Biology and Medicine, 192:110278, 2025.